

Seeing Through the Fog:
Using Scattered Light to Peer Deeper into Biological
Tissue

Thesis by
Joshua Harris Brake

In Partial Fulfillment of the Requirements for the
Degree of
Doctor of Philosophy

The logo for the California Institute of Technology (Caltech), featuring the word "Caltech" in a bold, orange, sans-serif font.

CALIFORNIA INSTITUTE OF TECHNOLOGY
Pasadena, California

2019
Defended May 17th, 2019

© 2019

Joshua Harris Brake
ORCID: 0000-0002-5113-6886

All rights reserved except where otherwise noted

ACKNOWLEDGEMENTS

"If I have seen further it is by standing on the shoulders of giants." - Isaac Newton

During the course of my PhD studies at Caltech there are numerous people who have made a significant impact not only on my development as an engineer and scientist, but also as a person. I am very thankful for all those who have poured into me, and hope that I can model the lessons they have taught me as I seek to mentor and guide the next generation of budding scientists and engineers.

First of all, I am grateful to my advisor Prof. Changhuei Yang for seeing something in me when I applied, and mentoring me over the past five years. He is an encouraging and honest advisor who has been a constant support during my PhD journey. I am thankful for his critiques and suggestions about my research ideas and his financial support for my studies, research supplies, and conference travel. I continue to appreciate the way he tailors his guidance to the individual needs of the members in the group and the energy he brings to the field of biophotonics.

Research is never done in a vacuum, and the members of one's research group are crucial to both a productive and happy PhD experience. I am fortunate to have been surrounded by a series of great postdocs and fellow PhD students who have poured into me during my 5 years in the lab. There are several people who deserve particular mention. Haowen Ruan for teaching me the ropes of combining ultrasound and light for wavefront shaping and providing many examples of how to draw beautiful and clear figures for research papers and presentations. Mooseok Jang for helping teach me about the physics of decorrelation and wavefront shaping. Edward Zhou for showing me many tips and tricks about how to precisely align optical systems. Albert Chung for giving me my initial tour of Caltech when I visited and for his many insights on all things computational imaging over the years. Roarke Horstmeyer for explaining the essence of optical systems using simple mathematical concepts. Elliott Robinson for teaching me about neuroscience, showing me how to patch clamp, helping me with various experiments over the years, and for being around to chat about football and baseball. Jian Xu and Ali Kazemi Jahromi for working alongside me on the interferometric speckle visibility project. Yan Liu for discussions about wavefront shaping. In addition, I am thankful for the other members in the group who have been fun to hang out with and have asked helpful questions and given good critiques over the years: Atsushi Shibukawa, Jinho Kim,

Xiaoze Ou, Daifa Wang, Donghun Ryu, Liheng Bian, Yidong Tan, Helen Lu, Daniel Martin, Yujia Huang, Michelle Cua, Cheng Shen, Changsoon Choi, Ruizhi Cao, and Antony Chan. Finally, a big thanks to Anne Sullivan for all her help over the years with ordering and helping keep the group operations running smoothly.

I would also like to thank my committee members Prof. Lihong Wang, Prof. Viviana Gradinaru, Prof. Azita Emami, and Prof. Euiheon Chung. It is a privilege to have the opportunity to work with such world-class scientists and engineers and to learn from their critiques and suggestions.

My life outside the lab in Pasadena over the past five years has also been a rich one and has helped me to bring a fresh and resilient attitude to the lab. In particular I am thankful for the great church home Abbey and I found at Grace Pasadena. The entire church staff made us feel welcome from our first week visiting and has helped both Abbey and I feel at home in Pasadena. For that I am thankful; especially to Brannin and Tanya Pitre, Marc Choi, and Jen Argue. I am also especially thankful for my friend Ben Ewen who has been an encouragement to me throughout my studies (and for his contributions to my coffee hobby!). Our city group has been a source of encouragement each week, and I have been enriched by the fellowship each Friday morning with the Grace men's group (Ben Ewen, Dave McFadzean, Justin Su, Eric Branscum, Mark Pickett, Zach Lee, and Gene Fahnestock). I have also been blessed to work alongside Len Tang and Jeff Still to launch the Science and Faith Examined project on the Caltech campus and have been blown away by how God has used it to spark conversations, develop relationships, and open doors for the Gospel on campus.

Another significant activity outside the lab during my time at Caltech has been my involvement with the Caltech-Occidental Wind Orchestra (formerly known as the Caltech-Occidental Concert Band). I missed playing trumpet during my undergrad years, so it was great to be able to resume playing with such an excellent group. In particular, I am thankful for Bill Bing and his leadership of the group for many years preceding my time and also for Glenn Price and the work he has done to carry on Bill's legacy and push us to ever higher levels of musicality. Of course, it goes without saying that the best part of the band has been playing next to several fellow partners-in-crime in the trumpet section; in particular, John Brugman (whose beautiful tone and musical playing continues to inspire my own playing), Les Deutsch, and Wil Rose who make Thursday nights both musically rewarding and fun.

There are many past teachers from my undergrad years at LeTourneau University that were integral in getting me to where I am today. I will always be thankful for Bill Graff and the many lessons I learned both as his student and from my experience getting to teach alongside him. My pedagogical approach has been shaped by the concepts I saw him use like frequent low-stakes testing and hands-on active learning with lab exercises. I am also thankful for others at LeTourneau like Paul Leiffer and Joonwan Kim and the lessons they taught me about how to live as a faithful Christian engineer. Others who had an impact during my student years include my research advisor Seung Kim and thesis advisor Steve Ball.

I also owe thanks to several instrumental high-school teachers: Dan Vinton for teaching me to love math early on, and Jim Bair for helping me hone my writing and always ask "so what?"

Throughout my life, I am particularly thankful for the support, encouragement, example, and love of my family. My grandparents Roger and Eleanor Brake and Gordon and Bernina Danielson always supported and encouraged me. My grandfather Roger Brake, in particular, taught me the value of not only working hard, but working smart.

I am also deeply indebted to my parents Jim and Marjie Brake. Mom, I'll always remember the homeschool days, and all the hours you spent teaching Nate and me and helping with a variety of school-related activities throughout elementary and high school. Dad, for your example of working hard, managing what the Lord has given you well, and faithfully providing for your wife and kids. I'm also thankful for my brother Nate and sister Rachel and their encouragement and support over the years.

Abbey, I am so grateful to have had you at my side for these past 5 years as my wife (not to mention the many years prior as my best friend) and to be experiencing life together with you day by day. I cannot wait to see what the Lord has for us and our family in this next stage at Harvey Mudd. I love you.

Finally, I am thankful to my Lord and Savior Jesus Christ and for his life, death, and resurrection.

Soli deo gloria.

ABSTRACT

Optical scattering is a fundamental problem in biomedical optics and limits most optical techniques to shallow operating depths less than 1 mm. However, although the scattering behavior of tissue scrambles the information it contains, it does not destroy it. Therefore, if you can unscramble the scattered light, it increases the accessible imaging depths up to the absorption limit of light (several centimeters deep).

One such way to beat optical scattering is using wavefront shaping. Borrowing ideas from adaptive optics in astronomy and phased arrays in radar and ultrasonic imaging, the basic concept of wavefront shaping is to control the phase and amplitude of the light field in order to harness scattered light. Using wavefront shaping techniques, scattered light can be used to form focal spots or transmit information through or inside optically scattering media. Furthermore, even without correcting for scattering directly by shaping the input light field, the properties of the scattered light can be analyzed to recover information about the structure and dynamic properties of a sample using methods from diffuse optics.

The main contributions of this thesis are along these two lines of research: moving wavefront shaping toward more practical applications and developing new techniques to recover useful physiological information from scattered light. This is developed through three main projects:

1. An investigation of how dynamic samples impact the scattering process and the practical implications of these dynamics on wavefront shaping systems.
2. The development of a wavefront shaping system combining light and ultrasound to focus light inside acute brain slices to improve light delivery for optogenetics.
3. A novel method to sensitively detect the dynamics of scattered light and use it to tease out information about the flow of blood within the tissue sample of interest.

PUBLISHED CONTENT AND CONTRIBUTIONS

- D. Wang[†], E. H. Zhou[†], **J. Brake**, H. Ruan, M. Jang, and C. Yang, “Focusing through dynamic tissue with millisecond digital optical phase conjugation,” *Optica*, 2(8), pp. 728–735, 2015. DOI: 10.1364/OPTICA.2.000728
J. B. helped prepare the some of the figures and develop the flow and presentation of the results in the manuscript.
- **J. Brake**[†], M. Jang[†], and C. Yang, “Analyzing the relationship between decorrelation time and tissue thickness in acute rat brain slices using multispeckle diffusing wave spectroscopy,” *JOSA A*, 33(2), pp. 270–275, 2016. DOI: 10.1364/JOSAA.33.000270
J. B. developed the experimental setup with help from M. J., drew the figures, and wrote and edited the manuscript with help from M. J. and C. Y.
- E. H. Zhou, A. Shibukawa, **J. Brake**, H. Ruan, and C. Yang, “Glare suppression by coherence gated negation,” *Optica*, 3(10), pp. 1107–1113, 2016. DOI: 10.1364/OPTICA.3.001107
J. B. helped design the figures, develop the data visualization, and write the manuscript.
- M. M. Qureshi[†], **J. Brake**[†], H.-J. Jeon, H. Ruan, Y. Liu, A. M. Safi, T. J. Eom, C. Yang, and E. Chung, “In vivo study of optical speckle decorrelation time across depths in the mouse brain,” *Biomedical Optics Express*, 8(11), pp. 4855–4864, 2017. DOI: 10.1364/BOE.8.004855
J. B. helped to design the experiment with M. M. Q., analyzed the data, drew the figures, and helped write the manuscript.
- H. Ruan[†], **J. Brake**[†], J. E. Robinson, Y. Liu, M. Jang, C. Xiao, C. Zhou, V. Gradinaru, and C. Yang, “Deep tissue optical focusing and optogenetic modulation with time-reversed ultrasonically encoded light,” *Science Advances*, 3(12), eaao5520, 2017. DOI: 10.1126/sciadv.aao5520
J. B. ran the experiments along with H. R. and J. E. R., did the majority of the data processing, helped design the figures along with H. R., and took the lead on the manuscript writing.

- H. Ruan, T. Haber, Y. Liu, **J. Brake**, J. Kim, J. M. Berlin, and C. Yang, “Focusing light inside scattering media with magnetic-particle-guided wavefront shaping,” *Optica*, 4(11), pp. 1337–1343, 2017. DOI: 10.1364/OP-TICA.4.001337

J. B. helped to develop the experimental procedure and to prepare and edit the manuscript.

- M. Jang[†], Y. Horie[†], A. Shibukawa[†], **J. Brake**, Y. Liu, S. M. Kamali, A. Arbabi, H. Ruan, A. Faraon, and C. Yang, “Wavefront shaping with disorder-engineered metasurfaces,” *Nature Photonics*, 12(2), p. 84, 2018. DOI: 10.1038/s41566-017-0078-z

J.B. helped develop the idea, draw the figures, and write and edit the manuscript.

Note: † indicates co-first authorship

TABLE OF CONTENTS

Acknowledgements	iii
Abstract	vii
Published Content and Contributions	viii
Table of Contents	x
List of Illustrations	xii
Chapter I: Introduction	1
1.1 Light-Matter Interactions	2
1.2 Relevant Properties of Light	10
1.3 Interferometry	15
1.4 Light propagation through disordered media	22
1.5 Wavefront shaping	27
1.6 Decorrelation	32
1.7 Outline of this thesis	32
Chapter II: The relationship between decorrelation and tissue thickness in acute rat brain tissue slices	35
2.1 Abstract	35
2.2 Wavefront shaping and decorrelation time	35
2.3 Multispeckle diffusing wave spectroscopy	36
2.4 Experimental setup for measuring decorrelation in acute brain slices	39
2.5 Multispeckle decorrelation analysis procedure	40
2.6 Multispeckle decorrelation time results	41
2.7 Decorrelation time and the influence of absorption: Monte Carlo simulation results	44
2.8 Conclusion	46
Chapter III: Decorrelation in the <i>in vivo</i> mouse brain due to blood flow	50
3.1 Abstract	50
3.2 Wavefront shaping and decorrelation in living tissue	50
3.3 Multispeckle decorrelation theory and analysis in living tissue	52
3.4 Experimental setup for <i>in-vivo</i> multispeckle decorrelation measurements of the rat brain	54
3.5 <i>In-vivo</i> decorrelation measurement results	57
3.6 Discussion and Conclusion	60
Chapter IV: Improved light delivery for optogenetics using digital time-reversed ultrasonically-encoded (TRUE) light focusing	66
4.1 Abstract	66
4.2 Introduction	66
4.3 Results	72
4.4 Discussion	82
Chapter V: Interferometric speckle visibility spectroscopy	92

5.1 Abstract	92
5.2 Introduction	92
5.3 Theory	95
5.4 iSVS and SVS Data Processing Procedure	97
5.5 Experimental Results	99
5.6 Discussion and Future Work	106
Chapter VI: Conclusion	108

LIST OF ILLUSTRATIONS

<i>Number</i>	<i>Page</i>
1.1 Jablonski diagram	3
1.2 Scattering on a foggy morning in Pasadena, CA	4
1.3 Scattering through thick slab of scattering material	6
1.4 Cartoon describing how the directionality of scattered light is quantified.	7
1.5 A cartoon describing the principle of temporal coherence.	12
1.6 A cartoon describing the principle of spatial coherence	14
1.7 Simple holography schemes.	16
1.8 Shot noise explanation with a raincloud and showerhead	20
1.9 Scattering regimes	23
1.10 Transmission matrix diagram	25
1.11 Phasor diagram illustrating the interference of different modes in a speckle pattern.	28
1.12 Feedback-based wavefront shaping	30
1.13 Time-reversal-based wavefront shaping	31
2.1 Experimental setup used to capture the speckle patterns.	40
2.2 $g_2(\tau)$ decorrelation time calculation	41
2.3 Decorrelation curves for 1.0, 1.5, 2.0, and 3.0 mm thick brain slices. .	42
2.4 Decorrelation times of the individual trials plotted with respect to tissue thickness.	43
2.5 Results of the Monte Carlo simulation of 1×10^6 photons with tissue properties $\mu_s = 5/\text{mm}$, $\mu_a = 0.2/\text{mm}$, and $g = 0.9$	45
2.6 Inverse mean path length $\langle P(s) \rangle$ vs sample thickness from 1-3 mm. .	46
3.1 Diagram of the experimental setup	55
3.2 Characterization of diffusing fiber tip light distribution	56
3.3 Decorrelation curves for different fiber tip depths	58
3.4 Decorrelation time as a function of fiber tip penetration depth	59
4.1 Custom TRUE focusing and electrophysiological recording system . .	69
4.2 Schematic of the TRUE focusing system	70
4.3 TRUE Focusing system electrical signal flow diagram	71
4.4 A comparison of TRUE focusing and conventional focusing	74

4.5	Experiment design, opsin characterization, and demonstration of photocurrent and firing modulation via TRUE focusing	76
4.6	Ultrasound pulse-echo image of the tip of the glass pipette electrode	78
4.7	Electrophysiological photocurrent traces from neurons in 500 μm and 300 μm thick acute brain slices	79
4.8	Electrophysiological photocurrent and membrane voltage traces comparing ultrasound on and off conditions	80
4.9	Spatial resolution of optogenetic stimulation achieved by conventional versus TRUE focusing	81
5.1	iSVS decorrelation explanation	96
5.2	iSVS data processing procedure	98
5.3	iSVS Experimental Setup	100
5.4	Advantage of vertical slit in the Fourier domain for optimal spatial frequency bandwidth usage	101
5.5	Rotating diffuser calibration setup	102
5.6	iSVS and SVS results vs. decorrelation time with rotating diffuser	102
5.7	iSVS and SVS results in the dorsal skin flap: transmission	104
5.8	iSVS and SVS results in the dorsal skin flap: reflection	105

Chapter 1

INTRODUCTION

“If you see through everything, then everything is transparent. But a wholly transparent world is an invisible world. To ‘see through’ all things is the same as not to see.” - C.S. Lewis

Focusing light into biological tissue is a critical capability in medicine, for a variety of diagnostic and research purposes. Medical imaging technologies using magnetic resonance, ultrasound, X-ray, or positron emission can penetrate deeply through tissue and thus enable entire organisms or parts of organisms to be imaged. However, each of these imaging technologies suffers from drawbacks, which prevent them from being maximally useful for biological diagnostic imaging or sensing. For example, the large magnetic fields necessary for magnetic resonance imaging (MRI) make it challenging to design affordable and compact systems. Furthermore, the resolution of MRI typically cannot extend beyond a cubic millimeter, which limits the ability to examine the fine structural or functional signals that are of interest in the brain as measured in functional MRI. Ultrasound, while noninvasive and safe even for the most delicate of tasks such as imaging babies in the womb, has limited spatial resolution due to the size of the acoustic wavelengths used and often needs additional contrast mechanisms to enable high enough signal-to-noise ratio (SNR) to image the structures of interest. Finally, X-ray and positron emission tomography use ionizing radiation, which can damage the sample under examination and are also limited in terms of the types of contrast they can image.

An ideal imaging technology would be able to image high spatial resolutions to capture the minute details of the structures of interest, high temporal resolutions to resolve the dynamics present in the sample, and employ many different contrast mechanisms to visualize structure and function with high selectivity and SNR. Additional valuable properties would include the ability to be able to safely image without concerns about toxicity or damage to the sample and the ability to image deeply and noninvasively. Light checks most of these boxes, but unfortunately struggles to image deeply inside tissue since tissue is strongly scattering to optical wavelengths (400-1000 nm). In the next few sections, we will discuss some of many fundamental properties of light that are useful for biological imaging, and also show

the physical and mathematical origins of optical imaging and strategies to address this scattering.

1.1 Light-Matter Interactions

The many types of interaction between light and matter provide a wide range of different contrast mechanisms that can be used to interrogate samples of interest. In optics, these contrast mechanisms can be exploited in order to provide information about the structure and function of different materials inside the medium. The foundation for light-matter interaction is based on the electronic structure of the atoms and molecules making up the matter. Molecular and atomic energy levels exist and are quantized, and the distribution and spacing between these levels specify their electronic behavior. The Jablonski diagram is a visual representation of this electronic structure and is helpful for discussing light-matter interactions. An example of a Jablonski diagram is shown in Figure 1.1. The thick solid lines indicate the electronic states, and the thinner lines indicate different vibrational states within the given electronic states. Nonradiative transitions are indicated by straight arrows, while radiative transitions are indicated by squiggly lines. These different types of transitions will be described subsequently.

In general, there are two main classes of light-matter interaction, resonant and non-resonant. These classes provide the physical basis for contrast mechanisms such as absorption, fluorescence, phosphorescence, and scattering.

Resonant interactions refer to those where the energy of the incoming photon matches one of the internal energy levels present within the atomic structure of the material. When this matching occurs, the molecule can absorb the energy from the incoming photon and cause an electron to jump to an excited state. When the molecule is in the excited state, it will naturally relax to a lower energy state. This decay can happen through two main pathways: nonradiative and radiative relaxation.

Nonradiative processes include vibrational relaxation, internal conversion, and intersystem crossings. Vibrational relaxations are the process through which the excited electron drops to a different vibrational energy level and dissipates the energy into its surroundings. Internal conversion describes the process by which an electron drops to a lower electronic energy state without emitting a photon while maintaining its spin state. These processes occur very quickly, on the time scale of 10^{-14} to 10^{-11} seconds. Intersystem crossings describe the process by which excited electrons change energy levels and also change their spin state. Intersystem crossings occur

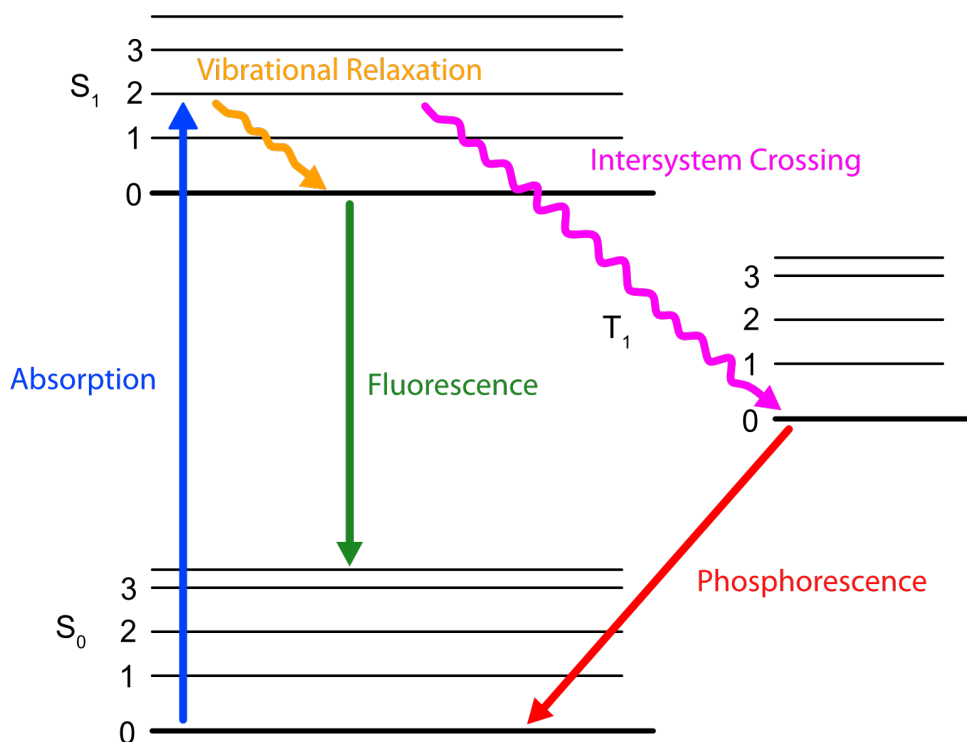


Figure 1.1: An example of a Jablonski diagram.

on a much slower time scale, from 10^{-8} to 10^{-3} seconds.

Radiative processes are those in which a photon is reemitted as the excited electron decays to a lower energy state. Fluorescence is the process by which electrons relax from an excited electronic state to a lower electronic energy level and emit a photon. The electron maintains its spin state, and so this is a relatively fast process, typically ranging from one to one hundred nanoseconds. In contrast, phosphorescence occurs when the excited electron relaxes but changes its spin state. Since this process requires an intersystem crossing, it has a much slower time scale than fluorescence, typically ranging from the millisecond range to several seconds.

In addition to these resonant mechanisms, there are also nonresonant interactions which occur when the energy of the incoming photon do not match any of the atomic or molecular energy level spacings. These types of interaction include elastic scattering processes such as Rayleigh or Mie scattering. In elastic scattering, the molecules act as simple dipoles and re-emit light at the same energy as the



Figure 1.2: **Scattering on a foggy morning in Pasadena, CA.**

incoming photons. Nonresonant interactions also include scattering phenomena such as Raman scattering. While this is an inelastic scattering mechanism since the energy of the emitted light differs from that of the incident light, it is distinct from the resonant interactions since the energy states of interest are virtual states, not actual energy levels that exist within the electronic structure of the molecules.

These light-matter interactions are what enable imaging systems, whether cameras or the human eye, to form images of the world around us. Light as it illuminates an object encounters the boundary of the object which causes it to be absorbed, reflect, or refract based on the optical properties of the interface (e.g., the absorptivity or the change in refractive index). Scattering from differences in refractive index is fundamental to imaging since it causes the light to be redirected, enabling it to be captured by an imaging system. However, while the scattering of light is an important form of optical contrast, enabling us to be able to see anything at all, unwanted scattering (or more precisely uncontrolled scattering as we will see later in thesis) is detrimental in an optical system.

Unfortunately, unwanted scattering is quite prevalent in many types of optical imaging. In atmospheric imaging or astronomy, particles in the atmosphere such as clouds or dust scatter light and hamper the formation of clear, high-quality images. In everyday life, we have likely all driven through a fog (see Figure 1.2) or noticed

the optical opacity of clouds as the sun tries to pierce through them on an overcast day. From the perspective of microscopy, the unwanted scattering of rough tissue interfaces or out-of-focus layers within a biological tissue sample scatter light and prevent clear imaging of the deeper layers below. For this reason, most biological tissue samples used in microscopy are cut in thin slices to limit the degree of unwanted scattering. Unfortunately, cutting the samples into thin slices creates additional levels of complexity and has undesirable side effects such as physically damaging the sample and making three-dimensional registration of the components within the tissue difficult.

In the next sections, we will look in more detail about how we can mathematically describe the physical phenomena of light scattering and absorption and build models to inform the development of optical tools for biomedicine.

Light Scattering Modeling

Scattering Coefficient Derivation

To get a better understanding of elastic scattering, it is helpful to spend a few paragraphs to develop a simple mathematical model to describe the scattering process. This model will allow us to build up from first principles an intuitive mathematical understanding of how we can visualize scattering and provide us with several quantitative measures of optical scattering (such as the strength of scattering, directionality of scattering, and the delineation different scattering regimes).

In this section, quantities will be given names with their dimensions in square brackets (e.g., a distance x has a dimension of length denoted by $[l]$). To start, we will consider the transmission of light through a sample of thickness L $[l]$ with a number volumetric concentration n $[\# \cdot l^{-3}]$ of scatters with scattering cross-section σ_s $[l^2]$. Now, using a typical trick in calculus, we will slice our thick scattering medium of thickness L into an arbitrarily small thickness δx $[l]$. The number of scatterers in this slab is $nA\delta x$ $[\#]$.

Now for this slab, what is the probability that a photon will pass through the slab unscattered? First, we can derive probability that a photon is scattered which is simply given by

$$P(\text{scattered}_{\delta x}) = \frac{\text{Ratio of scattering area}}{\text{Total area of slab}} = \frac{(nA\delta x)\sigma_s}{A} = n\delta x\sigma_s. \quad (1.1)$$

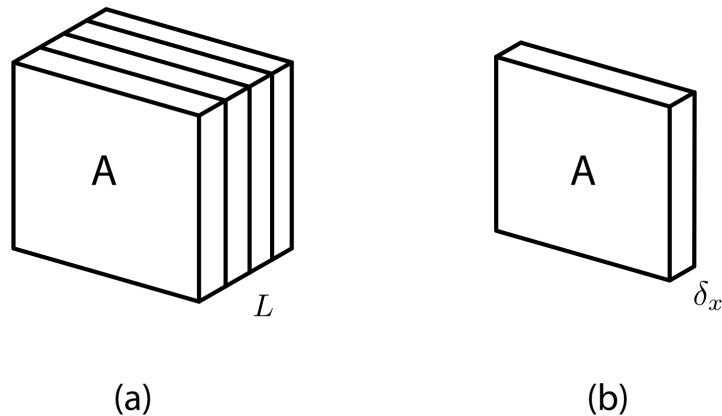


Figure 1.3: **Scattering through thick slab of scattering material.** (a) A scattering medium of cross-sectional area A and thickness L . (b) A slice of the scattering medium of thickness δx .

From this, we can calculate the probability that a photon is unscattered as

$$P(\text{unscattered}_{\delta x}) = 1 - P(\text{scattered}_{\delta x}) = 1 - n\delta x\sigma_s = \exp(-n\delta x\sigma_s) \quad (1.2)$$

where the last step uses the fact that δx can be made arbitrarily small to use the Taylor series expansion to represent the probability as an exponential.

This allows us to calculate the probability of a photon passing through the whole slab unscattered as the probability that it passes through a succession of individual thin slabs with the probabilities of being unscattered as given in Eq. 1.2. By definition, the number of slabs that makes up our whole scattering sample is given by $\frac{L}{\delta x}$ [#]. So, the probability of a photon passing unscattered through the entire slab is given by

$$P(\text{unscattered}_L) = \exp(-n\delta x\sigma_s)^{\frac{L}{\delta x}} = \exp(-n\sigma_s L). \quad (1.3)$$

This leads to the definition of a dimension of interest for scattering, the scattering mean free path l_s [l] or its inverse, the scattering coefficient $\mu_s = n\sigma_s$ [l^{-1}]. Formally defined, this is the thickness at which the fraction of unscattered light is given by $\frac{1}{e}$.

Scattering Anisotropy

Another quantity of interest is the directionality of the scattered light. When light interacts with a scattering sample, the light is redirected in many directions. How-

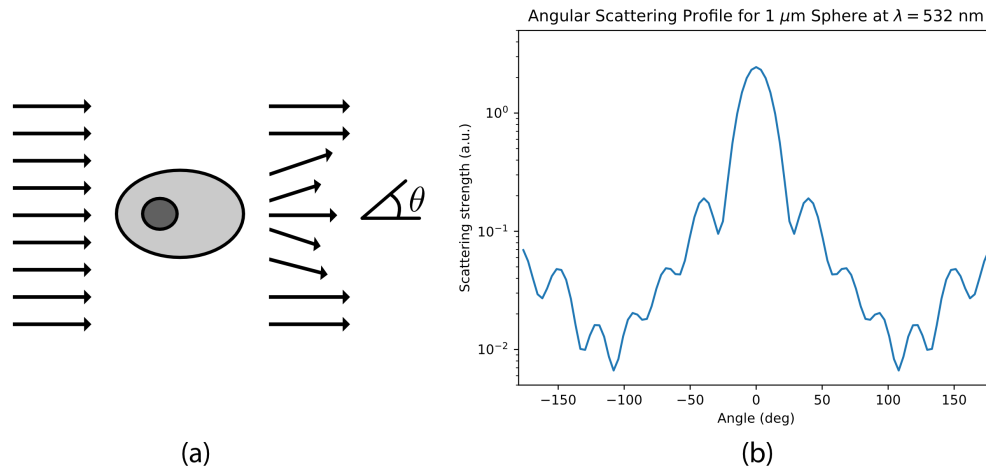


Figure 1.4: **Cartoon describing how the directionality of scattered light is quantified.** (a) An incident collimated beam is incident on a scattering medium such as a cell or piece of tissue. After interacting with the cell, the exiting light is scattered into different directions and can be quantified by measuring the intensity of light directed into a given angle. (b) A plot of scattered light intensity vs. angle for a solution of $1\ \mu\text{m}$ spheres with refractive index of $n = 1.5$ suspended in water (refractive index $n = 1$) illuminated with $532\ \text{nm}$ light at a concentration of 0.1 spheres per cubic micron. Plots calculated using the Mie scattering calculator from the Oregon Medical Laser Center (OMLC) Mie Calculator.

ever, the degree to which light is redirected from the original propagation direction into another direction differs based on the physical parameters of the sample. We can quantify this directionality by measuring the intensity of the scattered light as a function of angular deviation from the original propagation direction as shown in Figure 1.4.

While a plot of the scattered light intensity vs. scattering angle θ gives a good sense of the exact distribution of scattered light, it is also helpful to have a single metric which describes the scattering directionality. When light is scattered into a new direction, there is a component of the scattered light direction that is aligned with direction of the original unscattered light. To help describe the directionality, we can measure the average value of the forward directed light that is retained after the scattering event using the anisotropy factor, g , which is defined as the average of the cosine of the scattering angle.

$$g = \int_0^\pi p(\theta) \cos(\theta) 2\pi \sin(\theta) d\theta = \langle \cos(\theta) \rangle \quad (1.4)$$

The anisotropy factor g gives a quick sense of the scattering behavior and describes how forward scattering a material is. When the scattering is in the forward direction, then $g \in (0, 1]$ with $g \approx 1$ representing strong forward-directed scattering, when it is isotropic then $g = 0$, and when the scattering is backward directed then $g \in (0, -1]$. In biological tissue, which is in general very forward scattering, a typical value of g is ~ 0.9 .

The most important parameter governing the directionality of the scattered light is the size of particle compared to the wavelength of light. We can separate it into three general cases. When the particle is much smaller than the wavelength of light ($d \ll \lambda/10$), the scattering is nearly isotropic and $g \approx 0$. This regime is called Rayleigh scattering. In this regime, the intensity of the scattered light scales according to inverse of the wavelength to the fourth power ($I_{\text{scattered}} = \lambda^{-4}$). Thus, in the Rayleigh regime, shorter wavelengths scatter much more strongly than longer ones. The most common everyday manifestation of Rayleigh scattering is the blue color of the sky.

When the size of the particle is on the same order as the wavelength, the anisotropy can vary quite drastically based on the size of the particle and the difference between its refractive index and that of the background media. This regime can be described and analyzed using Mie theory and the Van de Hulst method. Finally, when the particle is much larger than the wavelength ($d > 10\lambda$), geometric optics can accurately describe the scattering phenomena. However, most of the interesting scattering in biomedicine is caused by particles on the order or smaller than the optical wavelength such as organelles and cell membranes.

Transport mean free path

While the directionality of the scattering is a useful criterion when discussing a single scattering event, once a photon has encountered a series of scattering events, the direction of the photon propagation becomes randomized. At this point, the direction the photon is propagating has no correlation with the direction at which it entered the scattering medium, and the light propagation can be modeled as a diffusion process.

A helpful rule of thumb for the length scale at which this diffusion process takes over is called the transport mean free path (l^*) and is defined as

$$l^* = \frac{l}{(1 - g)}. \quad (1.5)$$

The transport mean free path represents the distance where effectively no ballistic photons remain and is the point at which conventional optical microscopy techniques that rely on ballistic light begin to fail. The typical transport mean free path in biological tissue is $l^* \approx 1$ mm.

Mie Theory and the Rayleigh-Gans-Debye Approximation

In a scattering medium like biological tissue, there are many scattering events and it is hard to usefully characterize the scattering behavior with anything but the parameters we have already discussed like mean free path, transport mean free path, anisotropy, etc. However, to get a better sense of how scattering happens, we can simplify the problem and look at the scattering due to a single spherical particle. Mie theory, developed by Gustav Mie, is an exact solution to Maxwell's equations for the scattering behavior of a spherical particle under illumination by a electromagnetic plane wave. From Mie theory, we can better understand the specific behavior of scattering and then abstract this knowledge to more complicated cases.

In the case where the refractive index contrast of the sphere (i.e., the relative refractive index of the sphere n_s compared to the background medium n_b is nearly 1, $\left| \frac{n_s}{n_b} - 1 \right| \ll 1$) and the phase shift of the light passing through the sphere is small $2ka \left| \frac{n_s}{n_b} - 1 \right| \ll 1$, an approximation known as the Rayleigh-Gans-Debye approximation can be applied to simplify the Mie theory. Interested readers are suggested to consult reference [1] for more details.

Light Absorption

Light absorption occurs when the energy of a photon is transferred to an electron within a material, causing the electron to rise to a higher energy level. This absorption process occurs when the incoming photon is matched in energy to the vibrational frequency of the electron. Therefore, the energy (and correspondingly the frequency or wavelength) of the light must be matched to the vibrational frequency of the electron for this absorption process to occur, leading to wavelength dependent absorption spectra. Once the energy is transferred to the absorption molecule,

the energy that is now contained in the excited electron vibrations can either be transferred to another molecule, re-emitted as light at a lower energy, or emitted as heat.

Following a similar derivation as used above for scattering, we can also develop a metric to quantitatively describe the amount of absorption in a given medium. To start, we will again imagine a thick slab of material with a number concentration of absorbers given by n [$\# \cdot l^{-3}$] and an absorption cross section given by σ_a [l^2]. Again, dividing up the medium into thin slices of thickness δx [l] we can calculate the probability of a photon not being absorbed as

$$P(\text{unabsorbed}_{\delta x}) = 1 - P(\text{absorbed}_{\delta x}) = 1 - n\delta x\sigma_a = \exp(-n\delta x\sigma_a). \quad (1.6)$$

Again, expanding this to the entire thickness L of the absorbing medium, we can find that the probability of a photon being unabsorbed is given by

$$P(\text{unabsorbed}_L) = \exp(-n\delta x\sigma_a)^{\frac{L}{\delta x}} = \exp(-n\sigma_a L). \quad (1.7)$$

Here, we see alignment with the Beer-Lambert law and we can define a characteristic length l_a [l] (or equivalently the absorption coefficient μ_a [l^{-1}]) that describes the thickness of absorbing medium where the exiting power is equal $\frac{1}{e}$ times the incident power.

1.2 Relevant Properties of Light

In addition to the properties which describe light-matter interaction, there are also several important properties of the light itself which we need to discuss. These include basic quantities such as wavelength, frequency, and energy as well as more advanced but nonetheless important properties such as coherence (spatial and temporal) and interference. In addition, after understanding these basic properties, we will more fully be able to understand the fundamental physics of different light sources and how they can be appropriately used in the development of optical tools.

We know that light is an electromagnetic wave that can be described by Maxwell's equations. The electromagnetic wave has a defined frequency that defines the number of periods through which the wave passes in one second. For the optical portion of the electromagnetic spectrum, these frequencies range from around 400 THz (red) to 700 THz (blue). Typically, in optics, we talk about the wavelength of light as opposed to its frequency. The wavelength and frequency are related by the speed of light as given by the following equation where λ is the wavelength with units of

length, ν is the frequency with units of inverse time, and c is the speed of light with units of length per unit time.

$$\lambda\nu = c \quad (1.8)$$

The energy of light is also an important quantity. It as well is related to the frequency of the light and is given by

$$E = h\nu, \quad (1.9)$$

where E is the photon energy, h is Planck's constant with units of energy times time, and ν which has units of inverse time.

Properties of light

More advanced properties of light are also important for describing the behavior of optical systems. One of these properties is coherence. Coherence has two main dimensions; temporal and spatial.

Temporal coherence

Temporal coherence describes the correlation of wave and a copy of itself delayed by a time τ . Temporal coherence can be quantified either as a coherence time τ_c , which is defined as the delay time after which the correlation drops below a specified value such as $1/e$, or a coherence length, which is equal to the coherence time multiplied by the speed of light to convert it into a unit of length. Often, the coherence length is a more convenient quantity since it has more direct implications on the physical design of optical systems.

To intuitively understand the concept of temporal coherence, we can imagine two cases. If we have an idealized continuous wave, single frequency source, the coherence length will be infinite since the wave will always perfectly correlate with itself, regardless of the delay time/length. The interference patterns for this source will always have a very high contrast and will exhibit strong constructive and destructive interference depending on the exact values of the delay time. A laser is an example of a source that is typically designed to have a very long coherence length since it contains a very narrow range of emitted frequencies.

Alternatively, if our source is composed of the sum of several different frequencies (e.g., light emitted from a wide-band light source such as a light emitting diode

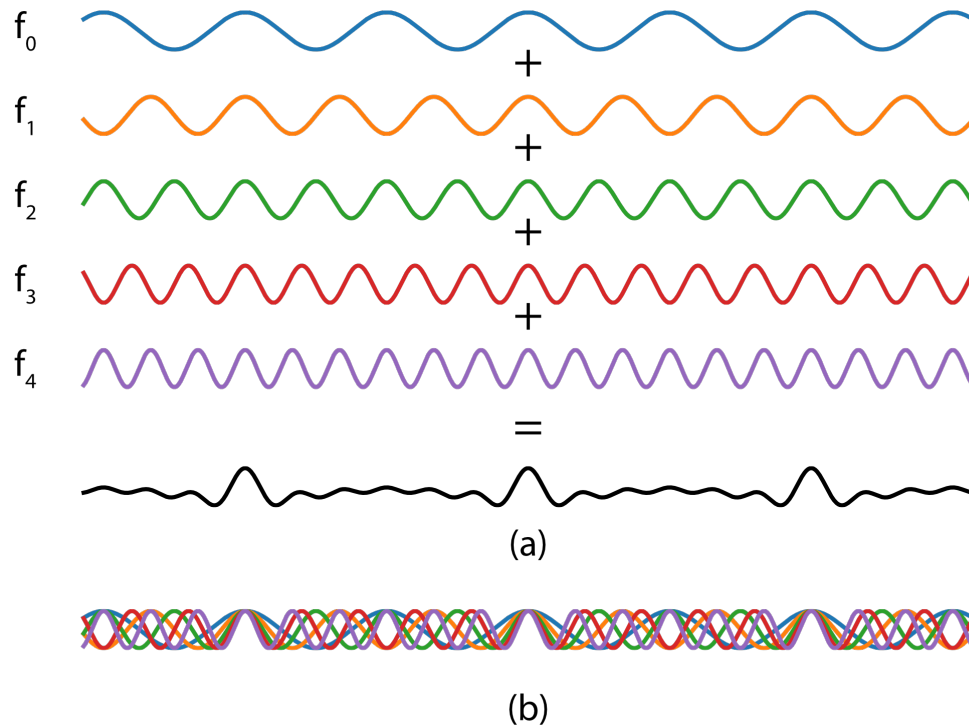


Figure 1.5: **A cartoon indicating the principle of temporal coherence.** When sinusoids of different frequencies add together, their resultant sum adds constructively or destructively depending on the phase relationship between the individual frequencies. The temporal coherence of a source is related to the range of frequencies that are contained in its emitted illumination. If a source emits only one frequency, then it has an infinite coherence length because it will interfere with itself regardless of the path length or phase delay between the original and delayed copies. However, if a beam contains multiple frequencies, there are only a finite range of path length delays over which the beam will interfere with itself and generate strong interference effects. (a) A figure illustrating how the sum of multiple frequencies generates a resultant sum which exhibits strong constructive interference when the phases align and many areas where the resultant sum destructively interferes. (b) An overlay of all the different frequencies. The points where the sinusoids are in phase generate the peaks seen in the sum shown in (a).

(LED)), this will yield a shorter coherence length. In this case, because the overall intensity of the resultant interference pattern is due to the summation of the individual frequencies, the resulting interference plot for different delay times is reduced. The reduction in correlation is directly determined by the spectral bandwidth (i.e., range of emitted frequencies) of the source. In addition to LEDs, short pulsed lasers are another type of light source that exhibits short coherence lengths. The operation of mode-locked lasers can make this connection particularly clear since the locked phase of different wavelengths causes the individual frequencies to phase in and out and create the resulting pulses.

Mathematically, we can describe the temporal coherence of a source using an autocorrelation function, $G(\tau)$, given by

$$G(\tau) = \langle U^*(t)U(t + \tau) \rangle \quad (1.10)$$

where $U(t)$ is a stationary random complex optical wavefunction representing the light source and τ is a delay time. The temporal autocorrelation function can be normalized by its value at $t = 0$ which is equivalent to the overall intensity of the source. This yields the normalized autocorrelation function given by

$$g(\tau) = \frac{\langle U^*(t)U(t + \tau) \rangle}{\langle U^*(t)U(t) \rangle}. \quad (1.11)$$

The value of $|g(t)|$ indicates the complex degree of temporal coherence of a source where $|g(\tau)| = 1$ indicates a perfectly correlated source and $|g(\tau)| = 0$ for a totally uncorrelated source.

Spatial coherence

Spatial coherence refers to the phase correlation of a wavefront and can be understood to represent how closely the light source corresponds to an ideal point source. Consider the Huygens-Fresnel principle, which states that each point on a wavefront acts as a new source of spherical wavefronts and a Young's double slit experiment. Assuming a temporal coherence length much longer than the path length difference between the light emitted from S_1 and arriving at the screen from the two slits, we expect to see an interference fringe pattern. S_2 will contribute a similar, shifted fringe pattern. The separation of P_1 and P_2 dictate the frequency of fringe pattern.

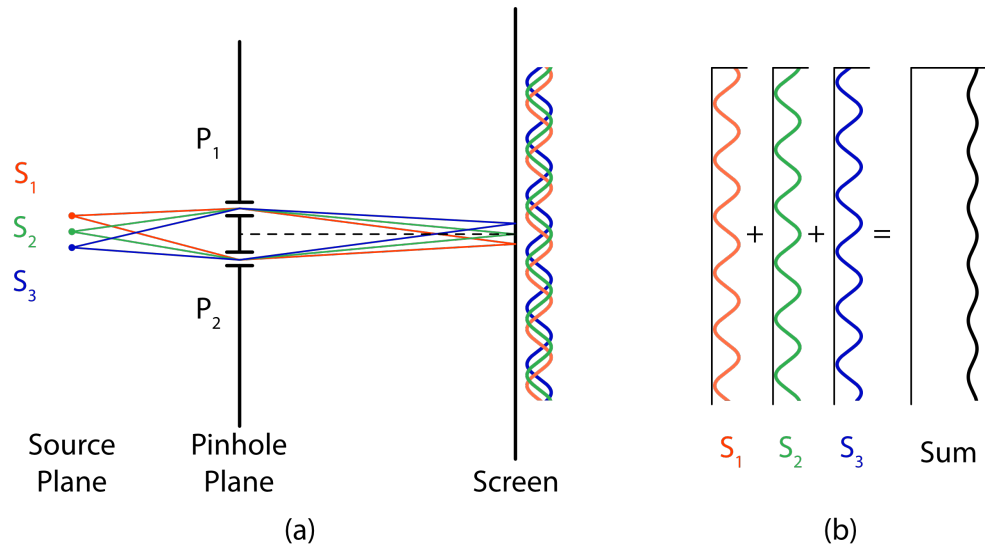


Figure 1.6: **A cartoon describing the principle of spatial coherence.** (a) Several sources S_1 , S_2 , and S_3 , illuminated two pinholes P_1 and P_2 . These sources generate fringe patterns on the screen. The number of independent sources or equivalently the spatial extent of the resulting extended source determines the spatial coherence of the source. (b) Summing the shifted fringe patterns from each of the individual sources generates a reduced contrast fringe pattern.

The argument of how we arrive at spatially incoherent illumination is very similar to the argument we just followed to arrive at temporally incoherent illumination. In the case where we only have one point source S_1 emitting light, we end up with a single fringe pattern, and if the source is a true point source (infinitely small) and the temporal coherence of the source is infinite (monochromatic), then the fringe pattern on the screen will be high contrast regardless of the separation distance of the pinholes P_1 and P_2 . If, however, we consider the addition of more point sources S_2 and S_3 , the situation will begin to change. This situation is illustrated in Figure 1.6(a) with the summation of the fringes and resulting reduction in fringe contrast shown in Figure 1.6(b).

We can consider each of these sources to be a source of additional plane waves, each contributing a laterally shifted fringe pattern on the screen. As we add up more and more shifted patterns, the effect will be to form a washed out fringe pattern. As a rule of thumb, if the angle subtended by the source is greater than $\theta_s = \lambda/d$, where λ is the wavelength and d is the separation distance between the pinholes, then the degree of spatial coherence will be very small. For more detailed analysis,

the reader is encouraged to consult reference [2].

Source properties and applications

When designing an optical system, it is critical to carefully choose a source with the appropriate properties. For example, we generally want to avoid strong absorption from water and depending on the application, may want to carefully choose our wavelength(s) to measure the absorption of blood or excite a particular molecule within the tissue. In other imaging applications, we may want to minimize the overall absorption to be able to image deep inside tissue. The coherence properties are also critically important and in particular, the temporal coherence properties of a source can help to improve the resolution and isolate signal photons by using interference as in imaging strategies such as optical coherence tomography (OCT) [3].

1.3 Interferometry

One of the challenges of working with the optical portion of the electromagnetic spectrum is that the frequency is very high. The high frequency (several hundred terahertz) is faster than electronic circuits can operate and therefore, unlike lower frequency signals like microwave or radio frequency signals, optical measurements do not have direct access to the complex (amplitude and phase) information of optical signals. Instead, optical measurements are most commonly made of the optical intensity, the time-averaged magnitude squared of the complex field ($I = |E|^2$), integrated over some measurement time. While the amplitude of the complex signal is simply the square root of the intensity $|E| = \sqrt{I}$, the phase information is lost. Unfortunately, in many optical applications, the phase information is very important as it carries valuable information about the optical field.

Fortunately, there are clever ways to encode the phase information into the intensity measurement so it can be directly measured. One such class of these methods uses interference with a known reference wave to perform this encoding. Within this thesis, two different types of these interference schemes are used: inline phase-shifting and off-axis holography. The concept of inline holography was originally proposed and demonstrated by Dennis Gabor in 1948 [4] as a way to improve electron microscopy and later further developed by Emmett Leith and Juris Upatnieks who invented off-axis holography. These interferometric methods not only enable measurement of the amplitude and phase of an optical field, but also have practical advantages which enable sensitive measurements to be made even with noisy detec-

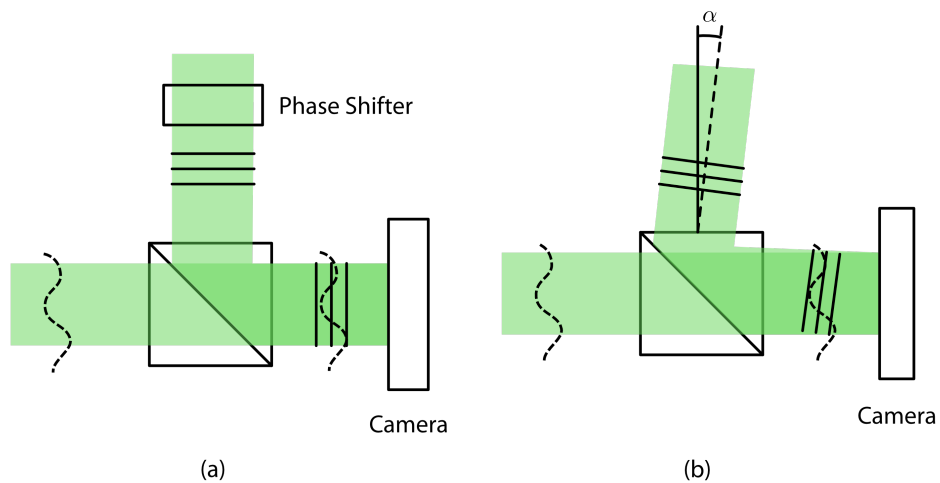


Figure 1.7: **Simple holography schemes.** (a) Phase shifting holography setup. The phase shifter (typically an electro-optic modulator (EOM) or delay line with translating mirror) is used to introduce phase shifts (optical path delays) between the sample and reference beams. (b) Off-axis holography setup. The reference beam is tilted by an angle of α with respect to the sample beam normal direction. This separates the sample and reference terms in the spatial frequency domain, enabling them to be retrieved from a single-shot measurement.

tors. The operation principles and respective trade-offs of these approaches will be described in the next sections.

Phase-shifting holography

In inline phase shifting holography, an unknown sample field $\mathbf{E}_s(\mathbf{x}) = |E_s| e^{-j\phi_s(\mathbf{x})}$ is combined with a known reference field $\mathbf{E}_r(\mathbf{x}) = |E_r| e^{-j\phi_r(\mathbf{x})}$ using a beam splitter as shown in Figure 1.7. There is no requirement on the exact form of the reference beam provided that it is known, but in practice, a collimated plane wave directed normal to the sensor plane is typically used for convenience. In this case, the reference beam expression can be simplified as $\mathbf{E}_r(\mathbf{x}) = |E_r| e^{-j\phi_r}$ where ϕ_r is now simply a constant offset, independent of the spatial position \mathbf{x} . After the sample and reference beams are combined, they are collected on a detector that measures the intensity of the interference pattern of the two beams. This can be described as the following:

$$I(\mathbf{x}) = \int_T |\mathbf{E}_s + \mathbf{E}_r|^2 = \int_T \mathbf{E}_s \mathbf{E}_s^* + \mathbf{E}_r \mathbf{E}_r^* + \mathbf{E}_s \mathbf{E}_r^* + \mathbf{E}_s^* \mathbf{E}_r \quad (1.12)$$

$$= \int_T E_s^2 + E_r^2 + 2E_s E_r \cos(\phi_s(\mathbf{x}) - \phi_r(\mathbf{x})) \quad (1.13)$$

where the * stand for complex conjugation.

We can see from this equation that the overall intensity is a function of the sample and reference intensities plus a term that contains the product of the sample amplitude, reference amplitude, and the cosine of the phase difference between the sample and reference beams. By changing the phase difference between the sample and reference beams, we can encode the phase difference information into the intensity. Normally, this is done by shifting the phase of the reference beam with respect to the sample beam with either a translating delay line or electro-optic modulator (EOM). By capturing at least three intensity measurements with different phase shifts, the phase of the sample beam can be reconstructed. For simplicity and signal to noise considerations, four different phase shift values are normally measured with relative phase difference of $\theta \in [0, \pi/2, \pi, 3\pi/2]$. In this case, the phase of the sample beam can be recovered using the simple equation below.

$$\phi_s = \tan^{-1} \left(\frac{I_{3\pi/2} - I_{\pi/2}}{I_{\pi} - I_0} \right) \quad (1.14)$$

The drawbacks of the phase shifting holography method is that it requires at least three frames to measure the phase of the sample. However, it enables full use of all the pixels in an area detector, since the phase is measured at each pixel.

Off-axis holography

Off-axis holography is an alternate way to measure the phase profile of a beam using interferometry. It was proposed in 1962 by Emmett Leith and Juris Upatnieks to address the issues of twin-image and zero-order contamination present in Gabor's inline holographic method [5]. The essential idea is to tilt the reference beam with respect to the sample beam so that it illuminates the sensor at an angle. This imposes a fringe pattern on the sample beam and separates the last term in Eq. 1.13 in the spatial frequency domain. If the reference beam is a tilted plane wave, the form of the reference beam changes to $\mathbf{E}_r(\mathbf{x}) = |E_r| e^{-jk(\sin\theta_x x + \sin\theta_y y)}$ where $k = \frac{2\pi}{\lambda}$ and θ_x

and θ_y are the tilt angles with respect to the x and y directions respectively. This yields an expression for the intensity given by

$$\begin{aligned} I(\mathbf{x}) &= \int_T |\mathbf{E}_s + \mathbf{E}_r|^2 = \int_T \mathbf{E}_s \mathbf{E}_s^* + \mathbf{E}_r \mathbf{E}_r^* + \mathbf{E}_s \mathbf{E}_r^* + \mathbf{E}_s^* \mathbf{E}_r \\ &= \int_T E_s^2 + E_r^2 + E_s e^{-j\phi_s(\mathbf{x})} E_r e^{jk(\sin\theta_x x + \sin\theta_y y)} + E_s e^{j\phi_s(\mathbf{x})} E_r e^{-jk(\sin\theta_x x + \sin\theta_y y)} \end{aligned} \quad (1.15)$$

By taking the 2-dimensional Fourier transform of the interferogram, the complex sample field can be spatially filtered and recovered via an inverse Fourier transform. If we look at the 2-d Fourier transform of the interferogram, it contains four terms.

$$\begin{aligned} \mathcal{F}(I) &= \mathcal{F}(E_s^2) + \mathcal{F}(E_r^2) \\ &\quad + \mathcal{F}(E_s e^{-j\phi_s(\mathbf{x})} E_r e^{jk(\sin\theta_x x + \sin\theta_y y)}) \\ &\quad + \mathcal{F}(E_s e^{j\phi_s(\mathbf{x})} E_r e^{-jk(\sin\theta_x x + \sin\theta_y y)}) \end{aligned} \quad (1.16)$$

The first two terms are the autocorrelation terms (Fourier transform of the sample and reference intensity distributions respectively). The sample autocorrelation will be a function with twice the bandwidth of the sample function. Since the reference beam is a plane wave, its autocorrelation function is a delta function centered at the origin in the spatial frequency domain. The last two terms are the off-axis lobes which contain the complex information about the sample. We can see that these terms contain the Fourier transform of the sample field multiplied by the tilted reference plane wave field. The amplitude of the reference field (E_r) is a constant and the phase term of the reference is a phase ramp. According to the Fourier shift theorem, a phase shift in the spatial domain manifests as a spatial shift in the spatial frequency domain, and so the effect of this tilted phase ramp is to shift the spatial frequency content of the sample field to a higher spatial frequency and multiply it by the reference field amplitude.

The major advantage of off-axis holography compared to phase-shifting holography is that it enables the complex sample field to be measured in a single shot. However, this comes with a cost since the signal must be band-limited such that it can be appropriately separated in the spatial frequency domain. This can be understood by looking at a cartoon of the spatial frequency domain. To avoid aliasing, the goal is

to fit the off-axis lobes in the spatial frequency domain without overlapping it with the sample or reference beam autocorrelation. Since the reference beam is a plane wave whose autocorrelation is a delta function centered at zero spatial frequency, the main challenge to avoid aliasing is to avoid overlapping of the sample field autocorrelation and the off-axis lobes. If the spatial bandwidth of the sample is B then it can be represented in the spatial frequency domain as a circle with diameter B and its autocorrelation function as a circle with diameter $2B$. Therefore, the signal bandwidth B and reference beam tilt angles (θ_x, θ_y) must be controlled so that the information is separated in the spatial frequency domain. Then, the signal can be recovered by taking a 2D Fourier transform of the interferogram, cropping out one of the off-axis lobes, and the inverse 2D Fourier transform. Interested readers are referred to reference [6] for more details about reconstruction methods.

Shot-noise-limited detection

Another important benefit of interferometry is that it enables shot-noise-limited detection. Maximizing the signal-to-noise ratio (SNR) of an optical system is an important goal, particularly when dealing with biological samples that can only be exposed to a limited amount of intensity before thermal and chemical damage can occur. There are many sources of noise that can degrade a system's SNR. Some of the most common of these include various types of detector noise (e.g., dark current noise and readout noise), quantization noise, laser noise, and fluctuations in temperature or air flow. However, even if all of these sources are minimized or eliminated, there is a fundamental limit to the SNR that can be achieved by an optical system due to the quantized nature of light. The noise that is a result of this quantized nature is referred to as shot noise or Poisson noise and is the fundamental upper bound for the SNR of optical measurements.

Given a signal of N , the Poisson noise of the signal is given by \sqrt{N} . Therefore, the SNR for shot noise is given by

$$\text{SNR} = \left(\frac{N}{\sqrt{N}} \right)^2 = N \quad (1.17)$$

To understand the limitations of shot noise, let's consider the example of an outdoor showerhead in a rainstorm as shown in Figure 1.8. We want to know the minimum average rainfall rate of the showerhead necessary in order to tell whether it is on or not compared to the shot noise of the raincloud. The average rainfall rate from

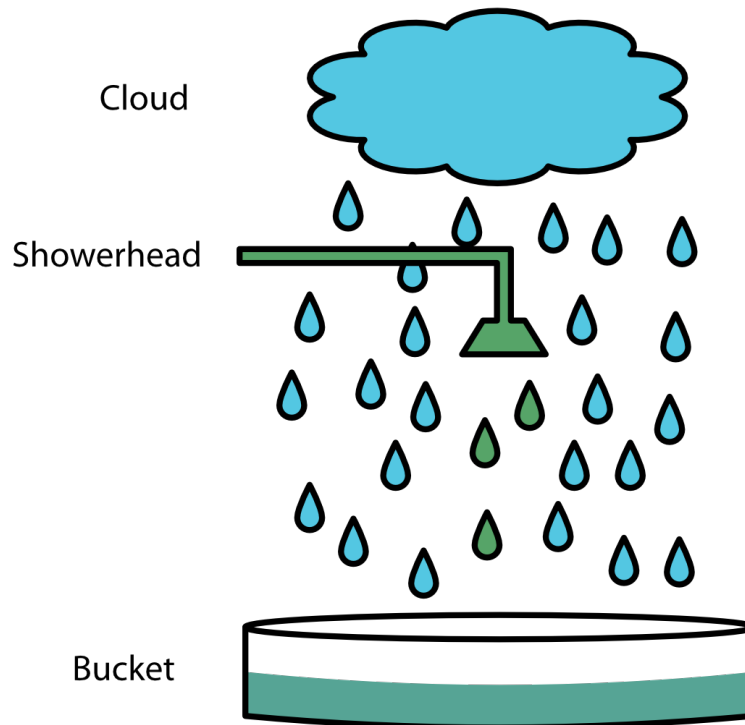


Figure 1.8: **Shot noise explanation with a raincloud and showerhead.** Consider the following case of a showerhead in a rainstorm. We want to analyze the average rainfall rate necessary from the showerhead for us to be able to determine whether or not it is on.

the cloud is N_{cloud} , the average rainfall rate of the showerhead is $N_{\text{showerhead}}$, and $N_{\text{cloud}} \gg N_{\text{showerhead}}$. Therefore, the average number of raindrops detected within a measurement time T is given by:

$$S_{\text{total}} = (N_{\text{showerhead}} + N_{\text{cloud}}) \cdot T \quad (1.18)$$

The SNR of this situation is given by

$$\text{SNR} = \left(\frac{S_{\text{total}}}{\sqrt{S_{\text{total}}}} \right)^2 \quad (1.19)$$

$$= \left(\frac{N_{\text{showerhead}} \cdot T}{\sqrt{(N_{\text{showerhead}} + N_{\text{cloud}}) \cdot T}} \right)^2. \quad (1.20)$$

This means that to have an $\text{SNR} > 1$, we need

$$N_{\text{showerhead}} \cdot T \geq \sqrt{(N_{\text{showerhead}} + N_{\text{cloud}}) \cdot T}. \quad (1.21)$$

Using the fact that $N_{\text{rain}} \gg N_{\text{showerhead}}$, we can further simplify this to

$$N_{\text{showerhead}} \geq \sqrt{N_{\text{cloud}}}. \quad (1.22)$$

From this analysis, we can see that in order to distinguish whether or not the showerhead is on, we must have the average rainfall rate from the showerhead exceed the square root of the average rainfall rate from the raincloud.

So what does this have to do with interferometry? If we translate our raindrop analysis to photons, we can see that to measure the signal from a source on top of a large background, we need to ensure that the average photon rate is greater than the square root of the photon rate from other noise sources. Ideally, we want to be limited only by the shot noise of our signal, but if we have a noisy detector, the dark noise and readout noise contribute photoelectrons to our accumulated signal that are indistinguishable from photoelectrons generated by our source. Interferometry can help by enabling us to achieve sample shot noise limited detection even when we have a noisy detector which would normally swamp our signal.

To analyze this we can refer back to our interference equation (Equation 1.13), reprinted below for the reader's convenience and slightly modified to simplify the terminology. Here the signal and reference beam powers are given by P_s and P_r respectively.

$$I = P_s + P_r + \sqrt{P_r P_s} + n_{\text{detector}} \quad (1.23)$$

In this equation, our signal term is the third term in the equation, and the first two terms form a strong background signal. Finally, here we also add a noise term, n_{detector} , to represent the detector noise. Therefore, our SNR in this situation is given by

$$\text{SNR}_{\text{Interferometry}} = \left(\frac{\sqrt{P_r P_s}}{\sqrt{P_s + P_r + n_{\text{detector}}}} \right)^2. \quad (1.24)$$

In this situation, making the safe assumption of a large dynamic range for our detector, we can boost the reference beam power P_r so that it swamps the shot noise from the signal and detector noise terms. Therefore, the SNR equation becomes

$$\begin{aligned}\text{SNR}_{\text{Interferometry}} &= \left(\frac{\sqrt{P_r P_s}}{\sqrt{P_r}} \right)^2 \\ &= P_s.\end{aligned}\tag{1.25}$$

In contrast, the SNR in the homodyne case without a reference beam and a perfect (noiseless detector) is given by

$$\begin{aligned}\text{SNR}_{\text{Homodyne}} &= \left(\frac{P_s}{\sqrt{P_s}} \right)^2 \\ &= P_s,\end{aligned}\tag{1.26}$$

where the signal is the DC signal P_s and the noise is given by the shot noise of the sample beam $\sqrt{P_s}$.

This shows a remarkable result, namely that if we use a reference beam and a detector with sufficient dynamic range, we can achieve the same SNR as we can with a perfect, noiseless detector! This means that interferometry can be very helpful, enabling us to measure even very weak optical signals with shot-noise-limited performance. This is in addition to the usefulness of measuring the phase of an optical wavefront. In the particular, when we are dealing with biological samples, this is very useful since we want to minimize the power we expose our sample to without sacrificing SNR.

1.4 Light propagation through disordered media

Next we will investigate how light scatters as it propagates through disordered media and ways to model this process.

Elastic scattering regimes

When the refractive index of a material is spatially inhomogeneous (i.e., $n(\mathbf{r})$ is not a constant), light propagating through the material no longer follows a straightforward propagation as in free space. This is due to the fact that when light encounters a boundary between materials with two different refractive indices, it diffracts and

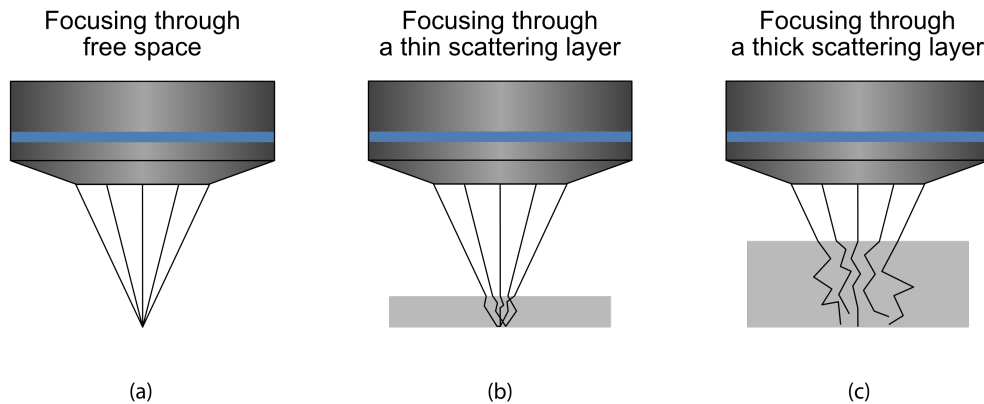


Figure 1.9: **Scattering regimes.** (a) In free space, conventional lenses form the correct wavefronts to focus light to tight focal spots. (b) When the scattering medium is thin and the thickness is less than the mean free path ($L < l$), most of the light is unscattered and conventional lenses can still form relatively tight focal spots. (c) Once the thickness exceeds the transport mean free path ($L > l^*$), conventional lenses can no longer form effective focal spots since almost all the light has been multiply scattered and very little ballistic light remains.

refracts. These processes more generally are referred to as elastic scattering, because the wavelength of light is not changed due to the scattering interaction. This is in contrast to other inelastic scattering process such as Raman or Brillouin scattering where the scattered photons are of different energies than the incoming photons.

There are three major regimes of scattering strength in the context of scattering media. The first regime is in the optically thin region where the thickness of the scattering media is on the order of the scattering mean free path. In this limit, most of the photons experience at most a single scattering event. However, as the scattering medium becomes more optically dense (i.e., the ratio of physical thickness to mean free path increases), then photons experience more scattering events. In this regime, most photons travelling through the scattering medium are scattered several times. Once the medium becomes sufficiently thick (thicker than one transport mean free path), the probability of ballistic photons passing through the medium becomes vanishingly small. In this limit, the propagation of light can be described as diffusive and is well described by diffusion equations [7].

Time-reversal symmetry of the wave equation

Although the heterogeneous refractive index distributions in scattering media present a challenge for focusing light through them, the physics of the wave equation can help to simplify the situation. Among the most important properties of the wave equation for sending light through scattering media is the time-reversal symmetry of the wave equation. In the linear regime, the electric field $\mathbf{E}(\mathbf{r}, t)$ of an electromagnetic wave can be described by the wave equation

$$\mu(\mathbf{r})\epsilon(\mathbf{r})\frac{\partial^2\mathbf{E}}{\partial t^2} = \nabla^2\mathbf{E}, \quad (1.27)$$

where ϵ and μ are the position dependent electric and magnetic permeabilities of the medium, respectively. Recalling that the refractive index is defined as $n = \sqrt{\epsilon_r\mu_r}$ where $\epsilon_r = \frac{\epsilon}{\epsilon_0}$ and $\mu_r = \frac{\mu}{\mu_0}$ are the relative electric and magnetic permeabilities, this gives a wave equation in terms of the local refractive index as

$$\frac{n(\mathbf{r})^2}{c_0^2}\frac{\partial^2\mathbf{E}}{\partial t^2} = \nabla^2\mathbf{E}, \quad (1.28)$$

where c_0 is the speed of light in vacuum.

The time-reversal symmetry property means that if $E(\mathbf{r}, t)$ is a solution to the wave equation, then $E(\mathbf{r}, -t)$ is also a valid solution. For example, if $E(\mathbf{r}, t)$ is a spherical wave emanating from a source, then $E(\mathbf{r}, -t)$ is a spherical wave converging back toward the source. In the context of scattering media, this means that the time-reversed copy of a scattered light field will reverse its course through the scattering medium and converge at its original source. The benefits of using time-reversal to send waves through scattering media was first discovered and developed by Matthias Fink and colleagues using ultrasonic waves in the late 1980s. Interested readers are directed to reference [8] for more detailed information.

Transmission Matrix

Another important tool in our discussion about sending light through scattering media is the transmission operator. This operator (which can be discretized and modeled as a matrix) describes the complex mapping between the input and output electric fields of light passing through a scattering medium. Each element of the matrix therefore describes the amplitude and phase relationship between one input

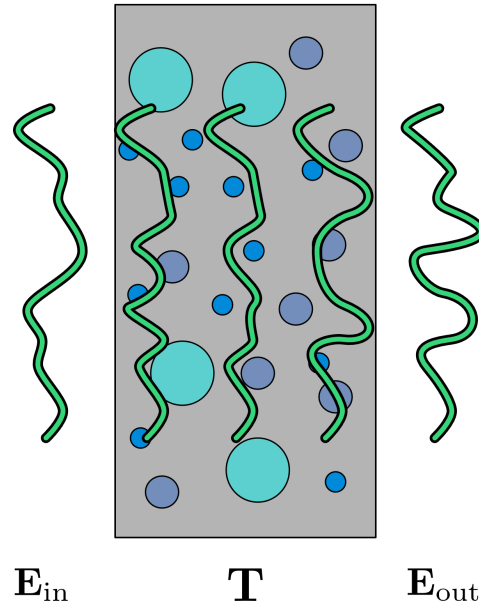


Figure 1.10: **A an example of the transmission matrix terminology for wavefronts passing through scattering media.** The input field \mathbf{E}_{in} passes through the transmission matrix \mathbf{T} which maps it onto the output field \mathbf{E}_{out} .

and output mode. While the concept of the transmission matrix is a general one in engineering, it has only been in the past decade that this concept has been explored in optics due to the growing availability of tools such as highly sensitive and fast cameras, which enable precise measurement of many optical modes, and spatial light modulators (SLMs), which enable the manipulation of many individual optical modes. Figure 1.10 and Equation 1.30 show a schematic and mathematical description of how the transmission matrix is defined.

$$E_{\text{out}} = T E_{\text{in}} \quad (1.29)$$

$$\begin{bmatrix} E_{\text{out}_1} \\ E_{\text{out}_2} \\ \vdots \\ E_{\text{out}_m} \end{bmatrix} = \begin{bmatrix} t_{11} & t_{12} & \cdots & t_{1n} \\ t_{21} & t_{22} & \cdots & t_{2n} \\ \vdots & \vdots & \ddots & \vdots \\ t_{m1} & t_{m2} & \cdots & t_{mn} \end{bmatrix} \begin{bmatrix} E_{\text{in}_1} \\ E_{\text{in}_2} \\ \vdots \\ E_{\text{in}_n} \end{bmatrix} \quad (1.30)$$

After we know the transmission matrix of a scattering medium we can use it to control light through the scattering medium by applying the appropriate input light

field pattern. Furthermore, the fact that wave propagation is time-symmetric means that time-reversal can be used to find the appropriate input light patterns. As demonstrated in reference [9] by Popoff and colleagues, one can use the time-reversal operator to find the correct input field E_{in} to use in order to obtain a desired output field E_{target} . In the case where the input light is monochromatic, time-reversal is the same as a phase conjugation. Therefore, the optimized pattern to generate an output target field E_{target} , is given by

$$E_{\text{in}} = T^\dagger E_{\text{target}}, \quad (1.31)$$

where the \dagger indicates conjugate transpose.

When inputting this input field, the resulting output is given by

$$E_{\text{out}} = O_{\text{foc}} E_{\text{in}} \quad (1.32)$$

where the operator $O_{\text{foc}} = T^\dagger T$ is called the time-reversal operator.

To further analyze the properties of this matrix, we can perform a singular value decomposition of the matrix. This will decompose the $m \times n$ time-reversal matrix O_{foc} into the form

$$O_{\text{foc}} = U \Sigma V^*, \quad (1.33)$$

where U is an $m \times m$ complex unitary matrix whose columns are the left singular vectors, Σ is an $m \times n$ with non-negative real numbers on the diagonal, and V is an $n \times n$ complex unitary matrix whose columns are the right singular vectors. In the context of the transmission matrix, the U acts to map the input modes onto the eigenmodes of the system, Σ contains the eigenvalues of the time-reversal operator matrix, and V acts to map the eigenmodes onto the output modes.

The distribution of the singular values of the transmission matrix is worth briefly discussing. For a lossless system (e.g., a medium surrounded by perfectly reflecting walls and no absorption), the singular values follow a bimodal distribution. This situation enforces a correlation between the transmission matrix elements and produces singular values that are either close to one or close to zero. However, in real

situations such as scattering in biological tissue, although absorption is low, the total energy is not conserved due to the limited collection efficiency. This causes the transmission matrix elements to become uncorrelated and follow a random, complex Gaussian distribution and, as follows from random matrix theory, the singular value distribution obeys a Marchenko-Pastur or quarter-circle distribution where nearly all the open channels have disappeared. Further details and additional papers for those interested are discussed in reference [9].

1.5 Wavefront shaping

However, even though the open channels begin to disappear, the presence of partially open channels means that we can still control the light propagation through the scattering medium. Since the transmission matrix is a linear amplitude and phase mapping between input modes and output modes, the output field at a particular point can be enhanced.

Wavefront shaping in optics was first demonstrated in 2007 by Vellekoop and Mosk [10]. In essence, the goal of creating a focus is to create a point of constructive interference through the scattering media and cause the contributions from individual output modes to align in phase. When we send coherent light through a scattering medium, the resulting output light field manifests as a "speckle" pattern. This is due to the random nature of the transmission matrix and is due to the random interference of the contributions from different output modes. At a given output mode, we can visualize the situation as a phasor diagram, where each individual phasor represents the amplitude and phase contribution at the selected output mode from a collection of input modes.

At each output mode, these phasors interfere, and the random interference can be modeled as a 2D random walk in the complex plane [11]. An example of this type of random interference is shown in Figure 1.11(a). However, if we have a way to control the input field, we can use the fact that the system is linear to rotate the phasors in the complex plane so that they are aligned and in phase with one another as shown in Figure 1.11(b). This generates a strong resultant intensity at the output optical mode of interest as demonstrated by the increased length of the red resultant vector in Figure 1.11(b) compared to Figure 1.11(a). Since the transmission matrix elements are in general uncorrelated, this means that by rotating the phasors, we can create strong constructive interference at a location of interest, while the intensity at other output modes remains random and acts as a 2D random walk in the complex

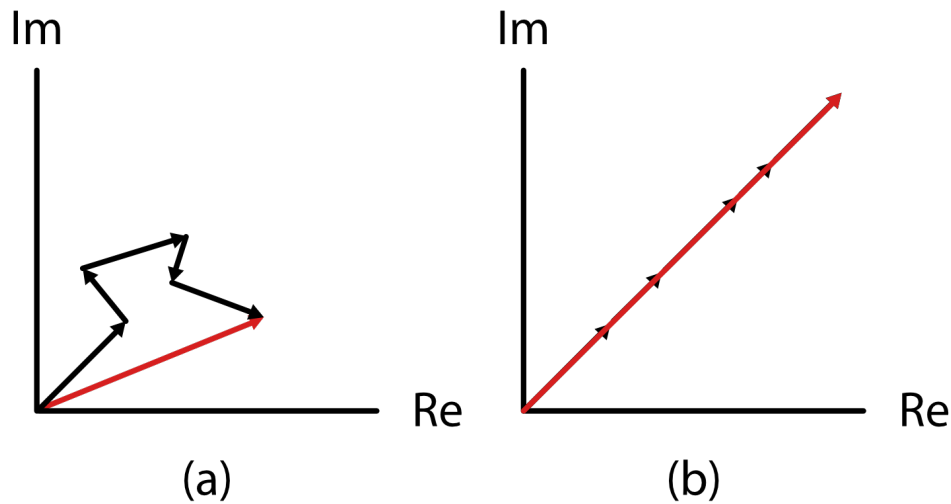


Figure 1.11: **Phasor diagram illustrating the interference of different modes in a speckle pattern.** (a) If the phasors are not aligned, they follow a 2D random walk in the complex plane. The red vector indicates the resultant phasor sum. (b) If the phasors are controlled via wavefront shaping, the phasors can be rotated so that they are in phase with one another to form a constructive interference peak. This creates an enhancement in the intensity at the point of interest given by the increase in the length of the resultant vector in (b) compared to (a).

plane.

Another point of practical benefit is that this control doesn't require full control of both the amplitude and phase of the input field. While amplitude control would enable us to change the length of the vectors, we can see that control over the phase alone (allowing us to rotate the vectors in the complex plane) is enough to enable an enhancement at the output mode of interest. To do this, we simply adjust the phase of the phasors, thereby rotating them to maximize the length of the resultant vector. This is useful because it is much easier in practice to control either the phase or amplitude only of an input field with a spatial light modulator instead of simultaneously controlling both.

Wavefront shaping in practice

There are several ways to find the optimal input field to create a focus at a desired output mode or location in practice. These fall into two main classes: feedback- and time-reversal-based methods. In feedback-based methods, an output metric can be monitored and maximized while different combinations of input patterns are

displayed. There are a variety of different feedback-based methods that have been developed and are nicely described in a recent review, reference [12].

The main drawback of feedback-based wavefront shaping methods is that they are slow because many measurements need to be made. This problem is solved by the time-reversal-based methods. With time-reversal, we use a source of coherent light emanating from a point of interest through or inside the scattering medium and measure the scattered wavefront corresponding to this source. Then, by creating the time-reversed or phase-conjugated version of that scattered wavefront, light can be focused back on the original point source. The advantage of this method is that it can achieve fast focusing speeds, since it requires only a single measurement of the scattered field in comparison to feedback-based methods, which require many measurements to form a high fidelity focus. However, this method requires a much more complicated optical setup to perform the time-reversal. This was originally demonstrated with an analog time-reversal mirror based on a photorefractive crystal [13] but now is commonly accomplished using a digital time-reversal mirror composed of a camera and spatial light modulator [14]. While this digital implementation increases the flexibility of the system and enables more energy to be played back in the time-reversed wavefront compared to the analog systems, it requires precise, pixel-to-pixel alignment of the camera and spatial light modulator which makes the system challenging to build, even with the development of algorithms to help with the alignment procedure [15].

Wavefront shaping with guidestars

Up until now, we have discussed how wavefront shaping can help to focus light *through* scattering medium, but for practical applications, we want to focus light *inside* scattering media like biological tissue. To do this, we need an additional component in our wavefront shaping system called a guidestar. Borrowed from concepts in astronomy where stars serve as effective point sources outside the atmosphere to help find the correct wavefront solution for the deformable mirrors on the earth's surface to correct for the aberration of the atmosphere, guidestars in the context of wavefront shaping provide information about the correct wavefront solution to focus at a point inside the tissue.

Guidestars can be used with both feedback- or time-reversal-based wavefront shaping systems, although not all guidestars are compatible with both. The guidestar mechanisms that have been developed fall into three main categories: light-based,

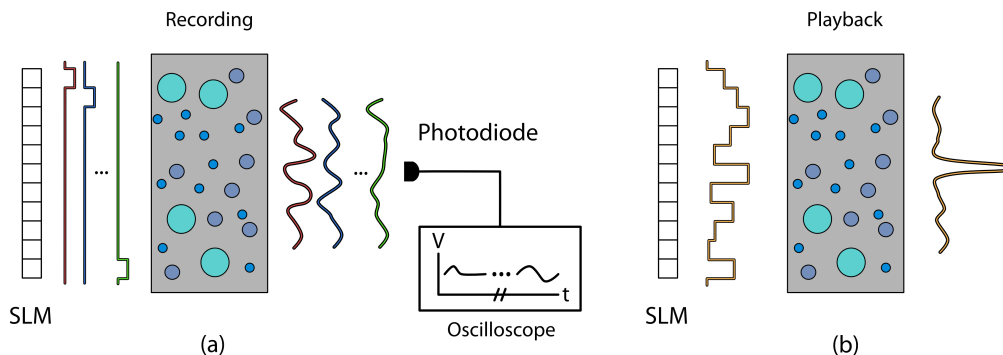


Figure 1.12: **Feedback-based wavefront shaping.** Feedback-based wavefront shaping uses a signal from a desired focal location as a feedback signal and creates different, orthogonal input patterns to maximize the intensity at that location. (a) In a basic scheme, a photodiode can be used to measure the light intensity at a given output point as different input patterns are displayed on a spatial light modulator (SLM). (b) After measuring several patterns, a best pattern can be composed to enhance the light at the desired location.

kinetic, and ultrasound-based guidestars. Light-based guidestars include approaches using fluorescence, second-harmonic generation, and absorption. These techniques are generally simple, but suffer from low efficiency and are often incompatible with time-reversal methods, since they generally do not generate coherent light.

Kinetic guidestars use the movement of an object inside the scattering sample as the signal for optimization. The most basic example of a kinetic guidestar is a moving particle as demonstrated in Time Reversal by Analysis of Changing wavefronts from Kinetic targets (TRACK) [16] or Time-Reversed Adapted-Perturbation (TRAP) focusing [17]. The basic idea of both of these techniques is to capture two wavefronts where the only change between the wavefronts is due to the movement of a particle. Then, by taking the difference between the two wavefronts, the resulting wavefront is the wavefront solution to send light back to the source of the movement. Both TRACK and TRAP focusing are compatible only with time-reversal based wavefront shaping methods. Other kinetic guidestars include magnetic particles [18] that can be externally controlled. These carry the advantage that they can be non-invasively controlled and moved as desired, and don't rely on the natural movement of the particle as in TRACK and TRAP focusing. In general, the kinetic guidestars have the advantage of being compatible with time-reversal methods, which means they can be fast and therefore potentially useful for biological applications. However,

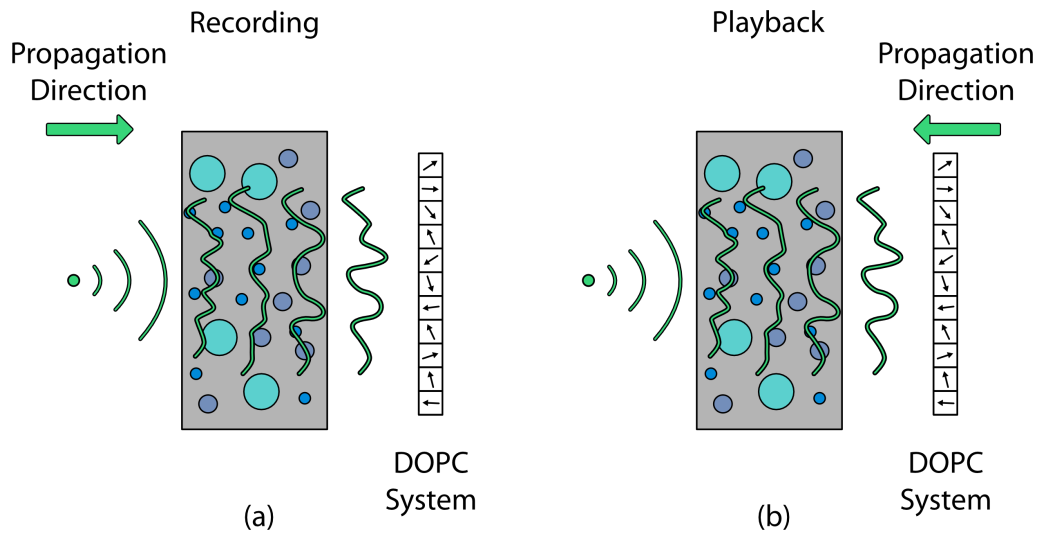


Figure 1.13: **Time-reversal-based wavefront shaping.** Time-reversal-based wavefront shaping uses the scattered light from a source of light within the sample and then sends a time-reversed copy of that wavefront back into the scattering medium to focus back on the location of the original source. The operation is broken down into two stages (a) recording and (b) playback. (a) In the recording stage, the scattered wavefront from a guidestar or location of interest is measured. (b) In the playback stage, the time-reversed copy of the wavefront is generated and displayed on the spatial light modulator (SLM). This time-reversed copy scatters back through the medium and constructively interferes to form a focus at the location of the original light source.

the downside of these methods is that they require the physical implantation of an external particle or rely on moving objects like red blood cells in the tissue to create a focus that reduces the control over the focusing location.

Ultrasound-based techniques such as time-reversed ultrasonically-encoded (TRUE) light focusing [19] use the acousto-optic effect to generate a source of coherent light that can be measured and used to create an optical focus at the location of the ultrasonic focus. While the ultrasound guidestar can be used with feedback-based approaches, it is most often used with time-reversal methods since it is compatible with them. The major benefits of the ultrasound guidestar are that it can be freely addressed to a desired location of interest by moving the ultrasound focus, and that it is non-invasive since it does not require a physical guidestar to be implanted. These two qualities make it well-suited for biological applications. This guidestar will be revisited in more detail when it is applied in Chapter 4.

1.6 Decorrelation

The preceding description of the transmission matrix and wavefront shaping assumes that the system is stable in time and that the matrix elements are fixed. However, if the configuration of the scattering medium changes (e.g., particles in a suspension move due to convection or Brownian motion, blood flows through a tissue sample, or a sample moves due to mechanical instability), the elements of the transmission matrix will also change. We call this process decorrelation since the transmission matrix elements lose correlation over time. In practice, when we want to focus light through or inside a scattering medium, we rely on the time-symmetry of the medium and stability of the transmission matrix to do so. Movement breaks the time-symmetry of the wave equation. This means that the time-reversed wavefront solution that would normally create a strong focus at the location of interest is no longer valid.

For practical applications, the speed at which this decorrelation takes place is very important, since it sets the boundaries of what practical applications can be addressed with wavefront shaping. Therefore, knowing this decorrelation speed for a particular type of medium is important.

1.7 Outline of this thesis

The remainder of this thesis is structured as follows. Chapter 2 investigates the decorrelation procedure in acute rat brain slices and its relationship to the tissue thickness in the absence of blood flow. Chapter 3 extends this investigation to the mouse brain *in-vivo* and compares the decorrelation times with those found in the absence of blood. This helps to establish bounds for the practical applications of wavefront shaping technologies and also provides guidance for future technology development.

Next, we explore the practical application of time-reversed ultrasonically-encoded (TRUE) light focusing in brain tissue to improve light delivery for optogenetics in Chapter 4.

Chapter 5 describes how we can use the decorrelation of a medium as a signal to tease out information about the dynamics of the sample and relate it to procedures within the tissue such as neural activity, which is coupled to the decorrelation through changes in the blood flow dynamics.

References

- [1] H. C. Hulst, *Light scattering by small particles*. Courier Corporation, 1981.
- [2] J. W. Goodman, *Statistical optics*. John Wiley & Sons, 2015.
- [3] D. Huang, E. A. Swanson, C. P. Lin, J. S. Schuman, W. G. Stinson, W. Chang, M. R. Hee, T. Flotte, K. Gregory, C. A. Puliafito, *et al.*, “Optical coherence tomography,” *science*, vol. 254, no. 5035, pp. 1178–1181, 1991.
- [4] D. Gabor, “A new microscopic principle,” *Nature*, vol. 161, pp. 777–778, 1948.
- [5] E. N. Leith and J. Upatnieks, “Reconstructed wavefronts and communication theory,” *JOSA*, vol. 52, no. 10, pp. 1123–1130, 1962.
- [6] N. Verrier and M. Atlan, “Off-axis digital hologram reconstruction: Some practical considerations,” *Applied Optics*, vol. 50, no. 34, H136–H146, 2011.
- [7] L. V. Wang and H.-i. Wu, *Biomedical optics: principles and imaging*. John Wiley & Sons, 2012.
- [8] M. Fink, “Time reversal of ultrasonic fields. i. basic principles,” *IEEE transactions on ultrasonics, ferroelectrics, and frequency control*, vol. 39, no. 5, pp. 555–566, 1992.
- [9] S. Popoff, G. Lerosey, R. Carminati, M. Fink, A. Boccarda, and S. Gigan, “Measuring the transmission matrix in optics: An approach to the study and control of light propagation in disordered media,” *Physical Review Letters*, vol. 104, no. 10, p. 100601, 2010.
- [10] I. M. Vellekoop and A. Mosk, “Focusing coherent light through opaque strongly scattering media,” *Optics Letters*, vol. 32, no. 16, pp. 2309–2311, 2007.
- [11] J. W. Goodman, *Speckle phenomena in optics: theory and applications*. Roberts and Company Publishers, 2007.
- [12] I. M. Vellekoop, “Feedback-based wavefront shaping,” *Optics Express*, vol. 23, no. 9, pp. 12189–12206, 2015.
- [13] Z. Yaqoob, D. Psaltis, M. S. Feld, and C. Yang, “Optical phase conjugation for turbidity suppression in biological samples,” *Nature Photonics*, vol. 2, no. 2, p. 110, 2008.
- [14] M. Cui and C. Yang, “Implementation of a digital optical phase conjugation system and its application to study the robustness of turbidity suppression by phase conjugation,” *Optics Express*, vol. 18, no. 4, pp. 3444–3455, 2010.
- [15] M. Jang, H. Ruan, H. Zhou, B. Judkewitz, and C. Yang, “Method for auto-alignment of digital optical phase conjugation systems based on digital propagation,” *Optics Express*, vol. 22, no. 12, pp. 14054–14071, 2014.

- [16] E. H. Zhou, H. Ruan, C. Yang, and B. Judkewitz, “Focusing on moving targets through scattering samples,” *Optica*, vol. 1, no. 4, pp. 227–232, 2014.
- [17] C. Ma, X. Xu, Y. Liu, and L. V. Wang, “Time-reversed adapted-perturbation (TRAP) optical focusing onto dynamic objects inside scattering media,” *Nature Photonics*, vol. 8, no. 12, p. 931, 2014.
- [18] H. Ruan, T. Haber, Y. Liu, J. Brake, J. Kim, J. M. Berlin, and C. Yang, “Focusing light inside scattering media with magnetic-particle-guided wavefront shaping,” *Optica*, vol. 4, no. 11, pp. 1337–1343, 2017.
- [19] X. Xu, H. Liu, and L. V. Wang, “Time-reversed ultrasonically encoded optical focusing into scattering media,” *Nature Photonics*, vol. 5, no. 3, pp. 154–157, 2011.

Chapter 2

THE RELATIONSHIP BETWEEN DECORRELATION AND TISSUE THICKNESS IN ACUTE RAT BRAIN TISSUE SLICES

*This chapter is adapted from the manuscript J. Brake[†], M. Jang[†], and C. Yang, “Analyzing the relationship between decorrelation time and tissue thickness in acute rat brain slices using multispeckle diffusing wave spectroscopy,” *JOSA A*, 33(2), pp. 270–275, 2016.*

2.1 Abstract

Novel techniques in the field of wavefront shaping have enabled light to be focused deep inside or through scattering media such as biological tissue. However, most of these demonstrations have been limited to thin, static samples since these techniques are very sensitive to changes in the arrangement of the scatterers within. As the samples of interest get thicker, the influence of the dynamic nature of the sample becomes even more pronounced and the window of time in which the wavefront solutions remain valid shrinks further. In this chapter, we examine the time scales upon which this decorrelation happens in acute rat brain slices via multispeckle diffusing wave spectroscopy and investigate the relationship between this decorrelation time and the thickness of the sample using diffusing wave spectroscopy theory and Monte Carlo photon transport simulation.

2.2 Wavefront shaping and decorrelation time

The optical opacity of biological tissue in the visible regime has long been a challenge in the field of biomedical optics. Since the light traveling through thick samples undergoes many scattering events, the information about the sample is scrambled and the light field exiting the sample forms a random speckle pattern [1].

While this scrambling of the light field makes it difficult to accurately image thick, highly scattering biological samples with conventional optical techniques, new research in the field of wavefront shaping enables light to be focused in or through strongly scattering tissue and has demonstrated progress toward this goal of deep tissue imaging [2–6]. In contrast to techniques such as confocal microscopy or optical coherence tomography (OCT), which seek to gate out and use only the

unscattered or singly-scattered portion of light passing through the sample, these wavefront shaping techniques incorporate even multiply scattered portions of the scattered light field.

While these wavefront shaping techniques have been primarily demonstrated with static scattering samples or fixed biological tissues, the ability to apply these techniques to living biological tissues is the ultimate goal. The main challenge facing this development is the dynamic nature of living tissue. In biological tissue where the average number of scattering events for an individual photon traveling through the sample is very large, small changes in the composition of the sample can break the time-reversal symmetry of optical scattering and cause a mismatch between the shaped wavefront and the correct wavefront solution, severely degrading the quality of the shaped focus. From previous studies, it is known that this degradation is proportional to the intensity autocorrelation function of the scattered light - a conventional measure of scatterer movement [7].

In this study, we measure the intensity autocorrelation function of acute brain tissue slices from rats and examine the relationship between the characteristic decorrelation time and tissue thickness, comparing the results with the theoretical predictions of diffusing wave spectroscopy (DWS), which suggest that the decorrelation time should be inversely proportional to the square of the thickness [8–12]. The results of this study elucidate the timescale on which the movement inside tissue occurs and guide the further development of fast wavefront shaping techniques, especially toward the development of improved light delivery techniques for optogenetics both on *in vitro* acute brain slices and eventually for *in vivo* applications [13–16].

2.3 Multispeckle diffusing wave spectroscopy

The wave nature of light allows for very small changes in optical path length to be probed using interference. In samples that exhibit strong multiple scattering such as biological tissue, these interference effects manifest themselves as a speckle pattern, and changes to the scattering media cause the speckle pattern to change over time. By capturing a sequence of images of the speckle pattern over time, the degree of correlation between a reference frame and each subsequent frame can be computed, thus providing a measure of how rapidly the scatterers inside the sample are moving. This method of measuring the intensity correlations of speckle over time to analyze the dynamic nature of scattering media was originally developed by Maret, Wolf, Pine, and others in the late 1980s and is known as diffusing wave spectroscopy

(DWS) [8, 10, 17].

The main aim of DWS is to relate the decorrelation of the scattering media due to the movement of the scatterers to the decay of the autocorrelation of the measured electric field. As derived by Maret and Wolf [17], the electric field autocorrelation in the case of multiple scattering and Brownian motion particle diffusion can be written as

$$g_1(\tau) = \int_0^\infty P(s) \exp \left[\left(-\frac{2\tau}{\tau_0} \right) \frac{s}{l^*} \right] ds, \quad (2.1)$$

where τ is delay time, $\tau_0 = 1/(Dk_0^2)$ is the characteristic decay time, $k_0 = 2\pi/\lambda$ is the wavenumber of the light in the medium, D is the diffusion constant of the scattering particles, l^* is the transport mean free path, s is the path length, and $P(s)$ is the distribution of path lengths in the medium. From this equation, we can see that the field autocorrelation is essentially a weighted sum (weights $P(s)$) of exponential decays at rates set by D , k_0 , l^* , and s . However, by examining different thicknesses of the same sample in the same experimental configuration, D , k_0 , and l^* are essentially fixed. Therefore, we can directly probe the relationship between the thickness and the characteristic decay time by determining the dependence of $P(s)$ on the thickness.

By measuring the ratio of unscattered light to the incident beam intensity, we found the scattering coefficient for the brain slices in our experiment to be $\mu_s = 50/\text{mm}$. This is in good agreement with the values found in literature [18]. Using this fact and the forward-scattering nature of tissue (anisotropy factor of $g \approx 0.9$), we find a reduced scattering coefficient of $\mu'_s \approx 5/\text{mm}$. We note here that in our experiment we assume that absorption is negligible since the mean absorption length is an order of magnitude longer than the transport mean free path ($\mu_a=0.2/\text{mm}$, $\mu'_s=5/\text{mm}$) [10, 18, 19]. If the sample thickness is much greater than the transport mean free path ($L \gg l^*$), then the transport of light can be treated as diffusive. Under this assumption, commonly known as the diffusion approximation, DWS theory predicts via a first cumulant expansion of the electric field autocorrelation function that the decay of the autocorrelation function should be proportional to $1/L^2$, where L is the sample thickness [8]. However, when the sample thickness is thin enough so that it is only several times greater than the transport mean free path, the predictions of the diffusion approximation will break down and the decay of the autocorrelation will be more closely proportional to $1/L$, due to the quasi-ballistic propagation of light [20–23]. Here we note that even if the diffusion approximation is not valid,

the framework of DWS still holds as long as the light is multiply scattered by non-interacting Brownian particles [17]. In practice, this means that the path length distribution $P(s)$ in cases where the diffusion approximation breaks down is difficult to analytically calculate and must be approximated via methods such as Monte-Carlo analysis.

In order to experimentally measure the electric field autocorrelation function, it would be most convenient to directly measure the electric field of the scattered light field. However, due to the limitations of intensity only detectors such as photodiodes and conventional CMOS and CCD cameras, measuring the electric field directly is not experimentally convenient. Fortunately, using intensity only measurements we can calculate an intensity autocorrelation function by comparing data points taken at time t_0 and at a later time $t_0 + \tau$ and relate the calculated intensity autocorrelation function to the electric field autocorrelation function via the Siegert relation [24]. Here, the intensity autocorrelation function is given by

$$g_2(\tau) \equiv \frac{\langle I(t_0) \cdot I(t_0 + \tau) \rangle}{\langle I(t_0) \rangle \langle I(t_0 + \tau) \rangle}, \quad (2.2)$$

where $I(t_0)$ and $I(t_0 + \tau)$ are the captured intensities at times t_0 and $t_0 + \tau$ respectively, and $\langle \cdot \rangle$ indicates an average over all captured data for a given delay time. Then, assuming an ergodic system, the intensity autocorrelation function can be related to the field autocorrelation function through the Siegert relation:

$$g_2(\tau) = 1 + \beta |g_1(\tau)|^2. \quad (2.3)$$

Here, $g_2(\tau)$ is the intensity autocorrelation function, $g_1(\tau)$ is the field autocorrelation function, and β is an experimental factor between 0 and 1 determined by the collection optics and capture parameters. In our experiment, β is determined to be $\sim 0.7 - 0.8$ by using the value $\beta = g_2(0) - 1$.

Traditionally, the intensity autocorrelation function is calculated by monitoring the intensity fluctuations of a single speckle via a photodiode and relating the intensity autocorrelation to the field autocorrelation function using ergodicity. However, with the recent advances in high-speed camera technology and data storage and transfer speed capabilities, a more powerful experimental scheme is available. In multi-speckle diffusing wave spectroscopy, the photodiode is replaced by a high speed

array sensor which samples many speckles in parallel at the same time [11]. This relaxes the requirements for temporal ergodicity of the sample, since many speckles are measured in parallel, and enhances the statistical strength of the method to analyze systems with both fast and slow dynamics. In this framework, each measurement is a 2D image, the multiplication in Eq. 2.2 is computed element-wise, and the temporal averages are replaced by pixel-wise averages of the stationary 2D captured frames. Using this procedure, we can capture a time series of speckle pattern images generated by the scattering media and compute the field autocorrelation function ($g_1(\tau)$) using the intensity autocorrelation function ($g_2(\tau)$) and the Siegert relation (Eq. 2.3), thereby characterizing the dynamic nature of the sample.

2.4 Experimental setup for measuring decorrelation in acute brain slices

Fig. 2.1 shows a diagram of the experimental setup used to capture the sequence of speckle patterns. A diode-pumped solid state laser ($\lambda = 532$ nm) illuminates the bottom surface of the sample rat brain slice with a beam diameter of approximately 500 microns. The brain slice is gently fixed with a slice anchor (Warner Instruments, SHD-22L/15) at room temperature in a homemade bath containing PBS to keep the sample hydrated and at a constant temperature. The speckle patterns were captured using a microscope objective focused on the top surface of the brain tissue (Olympus, 20X LCAch N PH) and imaged to a sCMOS camera (PCO-TECH, pco.edge 5.5) at a frame rate of 100 frames per second and exposure time of 1 ms. To improve the contrast of the captured speckle images a linear polarizer was placed in the infinity space region of the microscope and an iris was placed directly behind the exit pupil of the objective to control the speckle size on the detector. The iris was set such that the speckle size on the camera was $\sim 3 \times 3$ pixels to ensure adequate sampling [11]. In order to sample a large number of speckles for statistical stability, a 200×200 pixel region of interest in the center of the frame was selected (~ 4400 speckles). The entire setup was firmly mounted on a vibration isolating optical table to ensure stability and confirmed using a static scattering sample.

Four brain tissue thicknesses of 1, 1.5, 2, and 3 mm from a 3 month old Long-Evans rat were sliced using a vibratome (Leica, VT1200) to ensure accurate thickness. All animal handling procedures were conducted in compliance with the Institutional Animal Care and Use Committee (IACUC) at the California Institute of Technology. Then, the brain tissue slices were mounted in the tissue holder, and speckle patterns were captured from ~ 12 different positions in the tissue samples. The data was captured as quickly as possible within a period of several hours following acquisition

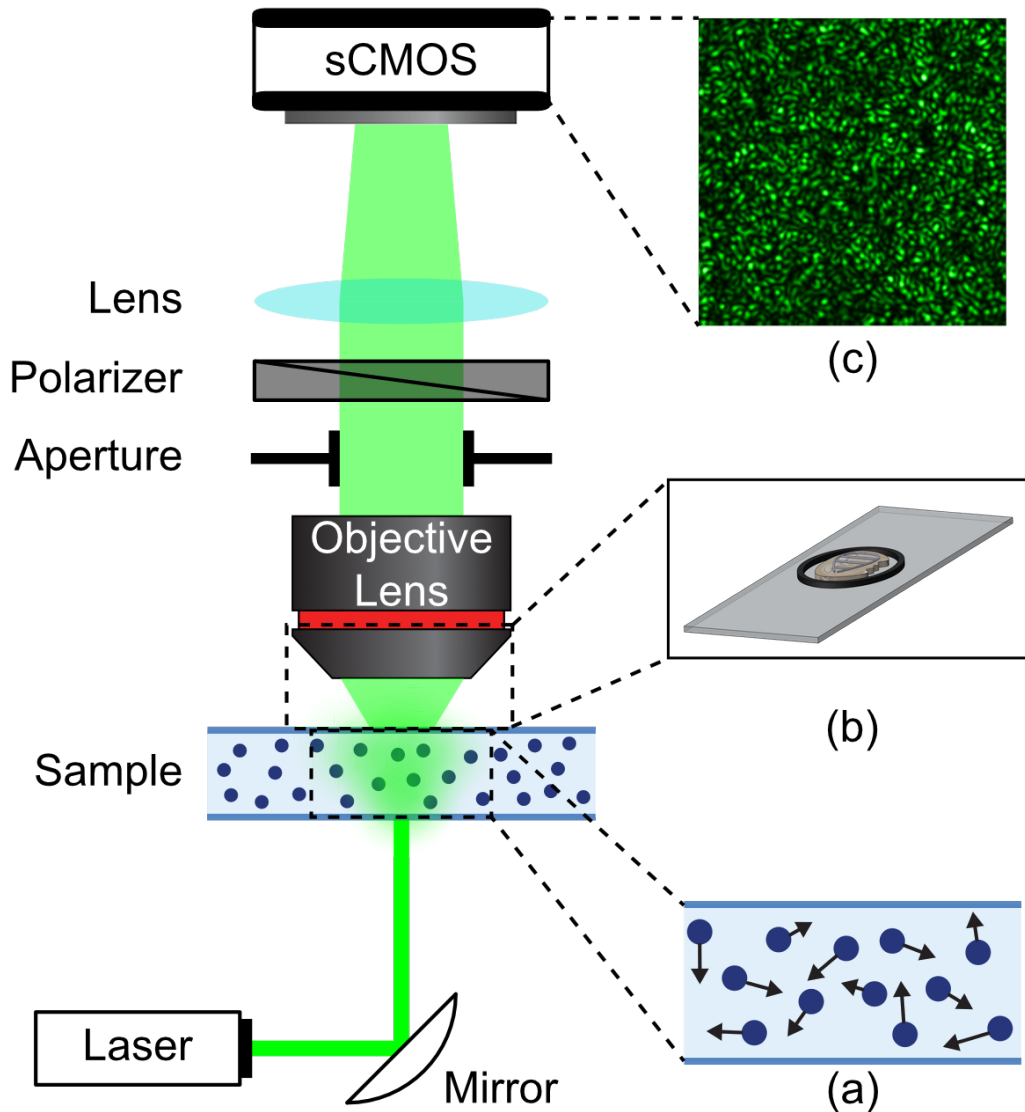


Figure 2.1: **Experimental setup used to capture the speckle patterns.** (a) The scatterers inside the tissue cause the collimated light to form a diffusive speckle pattern which changes over time due to the random Brownian motion of the scatterers within the tissue. (b) Diagram illustrating how the sample is mounted. (c) The speckle pattern is then imaged on the camera, and a sequence of images captured.

of the slices to ensure maximum sample freshness.

2.5 Multispeckle decorrelation analysis procedure

After a time series of speckle images is captured, the image stacks are analyzed in MATLAB according to Eq. 2.2 to compute the intensity autocorrelation function for each thickness. Fig. 2.2 shows an intuitive way to understand the calculation

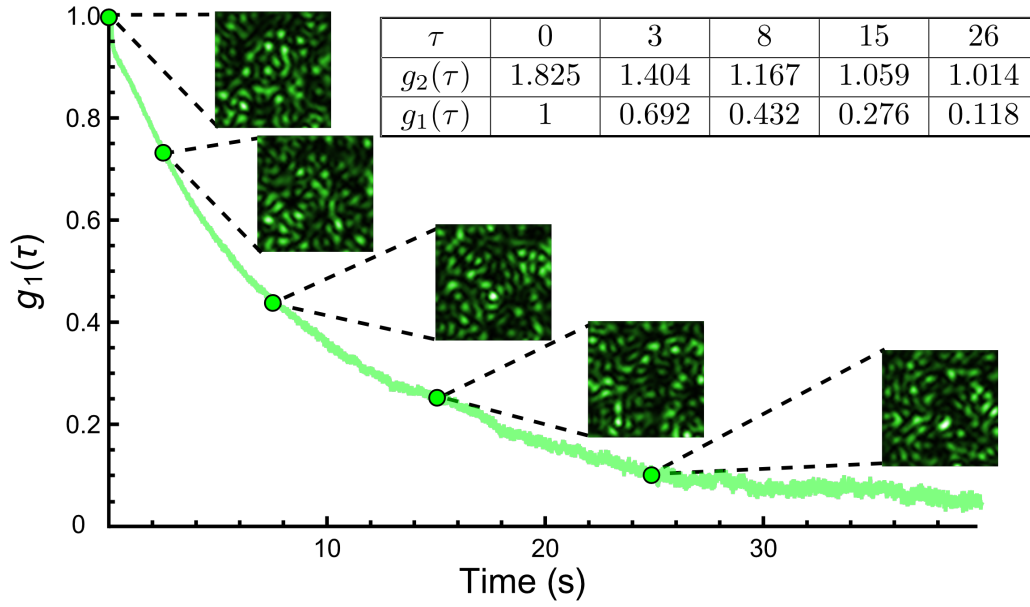


Figure 2.2: $g_2(\tau)$ **decorrelation time calculation.** The calculation procedure for calculating the decorrelation curves is performed by comparing each speckle pattern in the captured sequence with an original reference frame ($\tau = 0$). By pixelwise multiplying the sample and reference speckle image together and dividing by the mean intensities of each image, the degree of correlation at delay time τ can be quantified as $g_2(\tau)$. Then, $g_1(\tau)$ is calculated via Eqn. 2.3.

procedure.

The images in Fig. 2.2 represent the captured speckle patterns at delay times of 0, 3, 8, 15, and 26 seconds respectively. In order to compute the intensity correlation function $g_2(\tau)$, each image in the time series is multiplied entrywise with the first image in the series, and the pixelwise average of this product is divided by the product of the pixelwise averages of individual frames. Then, the Siegert relation is used to calculate the field autocorrelation function where β is taken as $g_2(0)$ to normalize $g_1(\tau)$.

2.6 Multispeckle decorrelation time results

In order to analyze the relationship between the decay rate of the decorrelation curves and the thickness of the sample, we fit each individual decorrelation curve to an exponential decay function given by

$$a * \exp\left(-\frac{t}{t_d}\right) + (1 - a), \quad (2.4)$$

where a is the amplitude of the decay, the $(1 - a)$ offset is added to account for noise factors that cause the decorrelation function not to drop to zero as $t \rightarrow \infty$, and t_d is the decorrelation time. Here, the decorrelation time t_d is inversely related to the first cumulant, providing a measure of the average decay rate of the distribution [25]. Therefore, by fitting the decorrelation curves in this way and calculating the decorrelation time, we can provide a figure of merit for the decay of the autocorrelation function and the movement of the scatterers in the tissue.

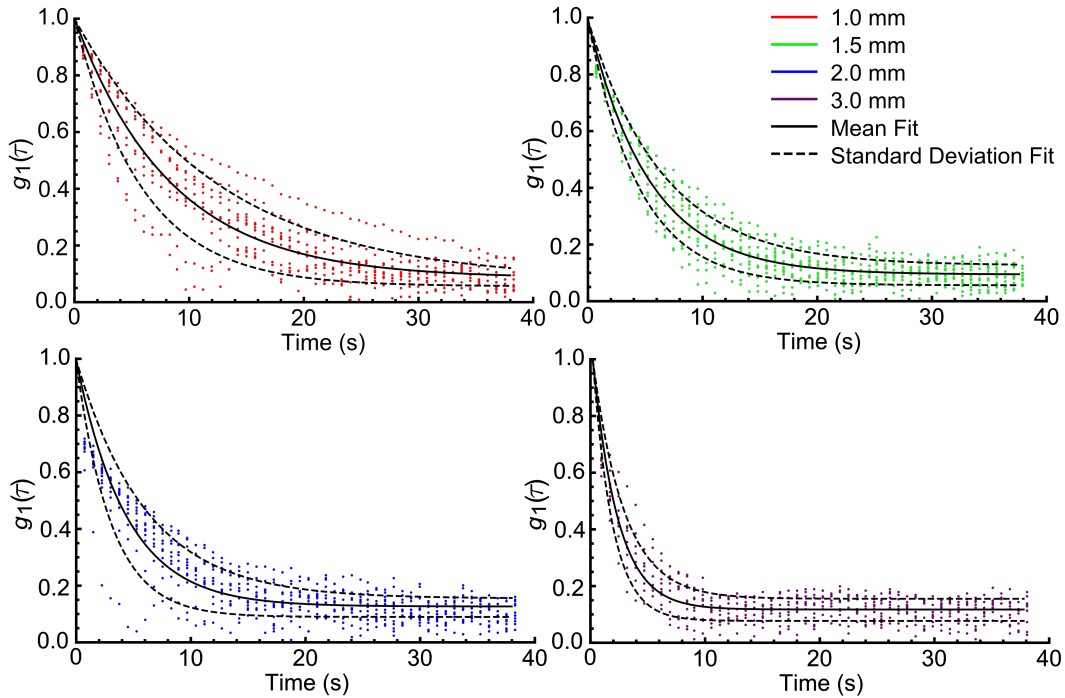


Figure 2.3: Decorrelation curves for 1.0, 1.5, 2.0, and 3.0 mm thick brain slices. Data points shown at intervals of 0.75 seconds. 12, 13, 12, and 10 data sets are presented for the 1.0, 1.5, 2.0, and 3.0 mm thicknesses respectively. The center of the three fitted curves show the sample mean, and the two outer curves show the sample standard deviation bounds.

Fig. 2.3 shows the decorrelation curves for the 1.0, 1.5, 2.0, and 3.0 mm rat brain tissue slices. Each plot shows the fitted sample mean curve with dashed fitted curves above and below indicating the sample standard deviation of the curves. As the tissue sample thickness increases, the decay rate of the decorrelation curves increase, causing the correlation to drop at an increasing rate.

Figure 2.4 shows the decorrelation times of each trial with respect to the tissue thickness. This decorrelation time indicates the time it takes for the amplitude (a) of

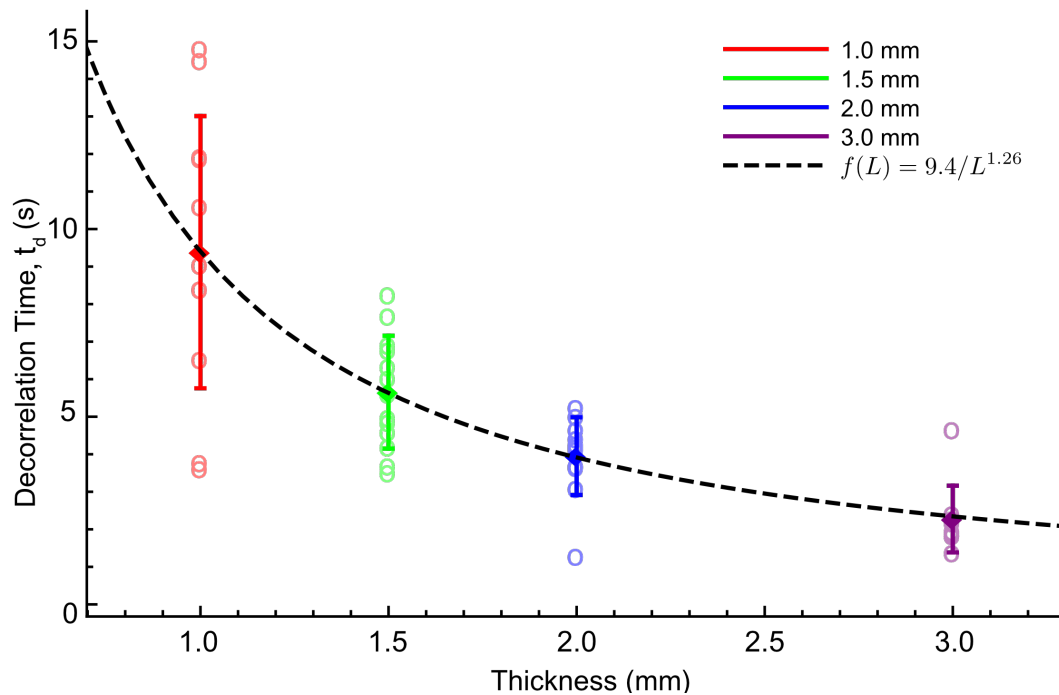


Figure 2.4: **The decorrelation times of the individual trials plotted with respect to the tissue thickness.** The mean decorrelation curve is indicated by the solid line with sample standard deviation bounds illustrated by the dashed lines above and below.

the calculated electric field autocorrelation function to decay to a/e . The measured data shows an average decorrelation time of 9.38, 5.65, 3.95, and 2.27 seconds with standard deviations of 3.63, 1.50, 1.03, and 0.89 seconds for the 1.0, 1.5, 2.0, and 3.0 mm thicknesses respectively. To analyze the trend of the decorrelation time vs tissue thickness, we fit the decorrelation time data with a model related to the inverse of a power of the tissue thickness L , $f(L) = a/L^b$. This yields fitted values of $a = 9.40$ and $b = 1.26$. As we expected, we see that the relationship between the decorrelation time and tissue thickness falls between a $1/L$ and $1/L^2$ description.

There are several reasons why the relationship between decorrelation time and thickness is not purely described by a $1/L$ or $1/L^2$ model. The first reason is due to the breakdown of the diffusion approximation. As noted by several authors in the DWS community, the assumption that light can be treated as diffusive begins to breakdown in the regime where the thickness of the scattering medium is of the same order of magnitude as the transport mean free path ($L < 10 \times l^*$) [20–23]. In fact, when the scattering medium is only a few times thicker than the transport

mean free path, the actual scattering path length distribution $P(s)$ is skewed toward shorter path lengths than predicted by photon-diffusion approximation [22]. This is due to the fact that while the diffusion approximation suggests that the path lengths increase proportional to the square of the thickness of the scattering medium, the scattering path length of the quasi-ballistic component linearly scales with the sample thickness, resulting in a $1/L$ -scaling of the decorrelation time [21]. As mentioned earlier, the transport mean free path in the gray matter of rat brain used in this experiment is ~ 0.2 mm. Thus, in the thickness range from 1 mm to 3 mm, we expect to observe the transition in scaling relation between a $1/L$ model towards a $1/L^2$ model rather than the exact $1/L^2$ -scaling predicted by the diffusion approximation. In addition, while the order of magnitude difference between the mean absorption length and mean scattering length decreases the effect of absorption, incorporating the effects of absorption also shift the characteristic decay times toward a $1/L$ model even in the diffusive regime [10]. This discussion is continued in Section 2.7, where we perform Monte Carlo simulations to analyze the effect of sample thinness (non-diffusive regime) and absorption.

While our experiment was designed to reduce the influence of potential sources of experimental error, the unavoidable heterogeneity of the sample leads to spatially varying scattering properties, therefore impacting the decay characteristics. These effects are especially pronounced in the thin slices (1.0 and 1.5 mm), where the transport mean free path is especially small compared to the thickness. This means that even small changes in the transport mean free path will have significant impact on the path length distribution ($P(s)$) and ultimately on the decay characteristic of the tissue.

2.7 Decorrelation time and the influence of absorption: Monte Carlo simulation results

To further investigate the sources for the deviation from the $1/L^2$ prediction of the diffusion approximation, we conducted Monte Carlo simulation of the photon transport through the tissue to evaluate the path length distribution $P(s)$ of the photons travelling through the sample. Modelling the sample as a semi-infinite slab medium with the optical properties $\mu_s = 5/\text{mm}$, $g = 0.9$, and $\mu_a = 0.2/\text{mm}$, we simulated the path length distributions for the 1, 1.5, 2, and 3 mm thicknesses used in our experiment. To construct the path length distributions, we built a custom single-layer, time-resolved Monte Carlo simulation based on the standard Monte Carlo simulation package developed by L.V. Wang, S.L. Jacques and others [26],

recording the path length of each photon which passed through the sample and was collected within the 0.2 NA and $\sim 0.2 \text{ mm}^2$ field of view of the objective used. The results of the Monte Carlo simulation are shown below in Fig. 2.5.

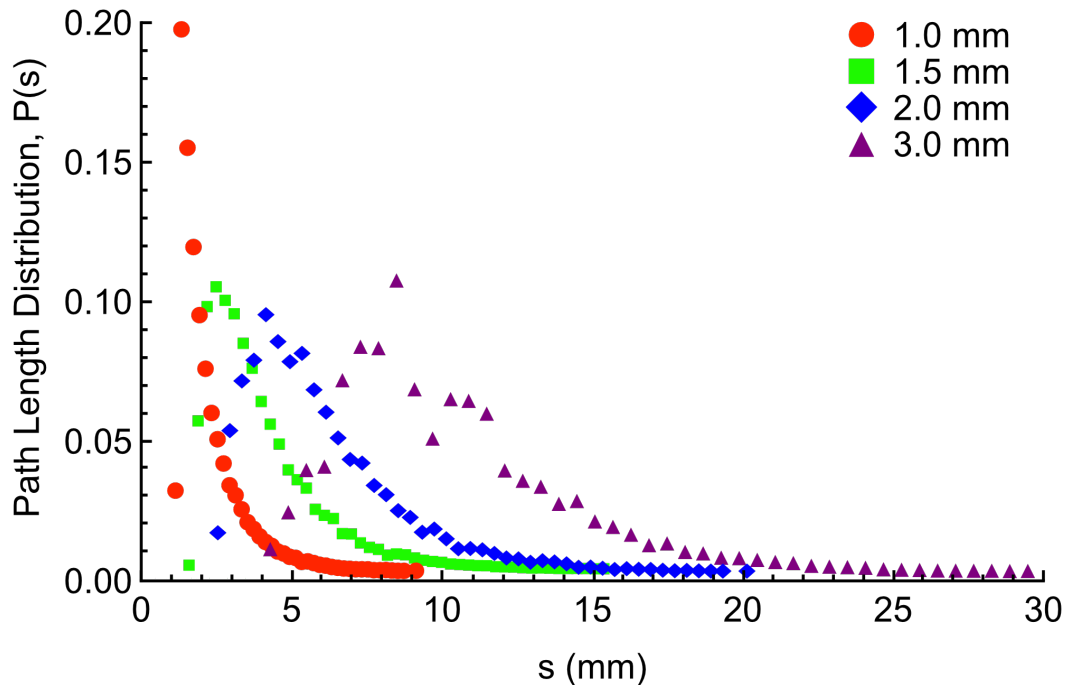


Figure 2.5: **Results of the Monte Carlo simulation of 1×10^6 photons with tissue properties $\mu_s = 5/\text{mm}$, $\mu_a = 0.2/\text{mm}$, and $g = 0.9$.** The plot shows the path length distribution $P(s)$ vs path length s for 1.0, 1.5, 2.0, and 3.0 mm thick samples. As the tissue thickness increases the mean path length increases and the distribution broadens.

As the thicknesses of the sample increases, we observe a growing average path length as well as a broadening of the path length distribution. For the 1.0, 1.5, 2.0, and 3.0 mm slices, the average path lengths are 2.1, 3.9, 5.8, 10.2 mm respectively. Since the first cumulant expansion exponential fits used to determine the decorrelation times are proportional to the inverse of the mean path length, we can analyze the relationship between the inverse of the mean path length and thickness to get a better understanding of the relationship between decorrelation time and thickness from the simulation results. Fig. 2.6 shows the relationship between the inverse of the mean path length and tissue thickness both in the cases where absorption is present and when it is not.

From the simulated data points and corresponding fits in Fig. 2.6, we can understand the influence of absorption on the measured results. Plotting the inverse of the mean

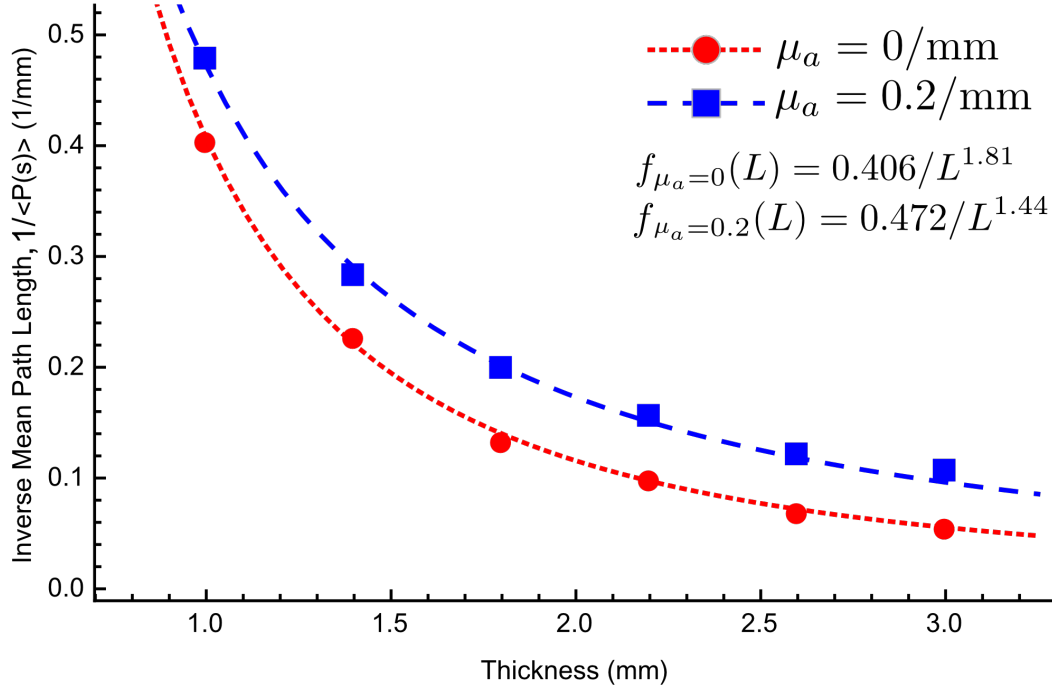


Figure 2.6: **Inverse mean path length $\langle P(s) \rangle$ vs sample thickness from 1-3 mm.** The fitted curves (dashed lines) show the corresponding fits of a/L^b . Here we can clearly see that the effect of absorption both decreases the mean path length and slows the decay from being proportional to $1/L^{1.81}$ to $1/L^{1.44}$.

path lengths with respect to tissue thickness and fitting with a/L^b where a and b are fitting parameters and L is the tissue thickness, reveals that the effect of absorption at small thicknesses is to shift the trend of the decorrelation curve from a $1/L^2$ relationship toward a $1/L$ trend. For the tissues greater than 2.0 mm, we see that the absorption plays a role by terminating the long scattering path lengths, thereby reducing the mean scattering path length. These results suggest that the absorption of the tissue, while much weaker than the effects of scattering, still has a marked impact on the trend of decorrelation time vs thicknesses, reducing the strength of the $1/L^x$ trend.

2.8 Conclusion

In this chapter, we have experimentally probed the relationship between the decorrelation time and the thickness of rat brain tissue using multispeckle diffusing wave spectroscopy. As new optical tools are developed to focus light deep into brain tissue for imaging or selective excitation of neuronal populations, these results will serve as a useful guide in determining how fast these systems must be to respond to

the dynamic nature of tissue in the absence of blood.

We note that in general, the movement of blood and surrounding tissues causes much faster decorrelation and is the ultimate challenge to overcome in *in vivo* applications. However, the results of this study are directly applicable to the selective excitation of neurons in acute brain slices via optogenetics using deep-tissue light focusing methods and also to *in vivo* experiments where blood flow is suppressed via immobilization techniques [7].

Recently several fast wavefront shaping have been demonstrated with response speeds on the order of several milliseconds [14, 15]. Based on the results from this study, we expect that these wavefront shaping techniques will be able to successfully focus light through brain tissue thicker than 10 mm as long as certain practical SNR requirements are met. This capability may enable entire acute brain sections to be optogenetically excited using these techniques. In future studies, we hope to investigate further how this information can enhance the development of novel optical systems to overcome the dynamic nature of biological tissue and enable *in vivo*, deep-tissue imaging.

Funding. GIST-Caltech (CG2012); National Institute of Neurological Disorders and Stroke (NINDS) (1U01NS090577-01); National Institutes of Health (NIH) (1DP2OD007307-01); National Institute of Biomedical Imaging and Bioengineering (1F31EB021153-01); Donna and Benjamin M. Rosen Bioengineering Center.

Acknowledgments. J.B. acknowledges support from an NIH NRSA Predoctoral Fellowship and the Donna and Benjamin M. Rosen Bioengineering Center. The authors would also like to thank Dr. Cheng Xiao for his help in preparing the brain tissue slices.

References

- [1] J. W. Goodman, *Speckle phenomena in optics: theory and applications*. Roberts and Company Publishers, 2007.
- [2] A. P. Mosk, A. Lagendijk, G. Leroose, and M. Fink, “Controlling waves in space and time for imaging and focusing in complex media,” *Nature Photonics*, vol. 6, no. 5, pp. 283–292, 2012.
- [3] I. M. Vellekoop and A. Mosk, “Focusing coherent light through opaque strongly scattering media,” *Optics Letters*, vol. 32, no. 16, pp. 2309–2311, 2007.

- [4] R. Horstmeyer, H. Ruan, and C. Yang, “Guidestar-assisted wavefront-shaping methods for focusing light into biological tissue,” *Nature Photonics*, vol. 9, no. 9, p. 563, 2015.
- [5] X. Xu, H. Liu, and L. V. Wang, “Time-reversed ultrasonically encoded optical focusing into scattering media,” *Nature Photonics*, vol. 5, no. 3, pp. 154–157, 2011.
- [6] Y. M. Wang, B. Judkewitz, C. A. DiMarzio, and C. Yang, “Deep-tissue focal fluorescence imaging with digitally time-reversed ultrasound-encoded light,” *Nature Communications*, vol. 3, p. 928, 2012.
- [7] M. Jang, H. Ruan, I. M. Vellekoop, B. Judkewitz, E. Chung, and C. Yang, “Relation between speckle decorrelation and optical phase conjugation (OPC)-based turbidity suppression through dynamic scattering media: A study on in vivo mouse skin,” *Biomedical Optics Express*, vol. 6, no. 1, pp. 72–85, 2015.
- [8] D. Pine, D. Weitz, P. Chaikin, and E. Herbolzheimer, “Diffusing wave spectroscopy,” *Physical Review Letters*, vol. 60, no. 12, p. 1134, 1988.
- [9] F. MacKintosh and S. John, “Diffusing-wave spectroscopy and multiple scattering of light in correlated random media,” *Physical Review B*, vol. 40, no. 4, p. 2383, 1989.
- [10] D. Pine, D. Weitz, J. Zhu, and E. Herbolzheimer, “Diffusing-wave spectroscopy: Dynamic light scattering in the multiple scattering limit,” *Journal de Physique*, vol. 51, no. 18, pp. 2101–2127, 1990.
- [11] V. Viasnoff, F. Lequeux, and D. Pine, “Multispeckle diffusing-wave spectroscopy: A tool to study slow relaxation and time-dependent dynamics,” *Review of Scientific Instruments*, vol. 73, no. 6, pp. 2336–2344, 2002.
- [12] D. Weitz, J. Zhu, D. Durian, and D. Pine, “Principles and applications of diffusing-wave spectroscopy,” in *Structure and Dynamics of Strongly Interacting Colloids and Supramolecular Aggregates in Solution*, Springer, 1992, pp. 731–748.
- [13] K. Deisseroth, “Optogenetics,” *Nature Methods*, vol. 8, no. 1, pp. 26–29, 2011.
- [14] D. Wang, E. H. Zhou, J. Brake, H. Ruan, M. Jang, and C. Yang, “Focusing through dynamic tissue with millisecond digital optical phase conjugation,” *Optica*, vol. 2, no. 8, pp. 728–735, 2015.
- [15] Y. Liu, P. Lai, C. Ma, X. Xu, A. A. Grabar, and L. V. Wang, “Optical focusing deep inside dynamic scattering media with near-infrared time-reversed ultrasonically encoded (TRUE) light,” *Nature Communications*, vol. 6, 2015.
- [16] D. B. Conkey, A. M. Caravaca-Aguirre, and R. Piestun, “High-speed scattering medium characterization with application to focusing light through turbid media,” *Optics Express*, vol. 20, no. 2, pp. 1733–1740, 2012.

- [17] G. Maret and P. Wolf, “Multiple light scattering from disordered media. the effect of brownian motion of scatterers,” *Zeitschrift für Physik B Condensed Matter*, vol. 65, no. 4, pp. 409–413, 1987.
- [18] M. Azimipour, R. Baumgartner, Y. Liu, S. L. Jacques, K. Eliceiri, and R. Pashaie, “Extraction of optical properties and prediction of light distribution in rat brain tissue,” *Journal of Biomedical Optics*, vol. 19, no. 7, pp. 075 001–075 001, 2014.
- [19] M. Mesradi, A. Genoux, V. Cuplov, D. Abi-Haidar, S. Jan, I. Buvat, and F. Pain, “Experimental and analytical comparative study of optical coefficient of fresh and frozen rat tissues,” *Journal of Biomedical Optics*, vol. 18, no. 11, p. 117 010, 2013.
- [20] D. Durian, “Accuracy of diffusing-wave spectroscopy theories,” *Physical Review E*, vol. 51, no. 4, p. 3350, 1995.
- [21] I. Freund, M. Kaveh, and M. Rosenbluh, “Dynamic multiple scattering: Ballistic photons and the breakdown of the photon-diffusion approximation,” *Physical Review Letters*, vol. 60, no. 12, p. 1130, 1988.
- [22] K. Yoo, F. Liu, and R. Alfano, “When does the diffusion approximation fail to describe photon transport in random media?” *Physical Review Letters*, vol. 64, no. 22, p. 2647, 1990.
- [23] P.-A. Lemieux, M. Vera, and D. Durian, “Diffusing-light spectroscopies beyond the diffusion limit: The role of ballistic transport and anisotropic scattering,” *Physical Review E*, vol. 57, no. 4, p. 4498, 1998.
- [24] P.-A. Lemieux and D. J. Durian, “Investigating non-gaussian scattering processes by using nth-order intensity correlation functions,” *J. Opt. Soc. Am. A*, vol. 16, no. 7, pp. 1651–1664, Jul. 1999. DOI: 10.1364/JOSAA.16.001651.
- [25] B. J. Frisken, “Revisiting the method of cumulants for the analysis of dynamic light-scattering data,” *Applied Optics*, vol. 40, no. 24, pp. 4087–4091, 2001.
- [26] L. Wang, S. L. Jacques, and L. Zheng, “MCML—monte carlo modeling of light transport in multi-layered tissues,” *Computer Methods and Programs in Biomedicine*, vol. 47, no. 2, pp. 131–146, 1995.

*Chapter 3***DECORRELATION IN THE *IN VIVO* MOUSE BRAIN DUE TO BLOOD FLOW**

*This chapter is adapted from the manuscript M. M. Qureshi[†], J. Brake[†], H.-J. Jeon, H. Ruan, Y. Liu, A. M. Safi, T. J. Eom, C. Yang, and E. Chung, “In vivo study of optical speckle decorrelation time across depths in the mouse brain,” *Biomedical Optics Express*, 8(11), pp. 4855–4864, 2017. DOI: 10.1364/BOE.8.004855*

3.1 Abstract

The strong optical scattering of biological tissue confounds our ability to focus light deeply into the brain beyond depths of a few hundred microns. This challenge can be potentially overcome by exploiting wavefront shaping techniques, which allow light to be focused through or inside scattering media. However, these techniques require the scattering medium to be static, as changes in the arrangement of the scatterers between the wavefront recording and playback steps reduce the fidelity of the focus that is formed. Furthermore, as the thickness of the scattering medium increases, the influence of the dynamic nature becomes more severe due to the growing number of scattering events experienced by each photon. In this paper, by examining the scattering dynamics in the mouse brain *in vivo* via multispeckle diffusing wave spectroscopy (MSDWS) using a custom fiber probe that simulates a point-like source within the brain, we investigate the relationship between this decorrelation time and the depth of the point-like light source inside the living mouse brain at depths up to 3.2 mm.

3.2 Wavefront shaping and decorrelation in living tissue

The use of light in biomedicine for imaging and therapeutic applications is powerful due to the ability to image and deliver light with high spatial resolution in a noninvasive and nondestructive manner. The wide array of light-matter interactions such as scattering, absorption, fluorescence, and Raman scattering offer many different contrast mechanisms that can be used to interrogate and understand biological processes [1]. However, the strong scattering nature of biological tissue in the optical regime limits conventional high-resolution imaging and light focusing techniques to superficial layers of several hundred microns or less [2].

For many years in optics, the scattering of light was assumed to be the fundamental limit for high-resolution light delivery deep into turbid media. However, recent work in the field of wavefront shaping has shown that light can be focused at depths beyond several transport mean free paths by appropriately shaping the input light field. This opens a new regime for optical focusing between the transport mean free path and the absorption limit which is typically two orders of magnitude larger [3, 4]. Focusing light to a targeted location inside or through scattering media with the aid of wavefront shaping works by finding an appropriate input light field pattern such that the light can constructively interfere at the desired locations. Since this demonstration, wavefront shaping methods have been an active area of research [5–8], and several approaches have been developed, including those based on feedback [9], phase conjugation [10], and transmission matrix measurement [11].

The initial wavefront shaping demonstrations used static scattering media such as white paint layers, opal diffusers, or fixed tissue. In these static samples, the scatterers within are often stable for periods of time ranging from minutes to hours, and therefore, the optimal wavefront for forming constructive interference also remains constant over these time scales. However, many of the exciting applications for wavefront shaping are in living tissues where the optimal wavefront to focus light to a desired location varies with time due to Brownian motion and physiological motion such as breathing, heartbeat, and blood flow. While previous studies have demonstrated the ability to focus light through living tissue such as the mouse dorsal skin flap [12] or ear [13], the scattering of light by the vasculature in the brain significantly decreases the decorrelation time and prevents these methods from being translated directly for use in brain tissue *in vivo*.

Wavefront shaping systems are limited by both their wavefront measurement and playback schemes. Since the decorrelation time impacts system performance regardless of whether a feedback [14], transmission matrix [11, 15], or optical phase conjugation (OPC) [10, 12, 16, 17] based wavefront measurement scheme is used, it is a widely useful parameter for wavefront shaping systems. The decorrelation time is also helpful for evaluating wavefront playback schemes. These approaches have response times ranging from several tens of microseconds to several tens of milliseconds depending on whether nematic liquid crystal [12, 18], ferroelectric liquid crystal [17], or microelectromechanical systems based spatial light modulator (SLM) technologies are used [16, 19, 20]. Put together, the combined wavefront measurement and playback operation must take place within the decorrelation time

to successfully focus light using wavefront shaping. This makes the synergistic combination of an appropriate measurement and playback scheme critical. Understanding the decorrelation time and its relationship to the tissue thickness is an important, widely applicable parameter of interest for designing new wavefront shaping systems to focus light beyond several transport mean free paths deep in tissue, especially for systems geared toward *in vivo* applications.

The time scale at which the wavefront varies can be measured by observing the speed at which it loses correlation with a previous copy of itself over time. This is typically accomplished by computing a measure of the correlation between the wavefronts or speckle intensity patterns. Then, by fitting the correlation function, a figure of merit called the decorrelation time (or speckle correlation time) can be determined. The decorrelation time is defined as the time it takes for the correlation between the initial wavefront and the subsequently captured wavefronts to drop below a specific value. Previous studies [12, 13, 17, 21] have established the direct relationship between the speckle decorrelation time and the fidelity of the wavefront reconstruction for delivering light into a focus, and also characterized the speckle decorrelation times associated with living ear tissue both with and without the contribution of blood flow. More recently, the relationship between decorrelation time and tissue thickness was studied in acute rat brain slices [22]. However, up until now, the decorrelation time in the *in vivo* rodent brain and its relationship to the thickness of the tissue through which the light passes has not been directly measured or quantified.

In this study, we experimentally measure and report the relationship between the speckle decorrelation time and the depth of a point-like source inside the *in vivo* mouse brain. The results of this study provide an important order of magnitude measurement of the decorrelation time at a depth up to several millimeters below the surface of the brain. The experimental results included in this paper will help inform the development of wavefront shaping systems for *in vivo* applications such as deep tissue light focusing, imaging, and therapy and provide information for applying other optical techniques using speckle such as laser speckle contrast imaging (LSCI) [23] and ultrasound modulated optical tomography (UOT) [24] in the brain *in vivo*.

3.3 Multispeckle decorrelation theory and analysis in living tissue

To measure the decorrelation time, we used the framework of diffusing wave spectroscopy (DWS) [25–27]. DWS is a technique that uses measured fluctuations in the

scattered optical field passing through a dynamic scattering medium to determine the characteristic time scale associated with the movement of the scatterers within the medium. The key quantity of interest in DWS is the temporal autocorrelation function of the electric field, $g_1(\tau)$, which can be directly derived from the interfering contributions of photons of varying path lengths. Due to the multiple scattering process, the path length fluctuations reflect the movement of the scatterers. These fluctuations impact the decay time of the autocorrelation function, allowing the decay time of the autocorrelation function to be used to measure the movement of the scatterers inside the medium.

The field autocorrelation function $g_1(\tau)$ is difficult to measure directly due to the limitation of intensity-only detectors such as photodiodes and conventional CMOS and CCD cameras. Therefore, the intensity autocorrelation function $g_2(\tau)$ is typically recorded instead of $g_1(\tau)$ since it can be directly measured with intensity-only detectors. Then, using the appropriate version of the Siegert relation, the intensity autocorrelation function can be used to relate the intensity and field autocorrelation functions [25, 26, 28, 29]. While the exact relationship between the dynamics of the scatterers and $g_2(\tau)$ must be retrieved by using the appropriate Siegert relation, the decay time of $g_2(\tau)$ itself is a helpful metric to establish the decay time of the measured optical wavefront.

In the first experimental demonstrations, DWS was implemented by measuring the temporal evolution of a single speckle grain to compute the autocorrelation function [25, 26]. This required long measurement times and that the sample be ergodic [30]. One method to address these challenges is to measure many speckles in parallel using an array detector such as a digital camera in lieu of a single speckle on a photodiode. This configuration, called multispeckle diffusing wave spectroscopy (MSDWS), enables many speckles to be measured in parallel which reduces the necessary measurement time, and thus the requirement for ergodicity since each group of pixels corresponding to a single speckle can be considered a separate temporal measurement [31]. While the time scales that can be probed are slower than those accessible with photon counting devices such as photo multiplier tubes or avalanche photodiodes, state of the art sCMOS cameras can achieve sub-millisecond resolution, and therefore are advantageous when the autocorrelation function decays on the order of a few milliseconds.

To calculate the autocorrelation function, a series of intensity measurements are made. In the case of MSDWS, these are camera speckle images. Then, using

this temporal series of images, the autocorrelation function $g_2(\tau)$ is calculated by computing the correlation function between the sample frame at delay time τ and the initial frame in the series taken at time t_0 . This calculation is described by

$$g_2(\tau) = \frac{\langle I(t_0) \cdot I(t_0 + \tau) \rangle}{\langle I(t_0) \rangle \langle I(t_0 + \tau) \rangle} \quad (3.1)$$

where I is the intensity image captured on the sensor, τ is the delay time after the original frame measured at t_0 , and $\langle \dots \rangle$ represents an average over the elements of the element-wise multiplication of the frames. For a fully-developed speckle pattern with an exponential intensity distribution [32], $g_2(\tau)$ theoretically decays from a value of 2 (completely correlated) to a value of 1 (no correlation). However, partially developed speckle or experimental noise (e.g. due to blurring of the speckle pattern within the exposure time) means that in practice $g_2(\tau)$ typically decays from a value less than 2 to a steady state value greater than 1. By fitting this curve with an appropriate model based on the experimental configuration, the decorrelation time can be determined.

3.4 Experimental setup for *in-vivo* multispeckle decorrelation measurements of the rat brain

The experimental setup is shown in Fig. 3.1. A Helium-neon (HeNe) laser with a wavelength of $\lambda = 632.8$ nm and an output power of 17 mW (Research Electro-Optics Inc., Colorado, USA) was used to illuminate the brain through a custom optical fiber probe embedded into the brain. A microscope objective lens (RMS4X, NA 0.10, Olympus) focused on the top surface of the brain was used along with a tube lens (180 mm) to image the speckle pattern onto an sCMOS camera (Neo 5.5 sCMOS, Andor Technology Ltd., Belfast, UK). A linear polarizer, placed in the infinity space between the microscope objective and tube lens, helped to improve the contrast of the captured speckle image. Camera frames were captured at the minimum exposure time of 0.103 ms which enabled a frame rate of 9701 fps.

To move the point-like source inside the brain, we used a mechanical micromanipulator (MN-153 Narishige, Japan) configured to move diagonally at a 45° angle with respect to the normal direction as shown in Fig. 3.1. The penetration depth d was calculated using the insertion angle (45 deg) and the translation distance s along the axis of the needle. Since the location of the fiber probe translated along the x -axis as well as along the z -axis as the micro manipulator was advanced, a sub-region (256

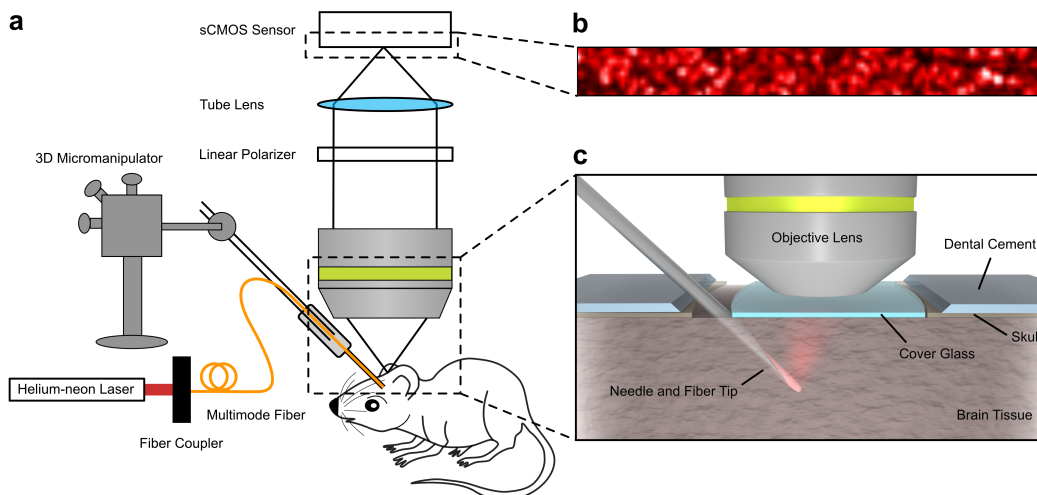


Figure 3.1: **Diagram of the experimental setup.** (a) The experimental setup consisted of a Helium-neon laser coupled to a custom-made fiber probe. The fiber probe was covered with white ZnO paint to simulate a diffuse point-like source in the tissue. (b) The speckle pattern on the surface of the brain was imaged to an sCMOS sensor using a microscope objective and tube lens. A linear polarizer helped to maximize the contrast of the captured speckle pattern, and the iris ensured an adequate speckle size on the sensor. (c) A zoomed view of the mouse brain and fiber tip. The fiber tip was inserted at a 45-degree angle into the mouse brain through a gap between the skull and the cover glass which formed the cranial window. Then, the fiber was advanced from a depth d of 1.1 mm to 3.2 mm below the brain surface, and a series of speckle patterns was recorded at each depth to analyze the decorrelation time.

$\times 12$ pixels, pixel size $6.5 \mu\text{m}$) for each depth, centered at the maximum intensity of the diffuse light profile on the brain surface, was selected out of the full size frame (1200×12 pixels) to allow for consistent sampling of the speckle pattern directly above the fiber tip across depths. We also made sure to avoid large blood vessels near the pial surface of the brain when selecting the regions of interest for analysis as shown in Fig. 3.2(c). The iris size in the optical train was selected so the speckle size on the camera was 2.2×2.2 pixels to satisfy the Nyquist criteria for sampling the speckle. The laser beam was coupled into a $105 \mu\text{m}$ core diameter (with jacket diameter $250 \mu\text{m}$) multimode fiber (Thorlabs FG105LCA) and the other end of fiber tip inserted through a 26-gauge needle (inner diameter = $260 \mu\text{m}$).

To simulate an isotropic point-like source embedded in the tissue, the fiber tip was covered with white spray paint made of Zinc oxide (ZnO) nanoparticles as shown in Fig. 3.2. Figure 3.2(a) shows a photograph of the fiber tip with the ZnO coating

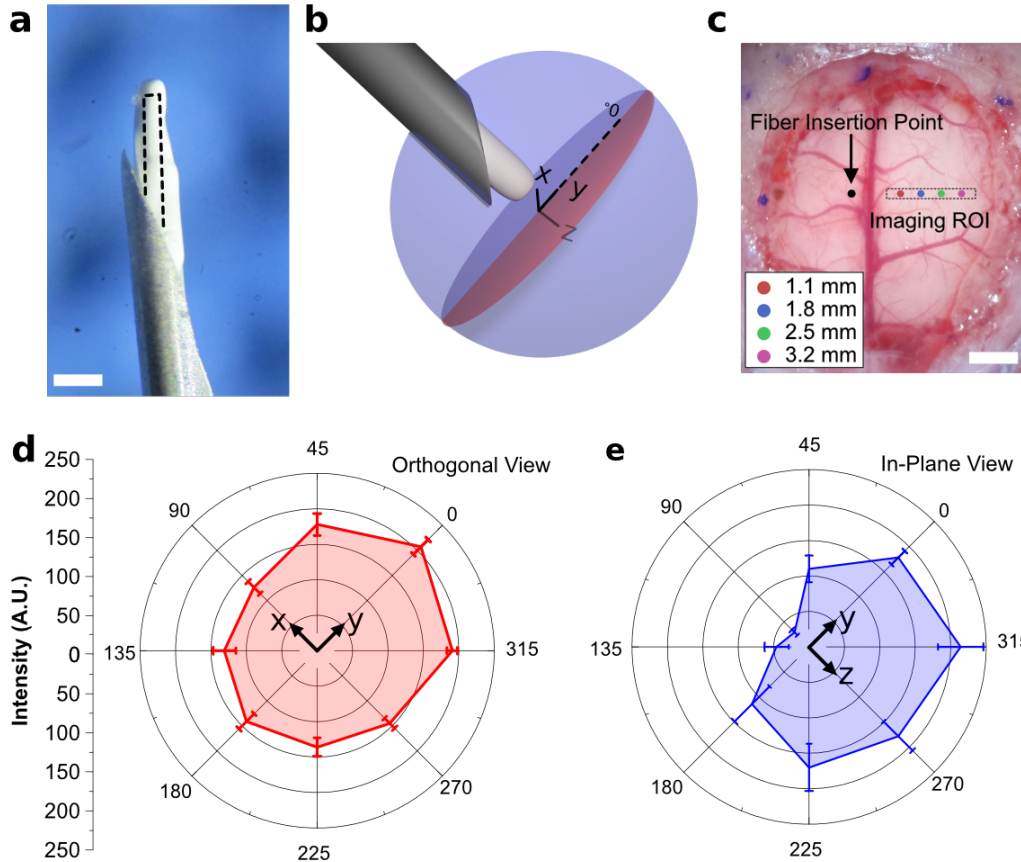


Figure 3.2: **Characterization of diffusing fiber tip light distribution.** (a) The custom fiber tip probe is made of a 105- μm diameter multimode fiber covered with white paint to create a diffuse, point-like source in the brain tissue. (b) To characterize the distribution of light exiting the fiber tip, we measured the light intensity profile in the x-y (red) and y-z (blue) planes. (c-d) The orthogonal (c) and in-plane (d) light intensity distributions. The solid line traces the mean of five measurements, and the error bars indicate the standard deviation of the measurements. Scale bar: 200 μm .

and Fig. 3.2(b) displays a 3D representation of the fiber probe and the two planes used to characterize the light distribution emitted from the fiber tip. Figure 3.2(c) and (d) show polar graphs of the light intensity distributions for the orthogonal (red) and in-plane (blue) perspectives, respectively. The intensity distribution is highly symmetric except for the portion of the in-plane view between 60° and 180° that is occluded by the body of the needle.

After manufacturing the fiber probe, we proceeded to perform *in vivo* experiments to measure the autocorrelation function as a function of the penetration depth of the

fiber probe. In our experiment, all the animal handling followed the guidelines of the Institutional Animal Care and Use Committee (IACUC) at the Gwangju Institute of Science and Technology, Korea. We used three male black mice (C57BL/6, each 12-14 weeks old with body weights between 25-30 grams).

Throughout the experimental protocol, the mice were anesthetized with a Zoetil/Xylazine mixture in saline solution (60/10 mg/kg body weight), and the body temperature was maintained at 37°C.

The craniotomy was performed using a standard procedure (see [33]). The diameter of the drilling site on the mouse skull was ~ 7 mm, and the cover slip placed on the exposed brain was 5 mm in diameter. The difference between the two diameters was used to allow for the fiber probe to be inserted into the brain. The animal was then fixed on the heating pad with a customized angel ring for stability (Customized ring type *in vivo* heating system, Live Cell Instrument, Seoul, Korea) [34].

3.5 *In-vivo* decorrelation measurement results

We chose depths of 1.1, 1.8, 2.5, and 3.2 mm to measure the decorrelation times. These depths span the depth of the cortical and subcortical regions in the mouse brain, an area of interest in neuroscience studies [35, 36]. To analyze the decorrelation times for each thickness, we used a nonlinear least squares optimization routine to fit individual decorrelation curve to a double exponential model given by

$$g_2(t) = a \times \exp\left(-2 \times \frac{t}{b}\right) + c \times \exp\left(-2 \times \frac{t}{d}\right) + (e + 1), \quad (3.2)$$

where a and c are the decay amplitudes, b and d are the characteristic times for each decay term, and e accounts for the curve offset from 1 at steady state. Here the two exponential terms serve to model the slow (e.g. due to tissue motion) and fast (e.g. due to blood flow) decorrelation time components. Then, the overall decorrelation time is determined by finding the time where the curve decay amplitude ($a + c$) decays to $1/e$ of its initial value.

Figure 3.3 shows the decorrelation curves for each depth with the fitted mean curve and a shaded area surrounding it representing the 95% confidence interval. Each curve was computed from an image stack after background subtraction using Eq. 3.1. For each depth, 14 data sets were used from three animals. The value of g_2 does not decay to 1 likely due to blurring of the speckle pattern within the acquisition and

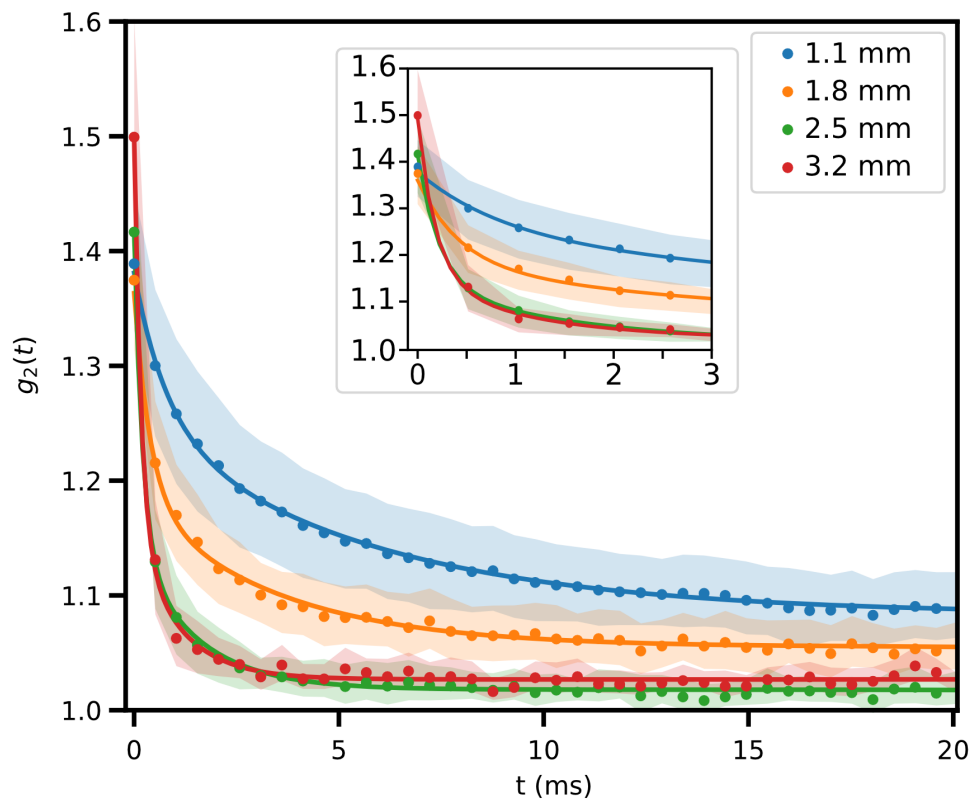


Figure 3.3: **Decorrelation curves for different fiber tip depths.** The decorrelation curves from 1.1 mm, 1.8 mm, 2.5 mm, and 3.2 mm were calculated by penetrating the respective depth into the mouse brain tissue using the fiber probe and capturing a time series of speckle patterns. Then, using the procedure explained above, $g_2(t)$ was calculated and plotted for each thickness. In the plot above, every 5th data point of the mean curve is shown for clarity, and the solid lines indicate the fit of the mean data points. Each thickness consists of a total of 14 traces across three mice. Shaded areas indicate the 95% confidence intervals for the mean of the data at each time point.

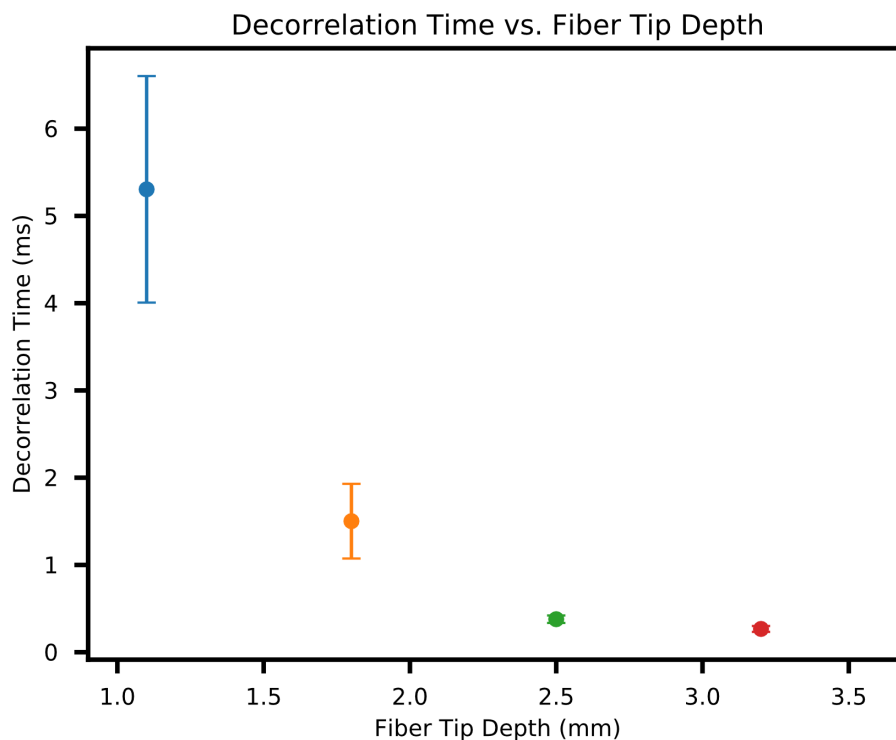


Figure 3.4: **Decorrelation time as a function of fiber tip penetration depth.** As the fiber tip penetrates deeper into the brain tissue, the decorrelation time decreases due to the increasing number of scattering events. The error bars indicate the standard error of the mean of the decorrelation times over the 14 total data sets from $n = 3$ mice at each depth.

contributions from ballistic or quasi-ballistic photons that form a static background speckle pattern, thus preserving correlation even after the multiply scattered portion of the pattern has decorrelated. However, as the penetration depth increases, the probability of unscattered photons continues to decrease, and the g_2 curves decay nearly to 1 with a slight offset likely due to blurring of the speckle. The respective mean decorrelation times for 1.1, 1.8, 2.5, and 3.2 mm depth of point-like source are 5.3, 1.5, 0.37, and 0.26 ms, with standard deviations of 4.8, 1.6, 0.16, 0.13 ms.

Next, we investigated the relationship between the decorrelation time and penetration depth. By collecting the decorrelation time parameter from the individual fitting results, we plotted the mean decorrelation time with the accompanying standard error of the mean as a function of the depth of the point-like light source as shown in Fig. 3.4. As the depth increases, the speckle decorrelation time decreases due

to the increasing number of photon scattering events, dropping below 1 millisecond beyond a penetration depth of 2 millimeters.

3.6 Discussion and Conclusion

In this study, we investigated the speckle decorrelation time associated with living mouse brains. The speckle decorrelation time is a parameter of interest for a variety of optical methods including wavefront shaping, laser speckle contrast imaging (LSCI), and ultrasound modulated optical tomography (UOT). In the context of wavefront shaping, the decorrelation time dictates the speed at which the system needs to operate to successfully focus light in or through a scattering medium and the time window of validity for transmission matrix measurements and subsequent light control. In laser speckle contrast imaging and UOT, the speckle decorrelation time helps to determine the experimental settings best suited for high fidelity analysis of the speckle contrast [37]. We hope the data presented here will be of use for optical engineers and scientists seeking to develop their respective techniques for *in vivo* applications in the brain.

Currently, the maximum depth we can investigate with our measurement setup is limited by the size of the mouse brain and the temporal resolution of our system, which is set by the maximum camera frame rate of our sCMOS camera (9701 frames per second for a frame size of 1200×12 pixels). From our study, we found that the decorrelation time *in vivo* in the mouse brain ranges from several milliseconds at a depth of 1 mm to sub-millisecond at depths greater than 3 mm. This is several orders of magnitude faster than the decorrelation time in *ex vivo* brain tissue of the same thicknesses, due to the significant influence of intracerebral flow (e.g. blood) on the decorrelation [22].

The translation of wavefront shaping systems to practical applications in living tissue is an area of active research. Applying wavefront shaping methods to optical methods for studying the brain is of great interest due to the widespread use of light in the brain both for neural activity monitoring with techniques such as GCaMP imaging [38] or for neuronal modulation with approaches such as optogenetics [39]. By applying wavefront shaping to counteract the effects of scattering in the brain, it would be possible to extend the depth at which these techniques can noninvasively operate. However, the millisecond-order time scales of movement in the brain limits current wavefront shaping methods and necessitates the development of faster techniques.

Based on the decorrelation times measured in the *in vivo* mouse brain, this means that the maximum depth accessible with current wavefront shaping technology (minimum system latency of ~ 3 ms [17]) in the *in vivo* mouse brain is between 1 and 2 mm. Therefore, to develop wavefront shaping methods which are practical and robust for *in vivo* light focusing for applications such as high-resolution deep tissue optical imaging, noninvasive deep tissue optogenetics, and photodynamic therapy at depths several millimeters below the tissue surface, it will be necessary to develop faster wavefront shaping tools. We believe that one promising solution to this problem is the development of an integrated wavefront measurement and shaping device which combines SLM and camera pixels into a single unit [40, 41]. This will allow for wavefront measurement and playback to be achieved on a parallel, per pixel basis, thus enabling sub-millisecond focusing times that will increase the penetration depth of wavefront shaping techniques to several millimeters *in vivo* in the brain. Other strategies to increase the decorrelation time are to move to longer wavelengths in the near infrared regime where scattering is less severe, or to use coherence gating and short pulses to extend the decorrelation time by selecting only minimally scattered photons [42, 43].

In future experiments, we hope to investigate the decorrelation time of the living brain at longer, near-infrared wavelengths (900-1200 nm), since these may be of future interest for wavefront shaping applications. In addition, it would be interesting to compare the decorrelation time in awake, head-fixed mice compared to the decorrelation time measurements from the anesthetized mice used in this study. To analyze deeper penetration depths, we can also modify the system to use a point based detector with a larger bandwidth than the sCMOS camera used in this study in order to record the dynamics of faster decorrelation processes.

In conclusion, we have shown for the first time the decorrelation time in the *in vivo* mouse brain up to 3.2 mm deep inside the mouse brain using a custom point-like fiber probe source. To take full advantage of our developed system, we have introduced a simple craniotomy to embed our point source at the desired angle in a minimally invasive manner to enable stable imaging over the course of the experiment. The results of this study will help to inform the development of future wavefront shaping systems for *in vivo* applications in the brain.

Acknowledgments

This work was supported in part by GIST Research Institute (GRI), and the GIST-Caltech Research Collaboration Project through a grant provided by GIST in 2017. We also acknowledge support from a research grant (NRF-2016R1A2B4015381) and by the Brain Research Program (NRF-2017M3C7A 1044964) of the National Research Foundation (NRF), by KBRI basic research program through Korea Brain Research Institute (17-BR-04) funded by the Ministry of Science, ICT, and Future Planning, and from the National Institutes of Health (NIH) (U01NS090577). J.B. was supported by the National Institute of Biomedical Imaging and Bioengineering (F31EB021153) under a Ruth L. Kirschstein National Research Service Award and by the Donna and Benjamin M. Rosen Bioengineering Center.

References

- [1] J. Mertz, *Introduction to optical microscopy*. Roberts, 2010, vol. 138.
- [2] V. Ntziachristos, “Going deeper than microscopy: The optical imaging frontier in biology,” *Nature Methods*, vol. 7, no. 8, p. 603, 2010.
- [3] L. V. Wang and H.-i. Wu, *Biomedical optics: principles and imaging*. John Wiley & Sons, 2012.
- [4] S. L. Jacques, “Optical properties of biological tissues: A review,” *Physics in Medicine & Biology*, vol. 58, no. 11, R37, 2013.
- [5] A. P. Mosk, A. Lagendijk, G. Leroose, and M. Fink, “Controlling waves in space and time for imaging and focusing in complex media,” *Nature Photonics*, vol. 6, no. 5, pp. 283–292, 2012.
- [6] H. Yu, J. Park, K. Lee, J. Yoon, K. Kim, S. Lee, and Y. Park, “Recent advances in wavefront shaping techniques for biomedical applications,” *Current Applied Physics*, vol. 15, no. 5, pp. 632–641, 2015.
- [7] R. Horstmeyer, H. Ruan, and C. Yang, “Guidestar-assisted wavefront-shaping methods for focusing light into biological tissue,” *Nature Photonics*, vol. 9, no. 9, p. 563, 2015.
- [8] S. Rotter and S. Gigan, “Light fields in complex media: Mesoscopic scattering meets wave control,” *Reviews of Modern Physics*, vol. 89, no. 1, p. 015 005, 2017.
- [9] I. M. Vellekoop, “Feedback-based wavefront shaping,” *Optics Express*, vol. 23, no. 9, pp. 12 189–12 206, 2015.
- [10] Z. Yaqoob, D. Psaltis, M. S. Feld, and C. Yang, “Optical phase conjugation for turbidity suppression in biological samples,” *Nature Photonics*, vol. 2, no. 2, p. 110, 2008.

- [11] S. Popoff, G. Lerosey, R. Carminati, M. Fink, A. Boccarda, and S. Gigan, “Measuring the transmission matrix in optics: An approach to the study and control of light propagation in disordered media,” *Physical Review Letters*, vol. 104, no. 10, p. 100601, 2010.
- [12] M. Jang, H. Ruan, I. M. Vellekoop, B. Judkewitz, E. Chung, and C. Yang, “Relation between speckle decorrelation and optical phase conjugation (OPC)-based turbidity suppression through dynamic scattering media: A study on in vivo mouse skin,” *Biomedical Optics Express*, vol. 6, no. 1, pp. 72–85, 2015.
- [13] Y. Liu, P. Lai, C. Ma, X. Xu, A. A. Grabar, and L. V. Wang, “Optical focusing deep inside dynamic scattering media with near-infrared time-reversed ultrasonically encoded (TRUE) light,” *Nature Communications*, vol. 6, 2015.
- [14] I. M. Vellekoop and A. Mosk, “Phase control algorithms for focusing light through turbid media,” *Optics communications*, vol. 281, no. 11, pp. 3071–3080, 2008.
- [15] Y. Choi, T. D. Yang, C. Fang-Yen, P. Kang, K. J. Lee, R. R. Dasari, M. S. Feld, and W. Choi, “Overcoming the diffraction limit using multiple light scattering in a highly disordered medium,” *Physical Review Letters*, vol. 107, no. 2, p. 023902, 2011.
- [16] D. Wang, E. H. Zhou, J. Brake, H. Ruan, M. Jang, and C. Yang, “Focusing through dynamic tissue with millisecond digital optical phase conjugation,” *Optica*, vol. 2, no. 8, pp. 728–735, 2015.
- [17] Y. Liu, C. Ma, Y. Shen, J. Shi, and L. V. Wang, “Focusing light inside dynamic scattering media with millisecond digital optical phase conjugation,” *Optica*, vol. 4, no. 2, pp. 280–288, 2017.
- [18] C. Ma, F. Zhou, Y. Liu, and L. V. Wang, “Single-exposure optical focusing inside scattering media using binarized time-reversed adapted perturbation,” *Optica*, vol. 2, no. 10, pp. 869–876, 2015.
- [19] D. Akbulut, T. J. Huisman, E. G. van Putten, W. L. Vos, and A. P. Mosk, “Focusing light through random photonic media by binary amplitude modulation,” *Optics Express*, vol. 19, no. 5, pp. 4017–4029, 2011.
- [20] D. B. Conkey, A. M. Caravaca-Aguirre, and R. Piestun, “High-speed scattering medium characterization with application to focusing light through turbid media,” *Optics Express*, vol. 20, no. 2, pp. 1733–1740, 2012.
- [21] M. Cui and C. Yang, “Implementation of a digital optical phase conjugation system and its application to study the robustness of turbidity suppression by phase conjugation,” *Optics Express*, vol. 18, no. 4, pp. 3444–3455, 2010.
- [22] J. Brake, M. Jang, and C. Yang, “Analyzing the relationship between decorrelation time and tissue thickness in acute rat brain slices using multispeckle diffusing wave spectroscopy,” *JOSA A*, vol. 33, no. 2, pp. 270–275, 2016.

- [23] S. Sun, B. R. Hayes-Gill, D. He, Y. Zhu, and S. P. Morgan, “Multi-exposure laser speckle contrast imaging using a high frame rate cmos sensor with a field programmable gate array,” *Optics Letters*, vol. 40, no. 20, pp. 4587–4590, 2015.
- [24] H. Ruan, M. L. Mather, and S. P. Morgan, “Pulse inversion ultrasound modulated optical tomography,” *Optics Letters*, vol. 37, no. 10, pp. 1658–1660, 2012.
- [25] D. Pine, D. Weitz, P. Chaikin, and E. Herbolzheimer, “Diffusing wave spectroscopy,” *Physical Review Letters*, vol. 60, no. 12, p. 1134, 1988.
- [26] G. Maret and P. Wolf, “Multiple light scattering from disordered media. the effect of brownian motion of scatterers,” *Zeitschrift für Physik B Condensed Matter*, vol. 65, no. 4, pp. 409–413, 1987.
- [27] F. MacKintosh and S. John, “Diffusing-wave spectroscopy and multiple scattering of light in correlated random media,” *Physical Review B*, vol. 40, no. 4, p. 2383, 1989.
- [28] A. B. Parthasarathy, W. J. Tom, A. Gopal, X. Zhang, and A. K. Dunn, “Robust flow measurement with multi-exposure speckle imaging,” *Optics Express*, vol. 16, no. 3, pp. 1975–1989, 2008.
- [29] P.-A. Lemieux and D. J. Durian, “Investigating non-gaussian scattering processes by using nth-order intensity correlation functions,” *J. Opt. Soc. Am. A*, vol. 16, no. 7, pp. 1651–1664, Jul. 1999. DOI: 10.1364/JOSAA.16.001651.
- [30] M. Medebach, N. Freiburger, and O. Glatter, “Dynamic light scattering in turbid nonergodic media,” *Review of Scientific Instruments*, vol. 79, no. 7, p. 073 907, 2008.
- [31] V. Viasnoff, F. Lequeux, and D. Pine, “Multispeckle diffusing-wave spectroscopy: A tool to study slow relaxation and time-dependent dynamics,” *Review of Scientific Instruments*, vol. 73, no. 6, pp. 2336–2344, 2002.
- [32] J. W. Goodman, “Some fundamental properties of speckle,” *JOSA*, vol. 66, no. 11, pp. 1145–1150, 1976.
- [33] R. Mostany and C. Portera-Cailliau, “A craniotomy surgery procedure for chronic brain imaging,” *JoVE (Journal of Visualized Experiments)*, no. 12, e680, 2008.
- [34] A. Cho, C. Yeon, D. Kim, and E. Chung, “Laser speckle contrast imaging for measuring cerebral blood flow changes caused by electrical sensory stimulation,” *Journal of the Optical Society of Korea*, vol. 20, no. 1, pp. 88–93, 2016.
- [35] D. Kobat, N. G. Horton, and C. Xu, “In vivo two-photon microscopy to 1.6-mm depth in mouse cortex,” *Journal of Biomedical Optics*, vol. 16, no. 10, p. 106 014, 2011.

- [36] D. G. Ouzounov, T. Wang, M. Wang, D. D. Feng, N. G. Horton, J. C. Cruz-Hernández, Y.-T. Cheng, J. Reimer, A. S. Tolias, N. Nishimura, *et al.*, “In vivo three-photon imaging of activity of gcamp6-labeled neurons deep in intact mouse brain,” *Nature Methods*, vol. 14, no. 4, pp. 388–390, 2017.
- [37] J. Li, G. Ku, and L. V. Wang, “Ultrasound-modulated optical tomography of biological tissue by use of contrast of laser speckles,” *Applied Optics*, vol. 41, no. 28, pp. 6030–6035, 2002.
- [38] L. Tian, S. A. Hires, T. Mao, D. Huber, M. E. Chiappe, S. H. Chalasani, L. Petreanu, J. Akerboom, S. A. McKinney, E. R. Schreiter, *et al.*, “Imaging neural activity in worms, flies and mice with improved gcamp calcium indicators,” *Nature Methods*, vol. 6, no. 12, p. 875, 2009.
- [39] K. Deisseroth, “Optogenetics,” *Nature Methods*, vol. 8, no. 1, pp. 26–29, 2011.
- [40] T. LaForest, A. Verdant, A. Dupret, S. Gigan, F. Ramaz, G. Tessier, and É. B. à la Guillaume, “Monolithic device for on-chip fast optical phase conjugation integrating an image sensor and a spatial light modulator,” in *Smart Photonic and Optoelectronic Integrated Circuits XVI*, International Society for Optics and Photonics, vol. 8989, 2014, 89890N.
- [41] T. Laforest, A. Dupret, A. Verdant, F. Ramaz, S. Gigan, G. Tessier, and É. B. à la Guillaume, “A 4000 hz cmos image sensor with in-pixel processing for light measurement and modulation,” in *2013 IEEE 11th International New Circuits and Systems Conference (NEWCAS)*, IEEE, 2013, pp. 1–4.
- [42] I. N. Papadopoulos, J.-S. Jouhanneau, J. F. Poulet, and B. Judkewitz, “Scattering compensation by focus scanning holographic aberration probing (f-sharp),” *Nature Photonics*, vol. 11, no. 2, p. 116, 2017.
- [43] M. Kadobianskyi, I. N. Papadopoulos, T. Chaigne, R. Horstmeyer, and B. Judkewitz, “Scattering correlations of time-gated light,” *Optica*, vol. 5, no. 4, pp. 389–394, 2018.

*Chapter 4***IMPROVED LIGHT DELIVERY FOR OPTOGENETICS USING
DIGITAL TIME-REVERSED ULTRASONICALLY-ENCODED
(TRUE) LIGHT FOCUSING**

*This chapter is adapted from the manuscript H. Ruan[†], J. Brake[†], J. E. Robinson, Y. Liu, M. Jang, C. Xiao, C. Zhou, V. Gradinaru, and C. Yang, “Deep tissue optical focusing and optogenetic modulation with time-reversed ultrasonically encoded light,” *Science Advances*, 3(12), eaao5520, 2017. DOI: 10.1126/sciadv.aao5520*

4.1 Abstract

Noninvasive light focusing deep inside living biological tissue has long been a goal in biomedical optics. However, the optical scattering of biological tissue prevents conventional optical systems from tightly focusing visible light beyond several hundred microns. The recently developed wavefront shaping technique time-reversed ultrasonically encoded (TRUE) focusing enables noninvasive light delivery to targeted locations beyond the optical diffusion limit. However, until now, TRUE focusing has only been demonstrated inside non-living tissue samples. Here, we present the first example of TRUE focusing in 2-mm-thick living brain tissue and demonstrate its application for optogenetic modulation of neural activity in 800- μm -thick acute mouse brain slices at a wavelength of 532 nm. We found that TRUE focusing enabled precise control of neuron firing and increased the spatial resolution of neuronal excitation 4-fold when compared to conventional lens focusing. This work is an important step in the application of TRUE focusing for practical biomedical uses.

4.2 Introduction

Optical methods are widely used across biomedical research, as well as for the diagnosis and treatment of disease, yet the ability to monitor and modulate biological processes at depth is conventionally limited by light scattering caused by the heterogeneous optical properties of biological samples. For example, a 532-nm photon experiences an average of nearly 40 scattering events as it travels through 1 mm of mouse brain tissue (scattering mean free path $l \approx 26 \mu\text{m}$) [1, 2], which exemplifies why the formation of an optical focus in typical tissue samples is often

limited to depths of a few hundred microns. In order to focus light deeper inside tissue, wavefront shaping or wavefront engineering methods (3-10) [3–10] have been developed that counteract the effects of optical scattering by modulating the incident light field so that the scattered light controllably interferes at locations of interest to form tight foci. This class of methods provides an advantage over techniques that discard scattered light as noise, such as confocal microscopy, since the probability of photons being unscattered (i.e. ballistic in nature) decays exponentially with increasing depth. The incorporation of scattered photons enables light focusing beyond the optical diffusion limit where the propagation directions of the photons become random [11]. Furthermore, since wavefront shaping techniques actively control scattered light, they offer direct optical modulation, an advantage over other optical imaging techniques such as photoacoustic tomography [11] and diffuse optical tomography [12], which enable deep tissue imaging, but cannot focus light to a particular location for improved light delivery.

The ability to manipulate scattered photons to create a light focus at depth with wavefront shaping is due to the elastic, deterministic nature of optical scattering, which scrambles but does not eliminate the information contained within a light field [13]. Thus, if one could discern the positions and scattering profile of the scatterers within the medium, it would be possible to tailor an incident wavefront to optimally couple light to any point in the tissue. This process can be simplified by mapping the optical phase and/or amplitude relationship between the input plane outside the sample and the targeted plane inside, which can be accomplished through feedback-based approaches [3, 8, 14, 15], transmission matrix measurement [9, 10, 16–19], or optical time reversal (optical phase conjugation) [13, 20–24]. Among these, optical phase conjugation is well-suited for optical focusing in living tissue applications because it allows for measurement of the phase relationship between the target focus and the wavefront solution on the input plane in parallel, thus producing the fastest focusing speeds [25–30]. This feature helps to overcome challenges posed by living tissue dynamics, which require that the wavefront shaping system obtain and playback the wavefront solution before the scatterers' configuration in the tissue changes [25–27, 30]. When used with a guidestar [5], a method for tagging photons that traverse a desired location within the biological sample, the optical phase conjugation approach can create a phase conjugate wavefront that forms a focus at the guidestar location.

Several guidestar mechanisms have been developed that enable the generation of

appropriate input wavefronts. These include fluorescent [31, 32], nonlinear optical [22, 33–36], kinetic [37, 38], photoacoustic [39–42], ultrasonic [43–46], magnetic [47] and microbubble [48] encoded mechanisms. Of these, ultrasound offers the advantage of being non-invasive, freely addressable within the volume of interest, and compatible with optical phase conjugation since it generates coherent tagged light. Time-reversed ultrasonically encoded (TRUE) focusing is a wavefront shaping technique that combines optical phase conjugation with the ultrasound guidestar to enable light focusing at depths beyond the optical diffusion limit with ultrasonic resolution ($\sim 30 \mu\text{m}$) [44–46].

The application of TRUE focusing to living systems would be beneficial to many fields of study, including neurobiological research, in which visible light is routinely used for both monitoring activity with genetically encoded neural activity indicators [49, 50] and controlling activity via optogenetic actuators [51]. While neurophotonic techniques that employ multi-photon excitation [52–57] and adaptive optics [33, 34, 36] have extended the depths of optical access *in vivo*, focusing light noninvasively in the multiple scattering regime in living brain tissue remains largely unexplored. Due to the strongly scattering nature of brain tissue, light delivery during optogenetic manipulation still requires the use of invasive, implanted optical fibers to reach targets in deep brain regions [58]. Since TRUE focusing allows for an optical focus to be formed noninvasively with the ability to freely move the focus within the tissue to target different regions of interest, it is particularly well-suited for optogenetic modulation. Here, we describe the design and application of an integrated TRUE focusing and patch clamp electrophysiology system for simultaneous optogenetic stimulation and neural activity monitoring within living brain tissue *ex vivo*. We first demonstrate light focusing through up to 2 mm thick living brain tissue using diffuse photons with a wavelength of 532 nm. Then, by performing patch clamp recordings in 800 μm -thick acute brain slices and using optogenetically-evoked photocurrents as a readout, we demonstrate that TRUE focusing increases the spatial resolution of neuronal excitation by four times compared to that of conventional focusing at a wavelength of 532 nm. This result represents the first demonstration of TRUE focusing in living brain tissue and is an important step in the translation of wavefront shaping methods into practical optical tools for *in vivo* applications, including optogenetics.

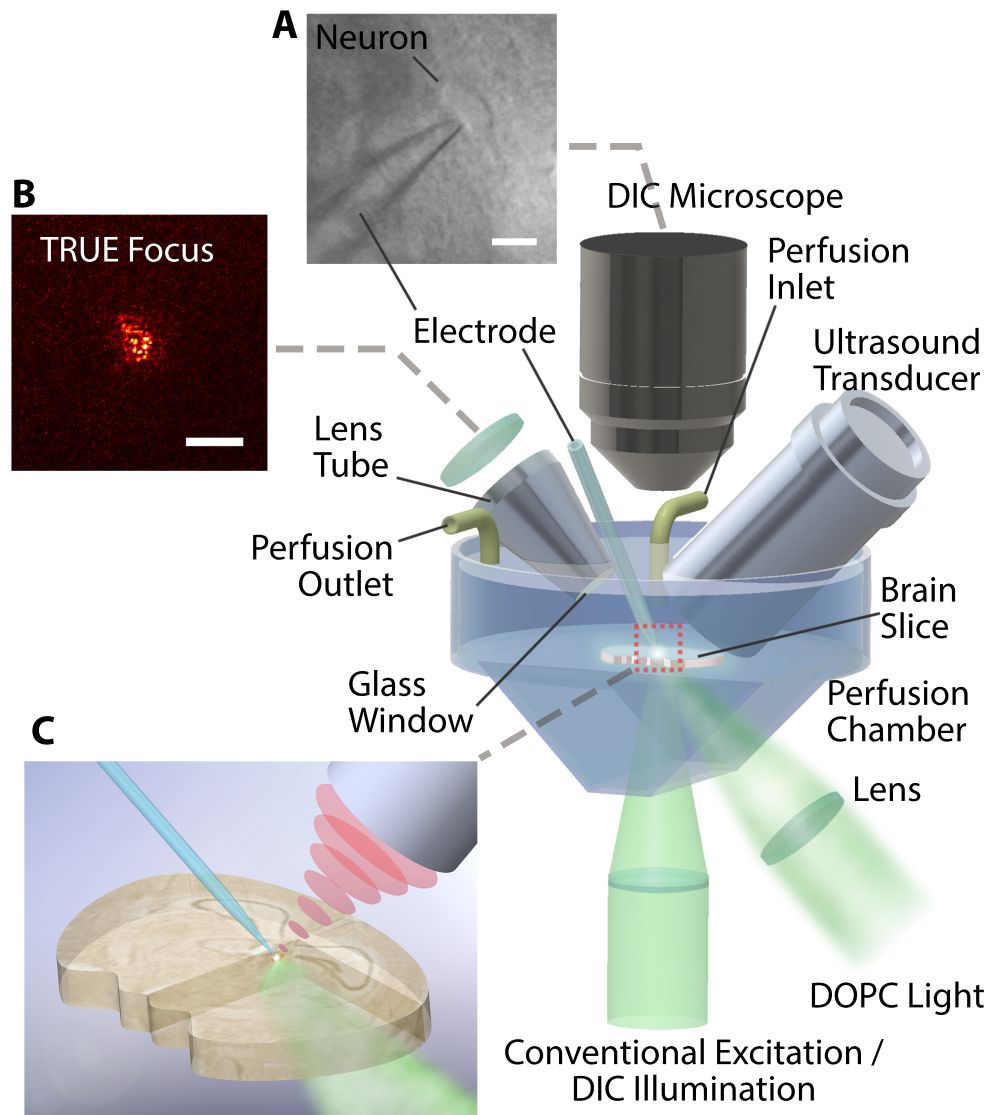


Figure 4.1: Custom TRUE focusing and electrophysiological recording system.

The custom TRUE focusing system combined a digital optical phase conjugation (DOPC) system with a patch clamp electrophysiology amplifier and headstage. Acute brain slices were held in a custom perfusion chamber that contained warmed, carbonated artificial cerebral spinal fluid (aCSF). The TRUE light beam illuminated the tissue at an oblique 45-degree angle while the borosilicate patch pipette electrode was used for neurophysiological measurements. (A) A DIC microscope was included for neuron visualization during patch clamping. (B) The TRUE focusing system allowed light to be sharply focused through the brain slice. (C) A close-up image of the TRUE focus on a patched neuron. Scale bars: 20 μm in (A) and 50 μm in (B).

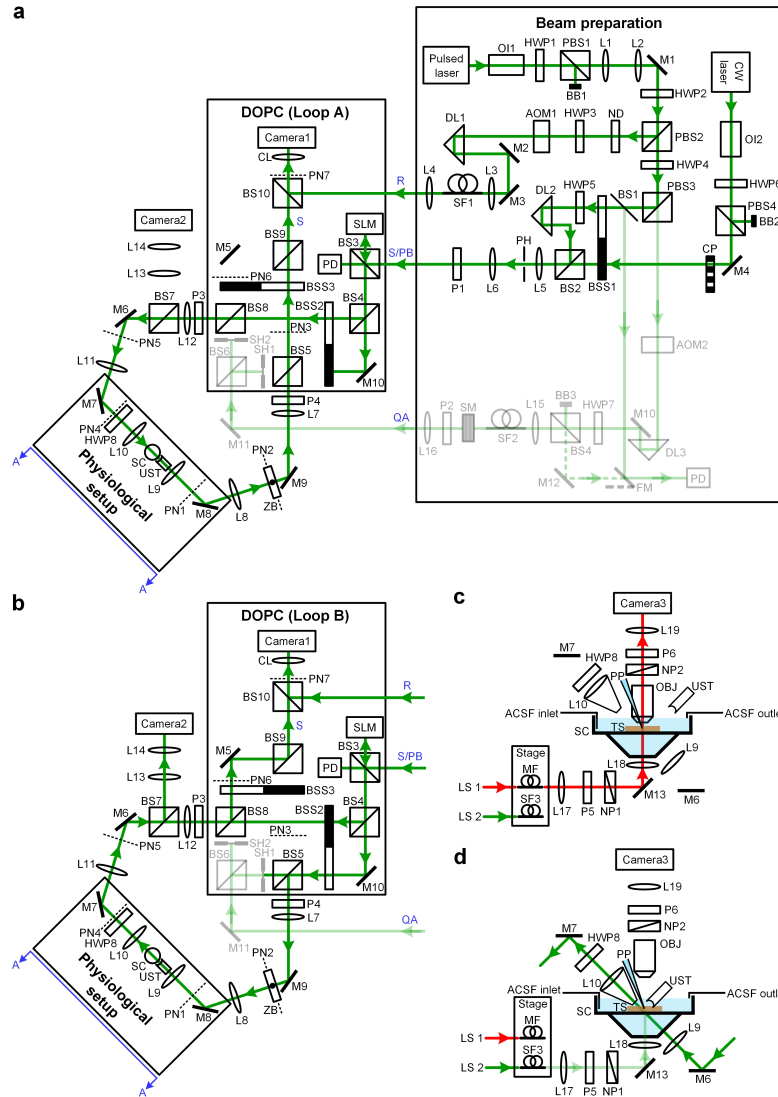


Figure 4.2: **Schematic of the TRUE focusing system.** (A-B) Schematic of the setup for DOPC Loop A and Loop B. (C) The physiological setup (the A-A section in A and B) running in the neuron observation and patching mode. (D) The physiological setup running in the neuron stimulation mode. Abbreviations: ACSF, artificial cerebrospinal fluid; AOM, acousto-optic modulator; BB, beam block; BS, beamsplitter; BSS, beam selecting shutter; CL, camera lens; CP, chopper; CW laser, continuous-wave laser; DL, delay line; FM, flip mirror; HWP, half-wave plate; L, lens; LS, light source; M, mirror; MF, multi-mode fiber; ND, neutral-density filter; NP, Nomarski prism; OI, optical isolator; P, polarizer; PB, playback beam; PBS, polarizing beamsplitter; PD, photodiode; PH, pinhole; PN, plane; PP, pipette; QA, quality assurance; R, reference beam; S, sample beam; SC, sample chamber; SF, single-mode fiber; SH, optical shutter; SLM, spatial light modulator; SM, scattering medium; TS, tissue slice; UST, ultrasonic transducer; ZB, zeroth-order block (a black 100 μm -diameter disk printed on a transparency).

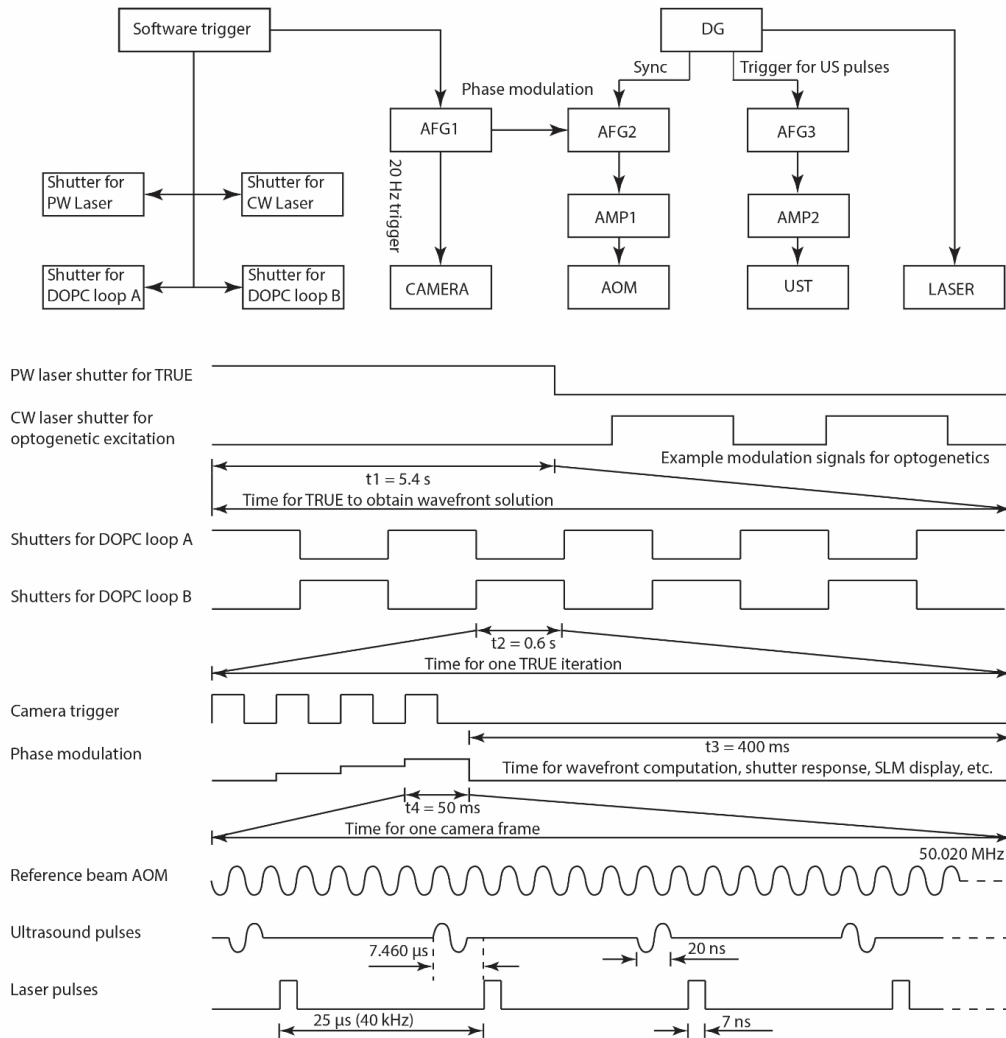


Figure 4.3: Electrical signal flow diagram. The experiment can be divided into two phases. In the first phase, the TRUE focusing system searches for the wavefront solution using a pulsed-wave (PW) laser. After that, we switch to a continuous-wave (CW) laser by controlling the shutters using software triggers. To obtain a correct wavefront solution, we implement nine iterations of the TRUE focusing process by switching the shutters that select between DOPC loop A and B. In each DOPC loop, a four-step phase-shifting holography approach is used to measure the optical field of the ultrasound modulated light. In this case, an arbitrary function generator (AFG1) is used to synchronize the camera and the phase of the reference beam. The frequency of the reference beam is shifted by 50.020 MHz by AFG2. The reference beam shares a clock with the ultrasound pulses and lasers pulses, both of which are triggered at 40 kHz. A 7.46 μs delay is used to compensate for the propagation time of the ultrasound wave traveling to the ultrasound focus. Abbreviations: AFG, arbitrary function generator; AMP, amplifier; AOM, acousto-optic modulator; DG, delay generator; UST, ultrasound transducer.

4.3 Results

System design and operating principles

In order to achieve TRUE focusing in living brain tissue *ex vivo*, we designed and implemented a digital optical phase conjugation (DOPC) system [21, 22] for TRUE focusing (Fig. 4.2-4.3) that included an integrated patch clamp electrophysiology head stage and amplifier for neurophysiological measurements, as well as a removable differential interference contrast (DIC) microscope for neuron visualization while whole cell recordings were being obtained (Fig. 4.1). A customized sample chamber was designed that allowed acute brain slices to rest horizontally while constantly perfused with carbogenated artificial cerebral spinal fluid (aCSF). Because this setup limited the orientations of the TRUE focusing light path and the ultrasound transducer to oblique angles, we illuminated the slice at a 45-degree angle with the ultrasound transducer positioned orthogonal to the TRUE light beam to maximize the modulation efficiency. In order to allow for the use of high numerical aperture (NA) lenses (for the DIC microscope objective, collection lens, and ultrasound transducer) with relatively short working distances to be operated within the limited available space, the observation objective, collection lens with lens tube, and ultrasound transducer were placed on computer controlled motorized stages so they could be precisely translated in and out of the bath. In order to prevent fluctuations of the perfusion fluid surface from influencing the wavefront measurement, we attached a glass window to the lens tube and immersed it in the aCSF solution. This normally incident design also avoids unnecessary refraction at the aCSF-air interface. Similarly, the bottom of the chamber was also designed with a 45-degree chamber-air interface, which minimizes the effects of refraction and helps with optical alignment.

The creation of a TRUE focus involved sequential wavefront recording (Fig. 4.4A1) and playback (Fig. 4.4A2) steps. In the recording step, a high-frequency (50 MHz) ultrasound field was focused to the location of interest while a probe light beam generated by a pulsed 532 nm laser illuminated the sample. Due to the acousto-optic effect, the frequency of a portion of the light passing through the ultrasound focus was shifted by the ultrasound frequency. The field of the scattered, ultrasound-tagged light was measured by the camera of the DOPC system using interferometry [59]. Then, in the playback step, the phase conjugate version of the phase map of the ultrasound-tagged light was displayed on the spatial light modulator (SLM) of the DOPC system and used to create the playback light field. Following the principle of time-reversal, this playback beam scattered in a time-reversed fashion and formed

an optical focus at the location of the ultrasound focus. Our TRUE focusing system described here relied on a digital wavefront recording and playback engine [21, 22], which, compared with analog TRUE focusing systems [44], allowed for measured wavefronts to be played back at a light intensity far greater than that of the measured wave [45]. The average intensity of the TRUE focus compared to the background intensity for phase-only modulation of the wavefront is given by Equation 4.1 [32]:

$$\eta_{\text{phase-only}} = \frac{\pi}{4} \times \frac{(N - 1)}{M} + 1 \quad (4.1)$$

where N is the number of optical modes controlled by the SLM and M is the number of optical modes (speckle grains) within the ultrasound focus. The size of the TRUE focus along the ultrasound beam lateral direction is dictated by the diffraction limited focused ultrasound beam diameter and the size along the ultrasound beam axial direction is determined by the ultrasound and laser pulse widths. In order to enhance the spatial resolution and contrast of TRUE focusing, we used an iterative TRUE focusing scheme [60–62], where the intensity and resolution of the TRUE focus was iteratively enhanced by repeating the TRUE focusing procedure using a previously established TRUE focus. A random phase pattern was displayed on the SLM to initiate the iterative TRUE focusing process. Rather than using two DOPC systems as previously demonstrated [61], we designed and implemented the iterative TRUE focusing system in transmission mode using a single DOPC system (see Methods and Fig. 4.2-4.3 for detailed descriptions).

A comparison between TRUE and conventional focusing in living brain slices

In order to test the performance of our system, we prepared acute brain slices (300 – 2000 μm) that contained the medial prefrontal cortex (mPFC) from C57Bl/6J mice using a vibrating microtome as previously described [63, 64]. Then, we placed the slices in our optical setup and recorded the light intensity profile through the slices formed by our TRUE focusing system (Fig. 4.4A1-A2) and a conventional lens (Fig. 4.4B). As predicted, the conventional focusing lens failed to form a tight optical focus and demonstrated a light profile that broadened as the brain slice thickness was increased due to the strong scattering nature of the tissue (Fig. 4.4C, top row). While a visible envelope of the intensity profile was observed when light was conventionally focused through a 500- μm -thick slice, the lateral width of the focus profile was significantly increased from the diffraction limited focus size of $\sim 1 \mu\text{m}$ (the NA of the focusing lens was 0.25). The size of the conventional focus

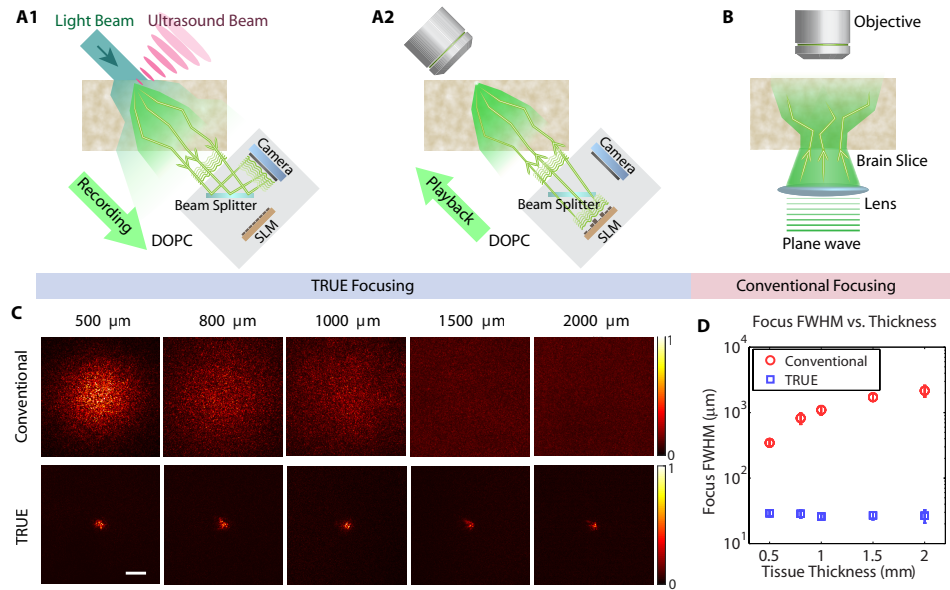


Figure 4.4: A comparison of TRUE focusing and conventional focusing. (A) The recording (A1) and playback (A2) procedures used to focus light through the slice onto its top surface with TRUE focusing. (B) Diagram of the experimental setup for measuring the light intensity distribution of the focus on the top surface of the brain slice achieved using a conventional lens illuminating the brain slice from below. A tube lens and a camera used together with the objective are not shown. (C) Images of the conventional and TRUE focus profile through living brain tissue slices (500, 800, 1000, 1500, and 2000 μm thick). (D) Full width at half maximum (FWHM) focal spot sizes for the conventional and TRUE foci as a function of tissue thickness. Error bars represent the standard deviation of five measurements taken at different locations. Scale bar: 100 μm.

continued to broaden as slice thickness was increased, and no discernible focus envelope was visible within the $580 \times 580 \mu\text{m}^2$ field of view in the 1000 μm or thicker slices.

In contrast, TRUE focusing was able to maintain a lateral resolution defined by the size of the ultrasound focus, decoupling the size of the focus from the focusing depth (Fig. 4.4C, bottom row). Our system employed a high-frequency ultrasound transducer with a 50 MHz nominal center frequency, a 6.35 mm aperture, and a 12.7 mm focal length. The theoretical beam diameter (-6 dB) for this configuration was $\sim 80 \mu\text{m}$ and the calibrated waveform duration (-6 dB) was 37.4 ns, corresponding to a pulse length of 55.3 μm. The region of ultrasound modulated light along

the axial direction of the ultrasound beam was also determined by the combination of the ultrasound pulse length and the laser pulse duration, which is 7 ns. Using the iterative TRUE focusing method enabled the TRUE focus to be tightened [60] to achieve a focus with an average full width at half maximum (FWHM) spot size of 27.4 μm across tissue thicknesses from 500 to 2000 μm .

To calculate the focal spot size of TRUE focusing from the images captured with the observation camera (Camera2 in Fig. 4.2), the image was first cropped to a region (82×82 pixels) surrounding the focus profile, and was low-pass filtered by a 3×3 averaging filter to smooth the speckle. Then, the focus profile was fit using a 2D Gaussian function $f(x, y) = A \exp \left\{ -\frac{[(x-x_0)^2 + (y-y_0)^2]}{(2\sigma^2)} \right\} + B$, where A , B , x_0 , y_0 , and σ are the fitting parameters. The full width at half maximum (FWHM) focal spot size was obtained by $\text{FWHM} = 2\sqrt{2 \ln 2} \sigma$. The focal spot size of conventional focusing was calculated in a similar way. However, since the focal spot size was much larger than that of TRUE focusing, the fitting was applied to a region composed of 1040×1392 pixels.

In contrast, the FWHM of the conventional focus broadened from $\sim 350 \mu\text{m}$ at a slice thickness of 500 μm to approximately 2100 μm at a thickness of 2000 μm (Fig. 4.4D). It should be noted that the effective thicknesses in the TRUE focusing case are larger than the physical thicknesses of the slices due to the 45-degree incident angle of the TRUE focusing beam. These results demonstrate the ability of TRUE focusing to overcome optical scattering to create high-resolution optical foci in living brain slices up to 2000- μm thick, which, unlike those formed by conventional focusing, do not significantly broaden with increased sample thickness.

Application of TRUE focusing for optogenetic manipulations

After demonstrating the ability of TRUE focusing to overcome optical scattering and produce light foci in thick acute brain slices, we next sought to demonstrate the advantage of TRUE for optogenetic manipulation compared to conventional focusing using a neurophysiological readout. Optogenetics, in which engineered light-gated ion channels or pumps are used to manipulate cellular activity with high spatial and temporal precision using visible light, has become relatively ubiquitous in basic neurobiological research due to its ability to convert differences in light intensity into graded electrophysiological signals [51]. Although a wide range of optogenetic actuators are available for neural excitation or inhibition with diverse excitation spectra spanning the visible spectrum, we used the excitatory,

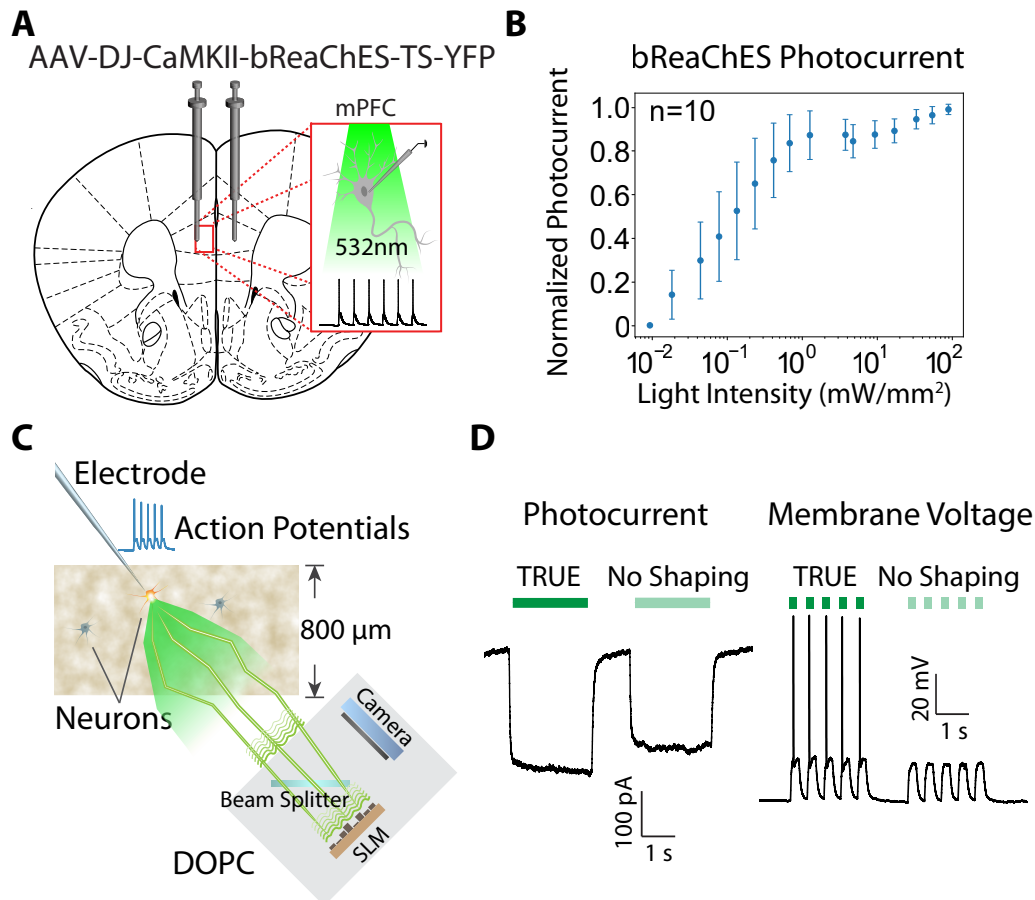


Figure 4.5: Experiment design, opsin characterization, and demonstration of photocurrent and firing modulation via TRUE focusing. (A) An AAV vector was used to stereotactically deliver the bReaChES transgene to the medial prefrontal cortex (mPFC). (B) Characterization of normalized photocurrent response vs. light intensity. The average maximum photocurrent across the 10 cells studied was 1047 pA. (C) Diagram illustrating the experimental scheme used to demonstrate the ability of TRUE focusing to elicit action potentials through 800 μ m thick living mouse brain tissue. (D) Representative traces demonstrating elicited photocurrent and membrane voltage changes achieved with and without TRUE focusing.

red-shifted opsin bReaChES for our experiments because its excitation peak was well-matched with our laser source (532 nm) [65]. In order to prepare samples for testing, we performed stereotaxic injections of an adeno-associated viral vector carrying the bReaChES transgene (AAV-DJ-CaMKII-bReaChES-TS-YFP) into the mPFC of C57Bl/6J mice (Fig. 4.5A). After waiting four weeks for surgical recovery and transgene expression, we prepared acute brain slices for simultaneous electrophysiological recording and optical testing. Animal husbandry and all experimental procedures involving animal subjects were approved by the Institutional Animal Care and Use Committee (IACUC) and by the Office of Laboratory Animal Resources at the California Institute of Technology under IACUC protocol 1650. We characterized the performance of bReaChES in cortical slices by measuring the photocurrent response to a wide range of 532 nm light intensities delivered through the DIC objective in voltage clamp mode. Similar to its parent opsin ReaChR [66], bReaChES displayed a nonlinear increase in photocurrent response that saturated at an intensity of approximately 10 mW/mm^2 (Fig. 4.5B). During these experiments, the average maximum photocurrent across the 10 cells studied was 1047 pA.

To demonstrate the capability of TRUE focusing for neural modulation, whole-cell patch clamp recordings were obtained from layer II/III neurons just below the superficial surface of mPFC slices using borosilicate glass patch pipette electrodes visualized under DIC microscopy (Fig. 4.1 and Fig. 4.2C). While TRUE focusing through slices up to 2 mm thick was achieved, maximum slice thickness during our optogenetic experiments was limited to $800 \mu\text{m}$, since neurons in thicker slices were difficult to visualize with DIC microscopy and were generally less healthy, which negatively affects recording and data quality. Because target neurons were located close to the surface of the brain slice for visualization, the DOPC playback beam illuminated from the bottom of the slice traversed almost the entire sample thickness, which is much larger than the optical diffusion limit of the acute mouse brain slice ($\sim 200 \mu\text{m}$ at 532 nm) [2]. Moreover, since the incident angle was 45 degrees (Fig. 4.5C), the effective thickness for TRUE focusing was even larger than the physical slice thickness. Once a whole-cell recording was successfully initiated, the DIC microscope objective was removed, and the lens tube and ultrasound transducer were lowered into the bath.

To ensure co-localization of the ultrasound focus with the pipette tip, we used pulse-echo ultrasound to form an image of the glass pipette tip (Fig. 4.6) and moved the ultrasound transducer to focus on the end of the tip where a target neuron was

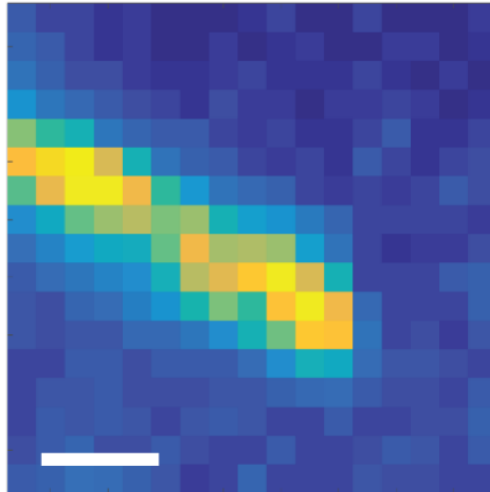


Figure 4.6: Ultrasound pulse-echo image of the tip of the glass pipette electrode. To focus ultrasound to the targeted neuron that is patch-clamped by the glass pipette, the ultrasound transducer is scanned to image the pipette tip in pulse-echo mode. The echo is recorded at each scanning position to form an image of the tip where the neuron is located. The transducer is then moved to that location so that the ultrasound focus overlaps with the neuron. Scale bar, 100 μm .

located. This approach allowed precise targeting of the TRUE focus to the recording neuron in order to maximize light delivery during optogenetic stimulation.

Next, we measured the photocurrent response that was elicited by the TRUE focus; as a control, we created a ‘no wavefront shaping’ condition by shifting the wavefront solution on the SLM by 100 pixels in each lateral direction, which generally approximated the laser background intensity. In this case, the TRUE focus outperformed the no shaping condition, evoking a larger photocurrent due to enhanced light intensity at the focus (Fig. 4.5D, left). The photocurrent enhancement factor, defined as the ratio between the difference of the photocurrent with and without TRUE focusing and the photocurrent without TRUE focusing, was on average 30% ($n = 6$) in 800 μm -thick brain slices, which was similar in magnitude to the enhancement observed in 300- μm and 500- μm slices (Fig. 4.7). To verify the effect of the ultrasound guidestar, we turned off the ultrasound and repeated the same procedure. In this case, since there was no guidestar for the system to focus to, no TRUE focus was formed, resulting in a smaller evoked photocurrent and no observed firing events (Fig. 4.8). Because the presence of the ultrasound field could potentially alter neural activity, we verified in several neurons that focused ultrasound alone in the absence of light failed to evoke any observable current in voltage clamp or alter

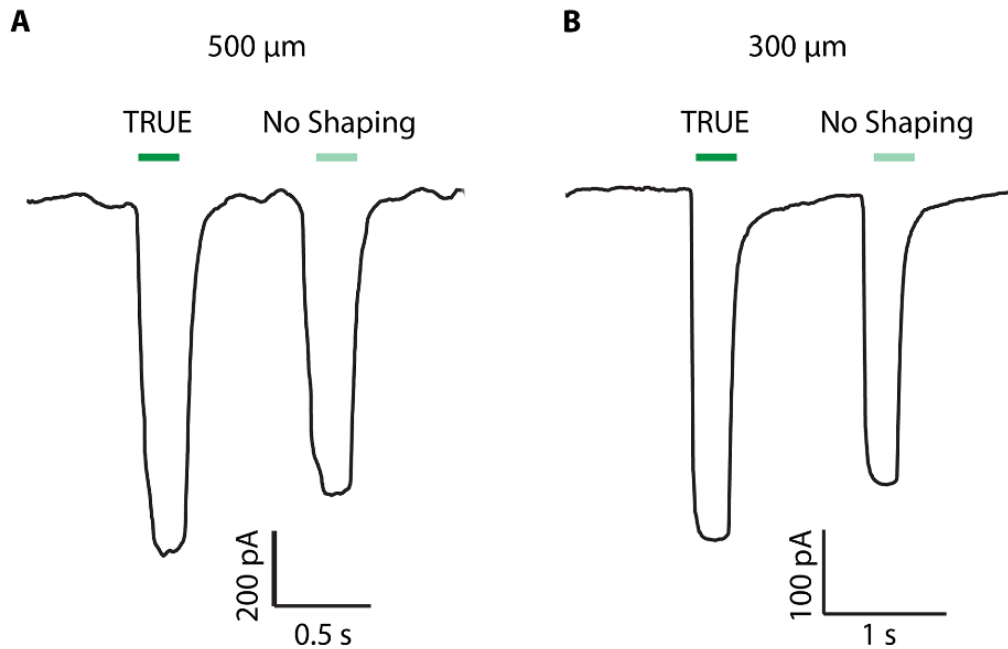


Figure 4.7: **Electrophysiological photocurrent traces from neurons in 500 μm and 300 μm thick acute brain slices.** TRUE focusing enables photocurrent enhancement at depths of 500 μm (A) and 300 μm (B) in addition to the 800 μm thickness shown elsewhere.

neuronal excitability in current clamp mode.

We next sought to evaluate the performance of our system by comparing the experimentally observed enhancement factor with the expected enhancement predicted by the technical specifications of our system and the observed TRUE focus size. The SLM employed in the DOPC system had 2×10^6 pixels, which allows us to focus light through a highly scattering medium to a single optical mode with an experimental peak focus intensity to background ratio η of $\sim 1 \times 10^4$. This experimental performance means the DOPC system could effectively control $N \sim 1 \times 10^4$ optical modes. Based on this performance, we were able to estimate the intensity enhancement at the ultrasound focus using Equation 4.1. Since our system produced a TRUE focus with a FWHM diameter of $\sim 27 \mu\text{m}$, the number of modes M inside the focus was $\sim 1 \times 10^4$, which corresponded to a predicted intensity enhancement factor at the ultrasound focus of approximately 2. Since the photocurrent enhancement was not proportional to light intensity (Fig. 4.5B), we predicted that the photocurrent enhancement factor would be less than 1, which was consistent with our data. De-

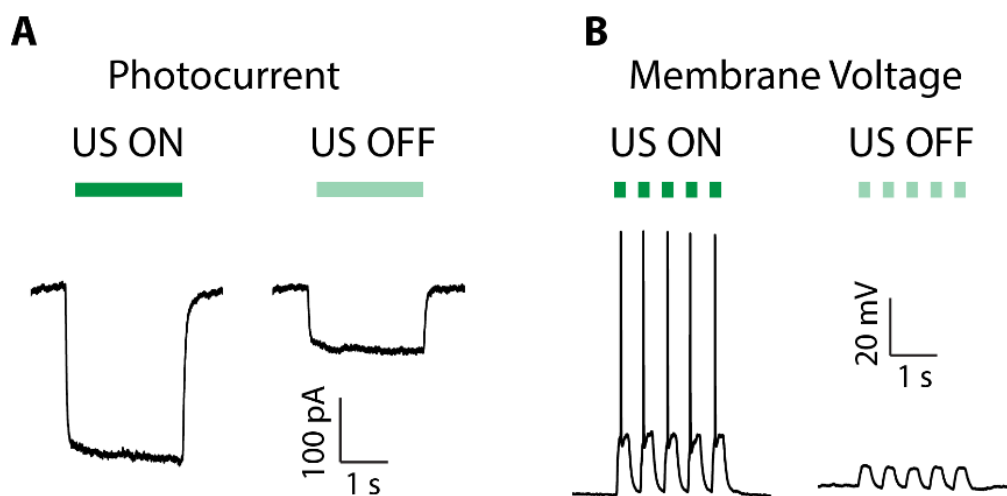


Figure 4.8: **Electrophysiological photocurrent and membrane voltage traces comparing ultrasound on and off conditions.** (A) Photocurrent traces when performing the TRUE focusing procedure with the ultrasound on and off. When the ultrasound is on, a phase map is measured which enables light to be focused to the location of the ultrasound focus and the neuron cell body. In contrast, when the ultrasound is disabled by turning off its driving amplifier, an incorrect phase map is measured so that the playback beam is not focused onto the neuron. As a result, we see a decrease in the amplitude of the photocurrent. (B) Membrane voltage traces when performing the TRUE focusing procedure with the ultrasound on and off. When the ultrasound is on, the playback beam is focused onto the neuron and elicit action potentials. In comparison, when the ultrasound is off, light is not focused onto the neuron and therefore no action potentials are elicited. It should be noted that the photocurrent and membrane voltage are lower with ultrasound off than those with ultrasound on followed by a shifted TRUE phase map displayed on the SLM (Fig. 4.5) which leads to an artificially increased photocurrent enhancement since the overall energy in the “US OFF” condition is lower than in the “No Shaping” condition. This is because the random phase map measured with ultrasound off has a higher spatial frequency ($1/\text{pixel size}$) than that of a normal phase map, and these high frequency components are filtered out by the limited numerical aperture of the optical system. In contrast, the shifted phase pattern in the “No Shaping” condition does not change the spatial frequency distribution of the phase map measured with ultrasound on and therefore maintains the same background intensity level as the background of the TRUE focus.

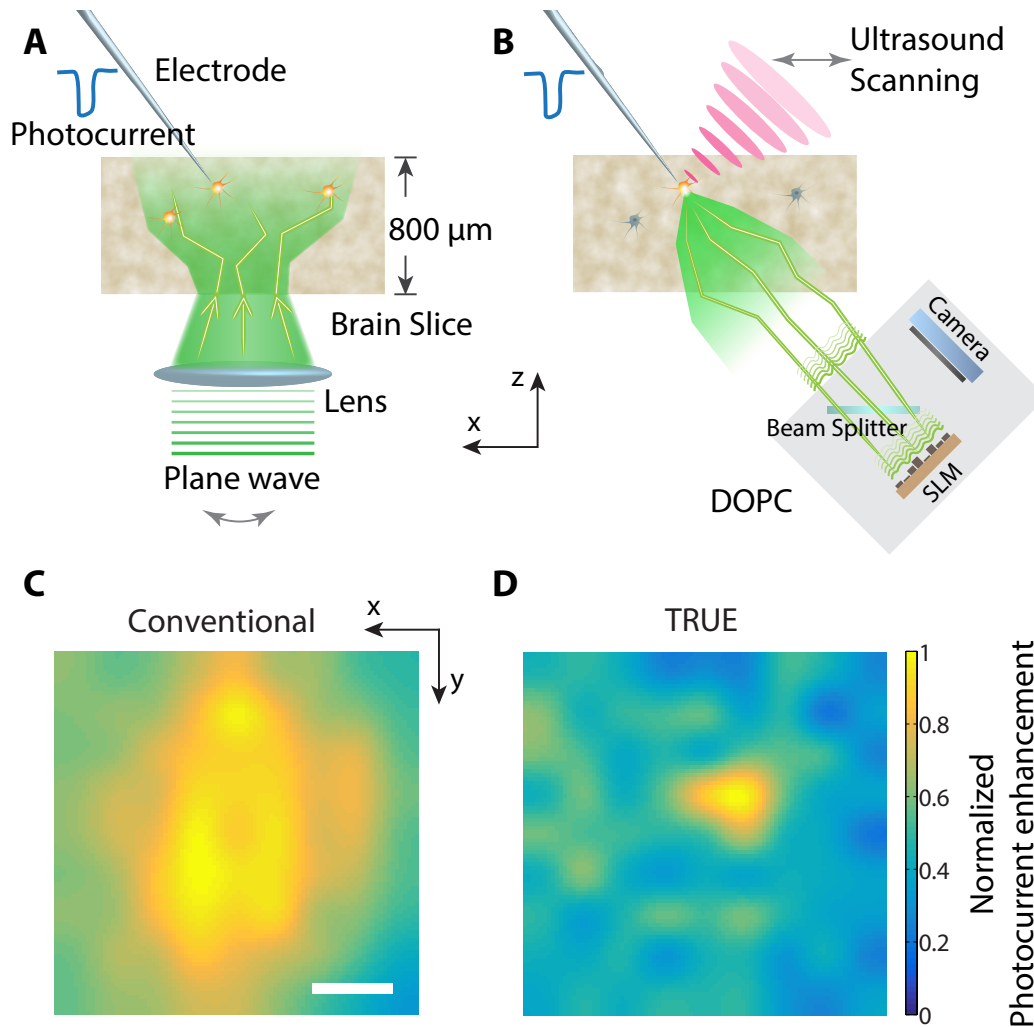


Figure 4.9: **Spatial resolution of optogenetic stimulation achieved by conventional versus TRUE focusing.** Experimental configuration for photocurrent scan map generation using conventional focusing (A) and TRUE focusing (B). The normalized photocurrent enhancement as a function of lateral focal scanning position for conventional (C) and TRUE focusing (D). Scale bar: 100 μm .

spite the observed enhancement, the laser power could be adjusted so that the TRUE focus elicited time-locked cell firing, whereas the no shaping condition could not elicit action potentials (Fig. 4.5D, right).

Improved spatial resolution of optogenetic stimulation using TRUE focusing

After demonstrating that TRUE-focused light could optogenetically stimulate neurons at depths beyond the optical diffusion limit, we compared the spatial resolution

of TRUE focusing with that of conventional lens focusing for optogenetic modulation. The ability for TRUE focusing to noninvasively enhance the light intensity in a spatially restricted manner is an important benefit compared to other conventional methods for delivering light into the brain, such as optical fibers or LED implants, which do not allow for the targeted volume to be freely moved within the brain after implantation. To quantify the spatial resolution of TRUE focusing and conventional focusing, we raster-scanned the focus of each case laterally around a patch-clamped neuron and recorded the photocurrent magnitude at each scanning position (Fig. 4.9A-B). In both cases, we scanned over a square grid of 9×9 points with a $50\text{-}\mu\text{m}$ step size in each dimension on the horizontal plane. For conventional focusing, the 780-nm wavelength DIC illumination LED was replaced with the 532-nm wavelength laser source delivered via a single mode optical fiber whose tip was imaged to the plane of the targeted neuron to form a focus (Fig. 4.2D). The position of the focus was calibrated using the observation microscope before placing the brain slice in the chamber, and the focus was raster-scanned on the horizontal plane during whole cell recordings (Fig. 4.2C-D). The normalized photocurrent enhancement was calculated at each scanning position and used to construct interpolated two-dimensional scan maps (Fig. 4.9C-D). Fitting the conventional lens scan map with a 2D Gaussian function yielded respective FWHMs of 393 and $536\text{ }\mu\text{m}$ in the x and y dimensions. In contrast, the FWHMs for the TRUE focusing scan were 99 and $71\text{ }\mu\text{m}$ in the x and y dimensions. Due to the scattering and diffusion of the conventional illumination, the spatial extent of the evoked photocurrent enhancement with conventional illumination was nearly 4 times broader than that obtained with TRUE focusing, thus confirming the utility of TRUE focusing for precise spatial focusing at depth beyond the optical diffusion limit.

4.4 Discussion

Overcoming optical scattering to noninvasively extend the depth at which light can be tightly focused inside living biological samples in clinical and research settings is of great interest to practitioners and researchers alike. In this work, we developed a TRUE focusing system that allowed us to focus light at depth in *ex vivo* brain tissue with a spatial resolution that significantly outperformed conventional lens focusing. By integrating a patch clamp electrophysiology headstage and amplifier into the TRUE focusing system, we were able to monitor neural activity during optogenetic stimulation with the TRUE focus. Using neurophysiological signals as a readout, we confirmed that TRUE focusing can be used to control neural

activity in thick tissue samples in a spatially restricted manner. Since optogenetic manipulations currently require the surgical implantation of invasive optical fibers for light delivery below the most superficial brain regions [58], we believe that our findings using TRUE focusing will inform future efforts to develop this technology for non-invasive optogenetic stimulation and/or fluorescent imaging *in vivo* with the spatial resolution required for precise targeting of individual neurons or neurons ensembles.

Multiphoton microscopy is capable of obtaining clear images at depths of 800 μm and is promising for neuromodulation at that depth. However, the fundamental working depth of this technique is limited by the number of unscattered or weakly scattered photons, which decreases exponentially with depth. In contrast, the TRUE focusing technique is able to focus light beyond the ballistic photon regime. The addressable depth of the TRUE focusing technique demonstrated in this set of optogenetic experiments was limited by the penetration depth of the DIC microscope illumination necessary to visualize neurons during the initiation of patch clamp recordings, as well as the viability of the neurons in thick tissue. While fluorescent activity indicators, such as the GCaMP family of proteins [67], would provide a viable activity readout in thicker tissue samples, these tools were not practical for use here given that the excitation wavelength for calcium indicators is likely to simultaneously excite neurons with opsins that match the operating wavelength of the TRUE focusing system (532 nm). In the future, this problem could be solved by decoupling the wavelength for TRUE focusing and optogenetic excitation from that for calcium indicator excitation. It would also be valuable to explore the maximum penetration depth of TRUE focusing for optogenetics, even if it would require minimally invasive methods *in vivo* such as optical fiber insertion for signal readout.

Unlike in *ex vivo* tissue preparations where cell viability is a limiting factor for tissue thickness, the focusing depth during *in vivo* applications is limited by the guidestar efficiency. As we focus deeper into tissue, fewer photons from the guidestar can be measured, not only because the detected portion of light from guidestar is reduced, but also because of a decrease in the modulation efficiency due to ultrasound attenuation. Although the DOPC system works even when the measured phase map has less than a photon per degree of freedom [68] (i.e. SLM or camera pixel), the presence of shot noise due to the much higher unmodulated light intensity will fundamentally limit the penetration depth [24, 69]. Additional guidestar aids, such

as microbubbles, can help improve the tagging efficiency significantly [48] but sacrifice the freely addressable and noninvasive nature of the ultrasound guidestar. In the future, it will be important to optimize the intensity of the measured ultrasound modulated light to extend the penetration depth.

Another goal for future developments of TRUE focusing for optogenetic stimulation is improved photocurrent enhancement. Using whole cell recordings, we observed a photocurrent enhancement of approximately 30% compared to the no shaping condition, which was consistent with predicted values but will require improvement before TRUE focusing is feasible for widespread use in optogenetic applications. The avenues to improve the focusing contrast are based on the variables in Eq. 4.1. From this equation, we can see that in order to enhance the focusing contrast we can either increase N , the number of controllable modes, or decrease M , the number of optical modes within the ultrasound focus. One way to reduce M is by reducing the size of the ultrasound focus by increasing the operating frequency and the NA of the ultrasound transducer. However, high-frequency ultrasound has a very limited penetration depth. Furthermore, since the goal is to enhance the light intensity delivered to the neuron soma, shrinking the size of the focus beyond the size of the cell will not necessarily lead to further improvements in photocurrent enhancement, although this strategy may allow for finer resolution targeting of neuronal subcompartments, such as individual dendrites or synaptic inputs. Another strategy is to increase the size of the optical modes by shifting to longer wavelengths, although opsins sensitive to infrared or near infrared wavelengths will need to be further refined before they are practical for single photon *in vivo* applications [70, 71]. A more feasible avenue to improve the TRUE focus contrast is to increase the number of controllable optical modes, N . This can be achieved by scaling up the number of SLM pixels, which will also benefit other general applications across the wavefront shaping field. For example, increasing the number of SLM pixels N by 10 times will result in a focus intensity to background ratio $\eta \approx 12$, which is sufficient for many practical applications.

To translate wavefront shaping into practical tools for *in vivo* applications, we also need to address the challenge of the optical decorrelation of living tissue. The dynamic nature of living tissue causes decorrelation of the optical wavefronts, so to effectively focus light inside living tissue, the system response time must be shorter than the decorrelation time of the tissue. For acute brain slices less than 2 mm in thickness, this decorrelation time is on the order of several seconds [72], which is

longer than the current TRUE focusing speed (0.6 s, see Fig. 4.3). However, the decorrelation time drops to the order of one millisecond for *in vivo* applications due to blood flow, cardiac motion, breathing, etc. [26, 73, 74]. In order to increase the response speed of wavefront shaping systems, digital micromirror devices (DMDs) and ferroelectric liquid crystal based SLMs have been employed to achieve high-speed DOPC within 10 milliseconds [25, 27], which is ultimately limited by the need to read out and transfer data to a computing device such as a PC or an embedded system, to compute the appropriate wavefront solution.

We expect that solving these problems will require an integrated wavefront shaping system that combines the wavefront sensing and modulation devices into a single device [75]. This design will allow for control over an increased number of optical modes in a scalable way without sacrificing the operation speed, since wavefront calculations can be performed in parallel on a per-pixel basis, minimizing data transfer and computation time. The development of such an integrated wavefront sensing and modulation platform will increase the achievable enhancement factors. Simultaneously, it will remove many of the challenges that limit the widespread adoption of wavefront shaping techniques, such as the difficulty of designing and aligning the complex optical system [76], opening the door for more scientists to incorporate wavefront shaping into their optical technologies for biomedicine and beyond.

References

- [1] S. Schott, J. Bertolotti, J.-F. Léger, L. Bourdieu, and S. Gigan, “Characterization of the angular memory effect of scattered light in biological tissues,” *Optics Express*, vol. 23, no. 10, pp. 13 505–13 516, 2015.
- [2] M. Mesradi, A. Genoux, V. Cuplov, D. Abi-Haidar, S. Jan, I. Buvat, and F. Pain, “Experimental and analytical comparative study of optical coefficient of fresh and frozen rat tissues,” *Journal of Biomedical Optics*, vol. 18, no. 11, p. 117 010, 2013.
- [3] I. M. Vellekoop and A. Mosk, “Focusing coherent light through opaque strongly scattering media,” *Optics Letters*, vol. 32, no. 16, pp. 2309–2311, 2007.
- [4] A. P. Mosk, A. Lagendijk, G. Lerosey, and M. Fink, “Controlling waves in space and time for imaging and focusing in complex media,” *Nature Photonics*, vol. 6, no. 5, pp. 283–292, 2012.

- [5] R. Horstmeyer, H. Ruan, and C. Yang, “Guidestar-assisted wavefront-shaping methods for focusing light into biological tissue,” *Nature Photonics*, vol. 9, no. 9, p. 563, 2015.
- [6] H. Yu, J. Park, K. Lee, J. Yoon, K. Kim, S. Lee, and Y. Park, “Recent advances in wavefront shaping techniques for biomedical applications,” *Current Applied Physics*, vol. 15, no. 5, pp. 632–641, 2015.
- [7] S. Rotter and S. Gigan, “Light fields in complex media: Mesoscopic scattering meets wave control,” *Reviews of Modern Physics*, vol. 89, no. 1, p. 015 005, 2017.
- [8] I. M. Vellekoop, “Feedback-based wavefront shaping,” *Optics Express*, vol. 23, no. 9, pp. 12 189–12 206, 2015.
- [9] S. Popoff, G. Lerosey, M. Fink, A. C. Boccara, and S. Gigan, “Controlling light through optical disordered media: Transmission matrix approach,” *New Journal of Physics*, vol. 13, no. 12, p. 123 021, 2011.
- [10] M. Kim, W. Choi, Y. Choi, C. Yoon, and W. Choi, “Transmission matrix of a scattering medium and its applications in biophotonics,” *Optics Express*, vol. 23, no. 10, pp. 12 648–12 668, 2015.
- [11] L. V. Wang and S. Hu, “Photoacoustic tomography: In vivo imaging from organelles to organs,” *science*, vol. 335, no. 6075, pp. 1458–1462, 2012.
- [12] D. A. Boas, D. H. Brooks, E. L. Miller, C. A. DiMarzio, M. Kilmer, R. J. Gaudette, and Q. Zhang, “Imaging the body with diffuse optical tomography,” *IEEE Signal Processing Magazine*, vol. 18, no. 6, pp. 57–75, 2001.
- [13] Z. Yaqoob, D. Psaltis, M. S. Feld, and C. Yang, “Optical phase conjugation for turbidity suppression in biological samples,” *Nature Photonics*, vol. 2, no. 2, p. 110, 2008.
- [14] J. Yoon, M. Lee, K. Lee, N. Kim, J. M. Kim, J. Park, H. Yu, C. Choi, W. Do Heo, and Y. Park, “Optogenetic control of cell signaling pathway through scattering skull using wavefront shaping,” *Scientific Reports*, vol. 5, p. 13 289, 2015.
- [15] R. Sarma, A. G. Yamilov, S. Petrenko, Y. Bromberg, and H. Cao, “Control of energy density inside a disordered medium by coupling to open or closed channels,” *Physical Review Letters*, vol. 117, no. 8, p. 086 803, 2016.
- [16] S. Popoff, G. Lerosey, R. Carminati, M. Fink, A. Boccara, and S. Gigan, “Measuring the transmission matrix in optics: An approach to the study and control of light propagation in disordered media,” *Physical Review Letters*, vol. 104, no. 10, p. 100 601, 2010.
- [17] Y. Choi, T. D. Yang, C. Fang-Yen, P. Kang, K. J. Lee, R. R. Dasari, M. S. Feld, and W. Choi, “Overcoming the diffraction limit using multiple light scattering in a highly disordered medium,” *Physical Review Letters*, vol. 107, no. 2, p. 023 902, 2011.

- [18] H. Yu, T. R. Hillman, W. Choi, J. O. Lee, M. S. Feld, R. R. Dasari, and Y. Park, “Measuring large optical transmission matrices of disordered media,” *Physical Review Letters*, vol. 111, no. 15, p. 153 902, 2013.
- [19] D. B. Conkey, A. M. Caravaca-Aguirre, and R. Piestun, “High-speed scattering medium characterization with application to focusing light through turbid media,” *Optics Express*, vol. 20, no. 2, pp. 1733–1740, 2012.
- [20] E. N. Leith and J. Upatnieks, “Holographic imagery through diffusing media,” *JOSA*, vol. 56, no. 4, pp. 523–523, 1966.
- [21] M. Cui and C. Yang, “Implementation of a digital optical phase conjugation system and its application to study the robustness of turbidity suppression by phase conjugation,” *Optics Express*, vol. 18, no. 4, pp. 3444–3455, 2010.
- [22] C.-L. Hsieh, Y. Pu, R. Grange, and D. Psaltis, “Digital phase conjugation of second harmonic radiation emitted by nanoparticles in turbid media,” *Optics Express*, vol. 18, no. 12, pp. 12 283–12 290, 2010.
- [23] T. R. Hillman, T. Yamauchi, W. Choi, R. R. Dasari, M. S. Feld, Y. Park, and Z. Yaqoob, “Digital optical phase conjugation for delivering two-dimensional images through turbid media,” *Scientific Reports*, vol. 3, p. 1909, 2013.
- [24] Y. Shen, Y. Liu, C. Ma, and L. V. Wang, “Focusing light through biological tissue and tissue-mimicking phantoms up to 9.6 cm in thickness with digital optical phase conjugation,” *Journal of Biomedical Optics*, vol. 21, no. 8, p. 085 001, 2016.
- [25] D. Wang, E. H. Zhou, J. Brake, H. Ruan, M. Jang, and C. Yang, “Focusing through dynamic tissue with millisecond digital optical phase conjugation,” *Optica*, vol. 2, no. 8, pp. 728–735, 2015.
- [26] Y. Liu, P. Lai, C. Ma, X. Xu, A. A. Grabar, and L. V. Wang, “Optical focusing deep inside dynamic scattering media with near-infrared time-reversed ultrasonically encoded (TRUE) light,” *Nature Communications*, vol. 6, 2015.
- [27] Y. Liu, C. Ma, Y. Shen, J. Shi, and L. V. Wang, “Focusing light inside dynamic scattering media with millisecond digital optical phase conjugation,” *Optica*, vol. 4, no. 2, pp. 280–288, 2017.
- [28] C. Ma, F. Zhou, Y. Liu, and L. V. Wang, “Single-exposure optical focusing inside scattering media using binarized time-reversed adapted perturbation,” *Optica*, vol. 2, no. 10, pp. 869–876, 2015.
- [29] Y. Liu, C. Ma, Y. Shen, and L. V. Wang, “Bit-efficient, sub-millisecond wavefront measurement using a lock-in camera for time-reversal based optical focusing inside scattering media,” *Optics Letters*, vol. 41, no. 7, pp. 1321–1324, 2016.

- [30] M. Jang, H. Ruan, I. M. Vellekoop, B. Judkewitz, E. Chung, and C. Yang, "Relation between speckle decorrelation and optical phase conjugation (OPC)-based turbidity suppression through dynamic scattering media: A study on in vivo mouse skin," *Biomedical Optics Express*, vol. 6, no. 1, pp. 72–85, 2015.
- [31] I. M. Vellekoop, M. Cui, and C. Yang, "Digital optical phase conjugation of fluorescence in turbid tissue," *Applied Physics Letters*, vol. 101, no. 8, p. 081 108, 2012.
- [32] I. M. Vellekoop, E. Van Putten, A. Lagendijk, and A. Mosk, "Demixing light paths inside disordered metamaterials," *Optics Express*, vol. 16, no. 1, pp. 67–80, 2008.
- [33] N. Ji, D. E. Milkie, and E. Betzig, "Adaptive optics via pupil segmentation for high-resolution imaging in biological tissues," *Nature Methods*, vol. 7, no. 2, p. 141, 2009.
- [34] J. Tang, R. N. Germain, and M. Cui, "Superpenetration optical microscopy by iterative multiphoton adaptive compensation technique," *Proceedings of the National Academy of Sciences*, vol. 109, no. 22, pp. 8434–8439, 2012.
- [35] O. Katz, E. Small, Y. Guan, and Y. Silberberg, "Noninvasive nonlinear focusing and imaging through strongly scattering turbid layers," *Optica*, vol. 1, no. 3, pp. 170–174, 2014.
- [36] I. N. Papadopoulos, J.-S. Jouhanneau, J. F. Poulet, and B. Judkewitz, "Scattering compensation by focus scanning holographic aberration probing (f-sharp)," *Nature Photonics*, vol. 11, no. 2, p. 116, 2017.
- [37] E. H. Zhou, H. Ruan, C. Yang, and B. Judkewitz, "Focusing on moving targets through scattering samples," *Optica*, vol. 1, no. 4, pp. 227–232, 2014.
- [38] C. Ma, X. Xu, Y. Liu, and L. V. Wang, "Time-reversed adapted-perturbation (TRAP) optical focusing onto dynamic objects inside scattering media," *Nature Photonics*, vol. 8, no. 12, p. 931, 2014.
- [39] F. Kong, R. H. Silverman, L. Liu, P. V. Chitnis, K. K. Lee, and Y.-C. Chen, "Photoacoustic-guided convergence of light through optically diffusive media," *Optics Letters*, vol. 36, no. 11, pp. 2053–2055, 2011.
- [40] A. M. Caravaca-Aguirre, D. B. Conkey, J. D. Dove, H. Ju, T. W. Murray, and R. Piestun, "High contrast three-dimensional photoacoustic imaging through scattering media by localized optical fluence enhancement," *Optics Express*, vol. 21, no. 22, pp. 26 671–26 676, 2013.
- [41] T. Chaigne, O. Katz, A. C. Boccara, M. Fink, E. Bossy, and S. Gigan, "Controlling light in scattering media non-invasively using the photoacoustic transmission matrix," *Nature Photonics*, vol. 8, no. 1, p. 58, 2014.
- [42] P. Lai, L. Wang, J. W. Tay, and L. V. Wang, "Photoacoustically guided wavefront shaping for enhanced optical focusing in scattering media," *Nature Photonics*, vol. 9, no. 2, p. 126, 2015.

- [43] J. W. Tay, P. Lai, Y. Suzuki, and L. V. Wang, “Ultrasonically encoded wavefront shaping for focusing into random media,” *Scientific Reports*, vol. 4, p. 3918, 2014.
- [44] X. Xu, H. Liu, and L. V. Wang, “Time-reversed ultrasonically encoded optical focusing into scattering media,” *Nature Photonics*, vol. 5, no. 3, pp. 154–157, 2011.
- [45] Y. M. Wang, B. Judkewitz, C. A. DiMarzio, and C. Yang, “Deep-tissue focal fluorescence imaging with digitally time-reversed ultrasound-encoded light,” *Nature Communications*, vol. 3, p. 928, 2012.
- [46] K. Si, R. Fiolka, and M. Cui, “Fluorescence imaging beyond the ballistic regime by ultrasound-pulse-guided digital phase conjugation,” *Nature Photonics*, vol. 6, no. 10, p. 657, 2012.
- [47] H. Ruan, T. Haber, Y. Liu, J. Brake, J. Kim, J. M. Berlin, and C. Yang, “Focusing light inside scattering media with magnetic-particle-guided wavefront shaping,” *Optica*, vol. 4, no. 11, pp. 1337–1343, 2017.
- [48] H. Ruan, M. Jang, and C. Yang, “Optical focusing inside scattering media with time-reversed ultrasound microbubble encoded light,” *Nature communications*, vol. 6, p. 8968, 2015.
- [49] B. F. Fosque, Y. Sun, H. Dana, C.-T. Yang, T. Ohyama, M. R. Tadross, R. Patel, M. Zlatic, D. S. Kim, M. B. Ahrens, *et al.*, “Labeling of active neural circuits in vivo with designed calcium integrators,” *Science*, vol. 347, no. 6223, pp. 755–760, 2015.
- [50] H. H. Yang and F. St-Pierre, “Genetically encoded voltage indicators: Opportunities and challenges,” *Journal of Neuroscience*, vol. 36, no. 39, pp. 9977–9989, 2016.
- [51] E. S. Boyden, F. Zhang, E. Bamberg, G. Nagel, and K. Deisseroth, “Millisecond-timescale, genetically targeted optical control of neural activity,” *Nature neuroscience*, vol. 8, no. 9, pp. 1263–1268, 2005.
- [52] D. G. Ouzounov, T. Wang, M. Wang, D. D. Feng, N. G. Horton, J. C. Cruz-Hernández, Y.-T. Cheng, J. Reimer, A. S. Tolias, N. Nishimura, *et al.*, “In vivo three-photon imaging of activity of gcamp6-labeled neurons deep in intact mouse brain,” *Nature Methods*, vol. 14, no. 4, pp. 388–390, 2017.
- [53] J. P. Rickgauer and D. W. Tank, “Two-photon excitation of channelrhodopsin-2 at saturation,” *Proceedings of the National Academy of Sciences*, vol. 106, no. 35, pp. 15 025–15 030, 2009.
- [54] B. K. Andrasfalvy, B. V. Zemelman, J. Tang, and A. Vaziri, “Two-photon single-cell optogenetic control of neuronal activity by sculpted light,” *Proceedings of the National Academy of Sciences*, vol. 107, no. 26, pp. 11 981–11 986, 2010.

- [55] E. Papagiakoumou, F. Anselmi, A. Bègue, V. De Sars, J. Glückstad, E. Y. Isacoff, and V. Emiliani, “Scanless two-photon excitation of channelrhodopsin-2,” *Nature Methods*, vol. 7, no. 10, pp. 848–854, 2010.
- [56] R. Prakash, O. Yizhar, B. Grewe, C. Ramakrishnan, N. Wang, I. Goshen, A. M. Packer, D. S. Peterka, R. Yuste, M. J. Schnitzer, *et al.*, “Two-photon optogenetic toolbox for fast inhibition, excitation and bistable modulation,” *Nature Methods*, vol. 9, no. 12, pp. 1171–1179, 2012.
- [57] A. M. Packer, D. S. Peterka, J. J. Hirtz, R. Prakash, K. Deisseroth, and R. Yuste, “Two-photon optogenetics of dendritic spines and neural circuits,” *Nature Methods*, vol. 9, no. 12, pp. 1202–1205, 2012.
- [58] F. Zhang, V. Gradinaru, A. R. Adamantidis, R. Durand, R. D. Airan, L. De Lecea, and K. Deisseroth, “Optogenetic interrogation of neural circuits: Technology for probing mammalian brain structures,” *Nature protocols*, vol. 5, no. 3, pp. 439–456, 2010.
- [59] I. Yamaguchi and T. Zhang, “Phase-shifting digital holography,” *Optics Letters*, vol. 22, no. 16, pp. 1268–1270, 1997.
- [60] H. Ruan, M. Jang, B. Judkewitz, and C. Yang, “Iterative time-reversed ultrasonically encoded light focusing in backscattering mode,” *Scientific Reports*, vol. 4, p. 7156, 2014.
- [61] K. Si, R. Fiolka, and M. Cui, “Breaking the spatial resolution barrier via iterative sound-light interaction in deep tissue microscopy,” *Scientific Reports*, vol. 2, p. 748, 2012.
- [62] Y. Suzuki, J. W. Tay, Q. Yang, and L. V. Wang, “Continuous scanning of a time-reversed ultrasonically encoded optical focus by reflection-mode digital phase conjugation,” *Optics Letters*, vol. 39, no. 12, pp. 3441–3444, 2014.
- [63] C. Xiao, J. R. Cho, C. Zhou, J. B. Treweek, K. Chan, S. L. McKinney, B. Yang, and V. Gradinaru, “Cholinergic mesopontine signals govern locomotion and reward through dissociable midbrain pathways,” *Neuron*, vol. 90, no. 2, pp. 333–347, 2016.
- [64] J. R. Cho, J. B. Treweek, J. E. Robinson, C. Xiao, L. R. Bremner, A. Greenbaum, and V. Gradinaru, “Dorsal raphe dopamine neurons modulate arousal and promote wakefulness by salient stimuli,” *Neuron*, vol. 94, no. 6, pp. 1205–1219, 2017.
- [65] C. K. Kim, S. J. Yang, N. Pichamoorthy, N. P. Young, I. Kauvar, J. H. Jennings, T. N. Lerner, A. Berndt, S. Y. Lee, C. Ramakrishnan, *et al.*, “Simultaneous fast measurement of circuit dynamics at multiple sites across the mammalian brain,” *Nature Methods*, vol. 13, no. 4, p. 325, 2016.
- [66] J. Y. Lin, P. M. Knutsen, A. Muller, D. Kleinfeld, and R. Y. Tsien, “ReaChR: A red-shifted variant of channelrhodopsin enables deep transcranial optogenetic excitation,” *Nature neuroscience*, vol. 16, no. 10, pp. 1499–1508, 2013.

- [67] M. Z. Lin and M. J. Schnitzer, “Genetically encoded indicators of neuronal activity,” *Nature neuroscience*, vol. 19, no. 9, pp. 1142–1153, 2016.
- [68] M. Jang, C. Yang, and I. Vellekoop, “Optical phase conjugation with less than a photon per degree of freedom,” *Physical Review Letters*, vol. 118, no. 9, p. 093 902, 2017.
- [69] M. Jang, H. Ruan, B. Judkewitz, and C. Yang, “Model for estimating the penetration depth limit of the time-reversed ultrasonically encoded optical focusing technique,” *Optics Express*, vol. 22, no. 5, pp. 5787–5807, 2014.
- [70] A. S. Chuong, M. L. Miri, V. Busskamp, G. A. Matthews, L. C. Acker, A. T. Sørensen, A. Young, N. C. Klapoetke, M. A. Henninger, S. B. Kodandaramaiah, *et al.*, “Noninvasive optical inhibition with a red-shifted microbial rhodopsin,” *Nature neuroscience*, vol. 17, no. 8, pp. 1123–1129, 2014.
- [71] A. A. Kaberniuk, A. A. Shemetov, and V. V. Verkhusha, “A bacterial phytochrome-based optogenetic system controllable with near-infrared light,” *Nature Methods*, vol. 13, no. 7, pp. 591–597, 2016.
- [72] J. Brake, M. Jang, and C. Yang, “Analyzing the relationship between decorrelation time and tissue thickness in acute rat brain slices using multispeckle diffusing wave spectroscopy,” *JOSA A*, vol. 33, no. 2, pp. 270–275, 2016.
- [73] A. Lev and B. Sfez, “In vivo demonstration of the ultrasound-modulated light technique,” *JOSA A*, vol. 20, no. 12, pp. 2347–2354, 2003.
- [74] M. M. Qureshi, J. Brake, H.-J. Jeon, H. Ruan, Y. Liu, A. M. Safi, T. J. Eom, C. Yang, and E. Chung, “In vivo study of optical speckle decorrelation time across depths in the mouse brain,” *Biomedical optics express*, vol. 8, no. 11, pp. 4855–4864, 2017.
- [75] T. Laforest, A. Verdant, A. Dupret, S. Gigan, F. Ramaz, and G. Tessier, “Co-integration of a smart cmos image sensor and a spatial light modulator for real-time optical phase modulation,” in *Image Sensors and Imaging Systems 2014*, International Society for Optics and Photonics, vol. 9022, 2014, 90220N.
- [76] M. Jang, H. Ruan, H. Zhou, B. Judkewitz, and C. Yang, “Method for auto-alignment of digital optical phase conjugation systems based on digital propagation,” *Optics Express*, vol. 22, no. 12, pp. 14 054–14 071, 2014.

INTERFEROMETRIC SPECKLE VISIBILITY SPECTROSCOPY

This chapter contains unpublished content from a manuscript in preparation.

5.1 Abstract

The dynamics of blood flow within tissue are a key indicator of metabolic function, providing functional information about physiological activity. Speckle visibility spectroscopy (SVS) is an emerging technique that allows for blood flow dynamics to be measured non-invasively using the dynamic properties of a captured optical field that has interacted with blood in a volume of interest. SVS works by analyzing the statistical properties of blurred speckle fields. This blurring is caused by the dynamic scattering of the blood cells and the statistics of the blurred speckle pattern contain information about the blood flow dynamics. In this chapter, we present a new technique called interferometric speckle visibility spectroscopy (iSVS), which enables high-speed and sensitive measurement of the optical field dynamics with shot-noise limited sensitivity. This enables sensitive, non-invasive monitoring of hemodynamic activity, with light power levels that are safe for clinical applications.

5.2 Introduction

When coherent light illuminates a dynamic scattering sample like living tissue, the interference of the different scattered light components generates an optical interference pattern called a speckle field. When the scatterers within the tissue move, this generates temporal fluctuations in the speckle pattern.

These changes in the speckle pattern are related to the movement of the scatterers within the sample. One way to quantify the dynamics of the speckle field and relate them to the scatterer movement is provided by the framework of diffusing wave spectroscopy (DWS). DWS was originally developed in the late 1980s to investigate materials like gels and colloidal suspensions. The basic theory is explained in reference [1]. In essence, a very sensitive single-pixel photodetector, such as an avalanche photodiode (APD), is used to collect light from a single speckle grain of the speckle pattern and monitor its fluctuations over time. Then, by computing the temporal autocorrelation function of the intensity time trace, $g_2(t)$, the decay can be fit to a theoretical model to extract quantities of interest such as the diffusion

coefficient of the sample under test.

In the mid-1990s, the Yodh group at the University of Pennsylvania realized that DWS theory could be applied to biological tissue to measure dynamics of interest to the medical community such as blood flow speed [2]. The application of DWS techniques to biological tissue is called diffuse correlation spectroscopy (DCS) and shares its fundamental physics with DWS. However, one of the limitations of DWS is that it can only sample a single speckle grain to maximize the contrast and SNR of the measurement, fundamentally limiting the throughput of the measurement. This limited throughput means that to sample many realizations of the scattering process and obtain an accurate $g_2(t)$ curve, the measurement time (T) must contain many decorrelation events (typically on the order of $T = 1000 \cdot t_d$ where t_d is the decorrelation time). For example, this means that to accurately measure a decorrelation time of 1 ms requires a total measurement time of 1 s.

This requirement on the measurement time fundamentally limits the refresh time of the system, requiring that the statistics of the dynamic scattering process must remain fixed within the measurement time T . While this may hold true in the case of beads diffusing in suspension, it is often not true in biological situations since the decorrelation from blood flow can change value several times during one second (e.g., due to pulsation from the heartbeat, which can be on the order of several Hertz for rodents).

One straightforward solution to this problem is to trade off measurements in time for measurements in space, sampling multiple speckles in parallel. This is the strategy used in multispeckle diffusing wave spectroscopy, the technique used in chapters 2 and 3. However, this method still requires several measurements within a single decorrelation time, which becomes infeasible with current camera technology when the decorrelation time is very short (1 ms).

One way to measure the decorrelation time in a single frame is to use the statistics of blurred speckle patterns that are captured in a single exposure longer than the decorrelation time. This is the basic idea behind speckle visibility spectroscopy (SVS) [3]. SVS uses a camera to record the intensity of dynamic speckle fields which are then used to characterize the speckle field decorrelation time τ . If the camera exposure time T is longer than the speckle field decorrelation time τ , there will be multiple independent speckle fields recorded by the camera within the exposure time. Since these independent speckle fields arrive at the camera at different times, the pattern recorded over the entire exposure is the intensity summation of these

independent speckle patterns. If the speckle pattern does not decorrelate, then the intensity summation over the exposure simply records a scaled version of a stable speckle pattern. However, if the speckle changes during the exposure time, the independent speckle patterns will add incoherently and ultimately modify the statistics of the recorded speckle pattern.

One such statistic of interest is the speckle contrast (κ), defined as

$$\kappa = \frac{\sigma}{\mu}, \quad (5.1)$$

where σ is the standard deviation of the measured speckle pattern and μ is the mean intensity of the recorded speckle pattern.

The speckle contrast decreases as multiple independent speckle intensity patterns add up on the camera, and mathematical models have been developed which relate the measured speckle pattern contrast to the camera exposure time T and the speckle field decorrelation time τ [4]. Exploiting this relationship, the speckle field decorrelation time can be calculated by measuring the speckle pattern contrast and inferring information about the biological activities that influenced the dynamic properties of the tissue.

However, there are two conditions that must be satisfied when using SVS: (1) The Siegert relation should hold, and (2) the photon number should be large enough to overwhelm the camera noise. For condition 1, the Siegert relation assumes a fully-developed speckle pattern and then takes advantage of its statistical properties to convert the intensity autocorrelation function $g_2(t)$ to the complex field autocorrelation function $g_1(t)$. If the speckles are not fully developed, which can happen if the photons do not experience multiple scattering events in the scattering medium, the output speckle pattern no longer follows fully-developed speckle statistics [5]. In this case, the Siegert relation does not hold and there is not a direct connection between $g_2(t)$ and $g_1(t)$. Moreover, there is an empirical factor β when converting $g_2(t)$ to $g_1(t)$, which also introduces systematic inaccuracy to the measurement. For condition 2, if the speckle field decorrelation time changes quickly, the camera should have a short exposure time and high frame rate to monitor the change of the decorrelation time that limits the number of available signal photons. In this case, the dark current and readout noise of the camera can swamp the signal. Here, we propose and demonstrate a new method termed interferometric speckle visibility

spectroscopy (iSVS), which circumvents the two aforementioned conditions and is able to exploit $g_1(t)$ directly even when the number of available signal photons is limited.

5.3 Theory

The iSVS architecture is based on an off-axis Mach-Zender interferometer and uses a planar, tilted reference beam to record off-axis holograms, enabling single-shot complex sample field reconstruction. This removes the constraint of the Siegert relation (condition 1), since we can retrieve the complex sample field from the off-axis holograms and calculate $g_1(t)$ directly. The introduction of the reference beam also enables the low signal field to be boosted above the camera noise threshold using the heterodyne gain of the reference beam. Therefore, the constraints of condition 2 also become less restrictive.

In the iSVS setup, the tilted planar reference beam $E_r(\mathbf{r}, t) = E_0 \exp(i\mathbf{k} \cdot \mathbf{r})$ and the signal beam $E_s(\mathbf{r}, t) = E_s \exp(i\phi_s(\mathbf{r}, t))$ interfere on the camera sensor, where $\mathbf{r} = (x, y)$ is the spatial coordinate, t is the time, E_0 is the amplitude of the reference beam, \mathbf{k} is the wave vector corresponding to the tilted plane wave, and $E_s(\mathbf{r}, t)$ and $\phi_s(\mathbf{r}, t)$ are the amplitude and phase of the signal field, respectively. The camera records the intensity pattern due to the interference of the sample and reference beams given by

$$\begin{aligned} I(\mathbf{r}) &= \int_0^T |E_r(\mathbf{r}) + E_s(\mathbf{r})|^2 dt \\ &= \int_0^T |E_r(\mathbf{r})|^2 + |E_s(\mathbf{r})|^2 + 2E_0(\mathbf{r})E_s(\mathbf{r}, t) \cos(\mathbf{k} \cdot \mathbf{r} - \phi_s(\mathbf{r}, t)) dt, \end{aligned} \quad (5.2)$$

where $t = 0$ defines the beginning of the exposure and T is the exposure time.

Since the reference beam is tilted with respect to the sample beam, it generates an interference fringe pattern and separates the third term in Equation 5.2 in the spatial frequency domain. Therefore, by taking the Fourier transform of the captured off-axis hologram, and using the known planar reference beam field profile, the complex sample field can be recovered by spatially filtering the image in the spatial frequency domain. After extracting the complex sample field $E_s(\mathbf{r}, t)$ from the off-axis hologram, we can further analyze the statistics of this sample field to retrieve the dynamics of the scattering sample.

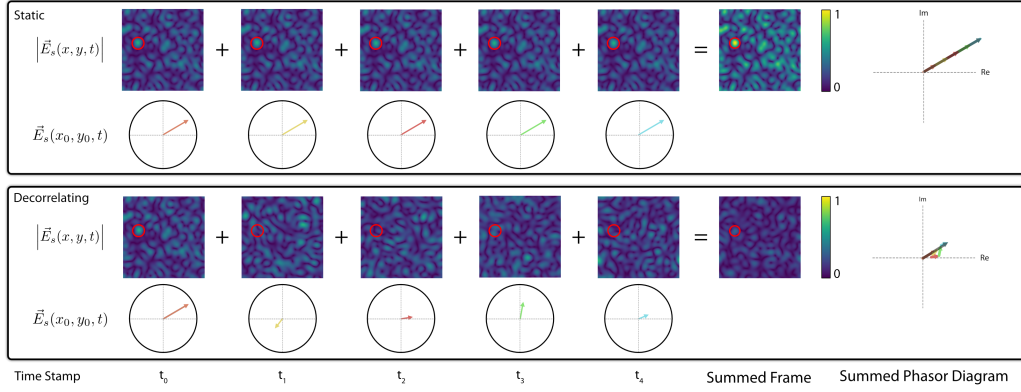


Figure 5.1: iSVS decorrelation explanation. This figure demonstrates the difference between the static and decorrelating samples in the iSVS measurement. If the medium is static (top row), then the field is the same at each time point. However, if the medium is decorrelating (bottom row), then the speckle pattern at each time stamp is independent.

The principle of iSVS can be intuitively understood by the diagrams shown in Figure 5.1. First, we should consider the influence of decorrelation on the sample speckle field. As shown in the top row of Figure 5.1, if the sample field is static, then the amplitude and phase of a specific coherence area (i.e., a speckle grain) is fixed as a function of time. Therefore, the integration of the sample field over the exposure time will simply create a scaled version of the static speckle pattern.

On the other hand, if the speckle pattern is decorrelating due to motion within the sample (bottom row of Figure 5.1), then the sample field and the complex amplitude and phase of the speckle field will fluctuate as a function of time. The effect of this fluctuation will be to create a new speckle pattern that will have a lower average magnitude than the static case, since the integrated sample electric field will effectively result in the summation of a random walk in the complex plane at each speckle grain where the amplitude and phase of the phasor is drawn from the corresponding statistical distributions known for speckle (e.g., Rayleigh distributed amplitude and uniformly distributed phase).

Defining the heterodyne signal as

$$S(r) = \frac{1}{T} \int_0^T 2E_0 E_s(\mathbf{r}, t) \cos(\mathbf{k} \cdot \mathbf{r} - \phi_s(\mathbf{r}, t)) dt, \quad (5.3)$$

and following the derivation of reference [3], the second moment of $S(\mathbf{r})$ contains $g_1(t)$:

$$\begin{aligned}
\langle S(\mathbf{r})^2 \rangle &= \frac{4E_0^2}{T^2} \left\langle \int_0^T \int_0^T E_s(\mathbf{r}, t_1) \cos(\mathbf{k} \cdot \mathbf{r} - \phi_s(\mathbf{r}, t_1)) \right. \\
&\quad \left. E_s(\mathbf{r}, t_1) \cos(\mathbf{k} \cdot \mathbf{r} - \phi_s(\mathbf{r}, t_1)) dt_1 dt_1 \right\rangle \\
&= \frac{4E_0^2 \overline{E_s^2}}{T} \int_0^T 2 \left(1 - \frac{t}{T}\right) (g_1(t))^2 dt \\
&= \frac{4I_0 \overline{I_s}}{T} \int_0^T 2 \left(1 - \frac{t}{T}\right) (g_1(t))^2 dt. \tag{5.4}
\end{aligned}$$

As we can see from Eq. 5.4, the second moment of $S(\mathbf{r})$ is a function of the integrated value of $g_1(t)$ over the exposure time, weighted by a factor inversely proportional to the exposure time T . In the case where our sample field is a speckle pattern, we can intuitively understand the behavior of the second moment as measuring the blurring of the speckle pattern. If the sample is slowly decorrelating over the exposure time (i.e., $g_1(t) \approx 1$ for $0 < t < T$), then the result of the integral is

$$\begin{aligned}
\langle S(\mathbf{r})^2 \rangle &= \frac{4I_0 \overline{I_s}}{T} \int_0^T 2 \left(1 - \frac{t}{T}\right) (g_1(t))^2 dt \\
&= \frac{4I_0 \overline{I_s}}{T} \cdot T \\
&= 4I_0 \overline{I_s}. \tag{5.5}
\end{aligned}$$

As the decorrelation time increases and the value of $g_1(t)$ begins to significantly decay from 1 during the exposure time T , the value of $\langle S(\mathbf{r})^2 \rangle$ will decrease. In the limit where the value of $g_1(t)$ decays quickly to 0 relative to the exposure time, the value of $\langle S(\mathbf{r})^2 \rangle$ decays to zero. Therefore, by measuring the second moment of the sample field, the decorrelation time can be inferred.

5.4 iSVS and SVS Data Processing Procedure

iSVS data processing pipeline

The data processing pipeline for iSVS and SVS data is outlined in Fig. 5.2. For the iSVS data, each captured interferogram is Fourier transformed using a 2D fast Fourier transform after subtracting an image of the reference beam alone. This

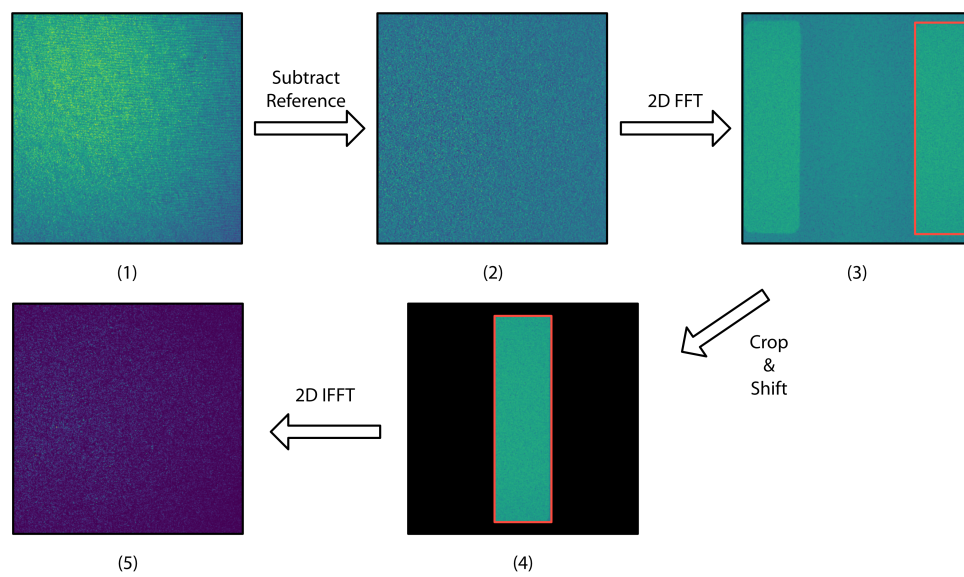


Figure 5.2: **iSVS data processing procedure.** The data processing pipeline for iSVS analysis is shown above. First, a reference frame is subtracted to suppress noise from non-uniformities in the reference beam. Then, the reference-subtracted image is Fourier transformed revealing off-axis lobes containing the sample field information. One of these lobes is selected, cropped, and shifted to the center of the spatial frequency space to remove the phase ramp of the reference beam in the spatial domain. Then, this cropped and shifted spectrum is inverse Fourier transformed to recover the sample speckle field. The magnitude of this speckle field is directly related to the decorrelation time of the light contributing to it.

acts to suppress noise from non-uniformities in the reference beam that can lead to additional noise within the range of spatial frequencies that contains the signal. Next, one of the off-axis lobes is selected, cropped, and shifted to the center of the spatial frequency domain and divided by the amplitude of the reference beam to yield the sample amplitude only. Then, this cropped and shifted signal is transformed back to the spatial domain using an inverse Fourier transform, yielding an image of the complex amplitude and phase of the sample speckle field. Here we also note that the final inverse Fourier transform is not strictly necessary unless one wishes to perform analysis on different spatial locations. In practice, this is valuable since different spatial locations can represent contributions from different areas and path length distributions and can be used to extract more information from the sample.

After the sample field is reconstructed using the steps outlined above, the decorrelation of a given area is calculated by taking the average of the sample electric field

magnitude within that area. As described in the iSVS theory, this magnitude maps to decorrelation time with smaller and larger sample field amplitudes signifying shorter and longer decorrelation times respectively.

SVS data processing pipeline

The processing pipeline for SVS is much simpler, since it does not involve interference from a reference beam. For each frame, the speckle contrast, κ , of the frame can be computed using the equation

$$\kappa = \frac{\sigma}{\mu} \quad (5.6)$$

where σ is the standard deviation of the frame and μ is the mean of the frame. For a fully developed speckle field, the statistics of speckle indicate that this value should be unity. However, when several independent speckle fields are summed together incoherently (as occurs when a decorrelating speckle pattern is integrated over the exposure time of a camera frame), the speckle contrast decreases since the standard deviation drops. Therefore, the speckle contrast can be considered a proxy for the decorrelation time.

In the same way as with iSVS, the SVS signal can be spatially cropped and separate areas analyzed to tease out location dependent signals. In this case, the speckle contrast is computed within each smaller region of interest.

5.5 Experimental Results

The experimental setup for iSVS is based on an off-axis holography configuration as shown in Figure 5.3. A long coherence length laser is split into a sample and reference arm. The sample arm is coupled into a single-mode fiber and directed to the sample of interest, either in a transmission or reflection geometry. Then, the sample beam is collected by a lens and imaged onto the camera after being spatially filtered by an aperture in the Fourier plane of the 4-f system. This aperture is a vertical slit designed to maximize the spatial bandwidth of the collected signal.

If we consider the available bandwidth in the spatial frequency domain for off-axis holography, we can consider the spatial bandwidth of the 4 terms in Equation 5.2. In the spatial frequency domain, these 4 terms form the following signals: the sample autocorrelation which is a convolution of the sample with itself and therefore has a bandwidth of $2B$ where B is the signal bandwidth, the reference autocorrelation

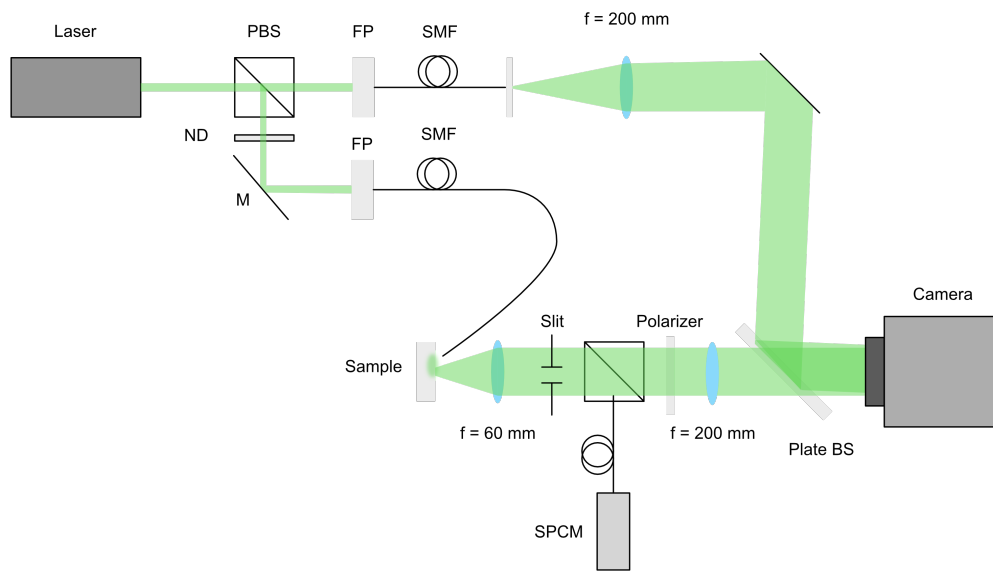


Figure 5.3: iSVS Experimental Setup. A 532 nm, diode-pumped solid-state, long coherence length, laser is used as the light source for the iSVS system. The laser light is split into two arms, sample and reference. The sample beam is coupled into a single-mode fiber and illuminates the sample. Scattered light from the sample is collected by a lens and imaged onto the camera with a 4-f imaging system. A slit in the Fourier plane of the 4-f system serves to set the sample bandwidth. A single photon counting module (SPCM) is used to capture conventional DCS measurements of the sample dynamics and for calibration. After passing through a polarizer to select only the scattered sample light that shares the same polarization as the reference beam, the scattered light is interfered with the collimated, tilted reference beam on the camera.

which is a sharply peaked delta-like function, and the two off-axis lobe terms which are the convolution of the sample with a shifted delta function from the tilted reference beam.

To maximize the bandwidth of the signal in the spatial frequency domain, we want to design the shape and size of the sample bandwidth such that we can maximally fit the off-axis lobes in the spatial frequency domain without overlapping them with the sample autocorrelation term or aliasing. Normally in off-axis systems for imaging we desire isotropic resolution and therefore would like a circular pupil in the Fourier plane. However, since in this case our sample field is a speckle field, we care primarily about sampling the maximum number of speckles and a circular pupil would leave unused space in the spatial frequency domain. To maximize the number

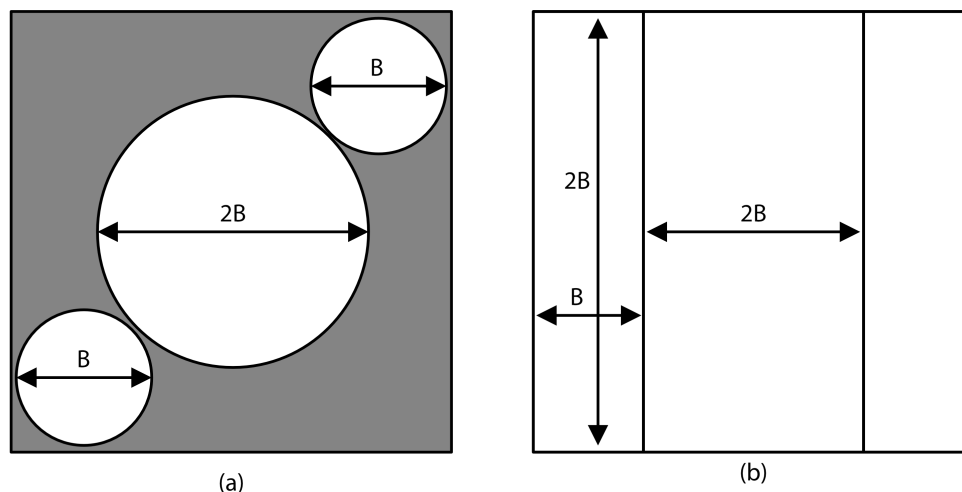


Figure 5.4: **Advantage of vertical slit in the Fourier domain for optimal spatial frequency bandwidth usage.** (a) A typical off-axis holography spatial frequency spectrum with circular sample bandwidth. This setup maintains isotropic lateral resolution, but does not efficiently use the information capacity of the system. The unused space in the spatial frequency domain is shaded gray. (b) In contrast, by using a rectangular slit to shape limit the spatial frequency content of the sample field, the spatial frequency domain can be fully used. Although the spatial resolution will now be non-isotropic, since the captured sample field is simply a speckle field, this is not a concern.

of speckle grains we collect, we need to have the speckle field cover the maximum number of pixels and have the largest spatial frequency bandwidth (smallest speckle size) allowable without aliasing. For this reason, we use a rectangular slit in the Fourier plane to set the shape of the sample spectrum and then use the tilt angle of the reference beam to position the off-axis lobes so that they fit on the sides of the spatial frequency spectrum without overlapping with the other terms.

System characterization

To verify the operation of the system, we built a decorrelating sample using a ground glass diffuser (Thorlabs, DG20 Series) mounted on an electric gearbox and motor unit (Pololu, Item #:3058) with a motor controller (Pololu, Item #:1372). Then, using a custom built Python serial interface, the motor was controlled to generate different decorrelation speeds.

A calibration procedure is used to generate a mapping between the digital signal used to drive the rotating diffuser and the decorrelation speed. A range of driving voltages

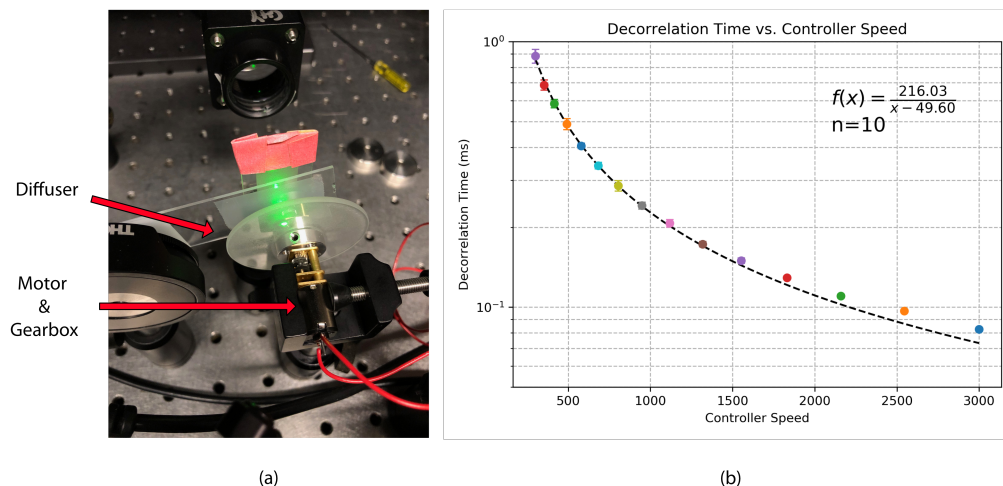


Figure 5.5: **Rotating diffuser calibration setup.** (a) A photo of the rotating diffuser setup. (b) A plot of the decorrelation time vs. motor drive speed signal from the motor controller. Ten trials were conducted for each speed. The mean and standard deviation for each speed are plotted.

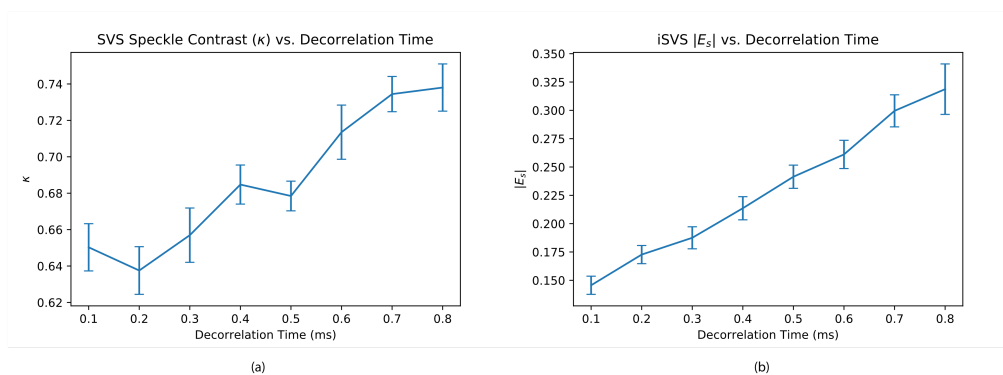


Figure 5.6: **iSVS and SVS results vs. decorrelation time with rotating diffuser.** (a) iSVS results showing the effective visibility factor vs. decorrelation time. (b) SVS results showing the speckle contrast vs. decorrelation time.

were applied to the motor and the decorrelation time computed by measuring a time trace of the fluctuations using the single photon counting module (SPCM) in the optical setup. This data is shown in Figure 5.5 and was fit with a simple inverse linear model with an offset to enable different decorrelation times to be set.

iSVS vs. SVS comparison with rotating diffuser

After developing and calibrating the rotating diffuser setup, it was used to compare the iSVS and SVS results for different decorrelation times. For the iSVS testing, the sample and reference beam were both turned on, and a series of interferograms were collected for each decorrelation time. These images were processed using the procedure detailed in Figure 5.2. Then, the reference beam was turned off and a series of frames were collected for analysis using the SVS framework. The results are shown in Figure 5.6.

Several observations can be made from these data. First, we can see that there is indeed a mapping between the sample field magnitude in iSVS as predicted by the theory. We can also see that the error bars on the iSVS curve are smaller than those on the SVS curve, indicating that the iSVS technique can more accurately measure changes in the decorrelation time.

iSVS vs. SVS in the dorsal skin flap

After calibrating the performance of the system using the controlled decorrelation time of the rotating diffuser setup, we proceeded to test the system on a rodent model. The goal of these experiments was to compare the performance of iSVS and SVS when measuring the dynamic decorrelation caused by breathing and blood flow of the animal. To do this, we illuminated the dorsal skin flap of an anesthetized rat in both transmission and reflection and processed the series of frames to analyze the dynamic behavior of the captured light. Animal husbandry and all experimental procedures involving animal subjects were approved by the Institutional Animal Care and Use Committee (IACUC) and by the Office of Laboratory Animal Resources at the California Institute of Technology under IACUC protocol 1770.

The results for the transmission geometry are shown in Figure 5.7. The fiber was positioned so that it illuminated the dorsal skin flap and the scattered light was collected and imaged on to the camera through a 4-f system as shown in Figure 5.7(a). Then, a series of datasets were captured while the sample beam power was reduced in steps. The laser powers for Figure 5.7(b1-b6) were 1, 0.5, 0.26, 0.13, 0.06, and 0.03 mW respectively.

We can see that when the laser power is strong, both iSVS and SVS can resolve the dynamics of the sample as in 5.7(b1) and (b2). However, when the signal light intensity drops so that it is buried in the camera noise, SVS can no longer detect the decorrelation changes. However, due to the heterodyne gain provided by the

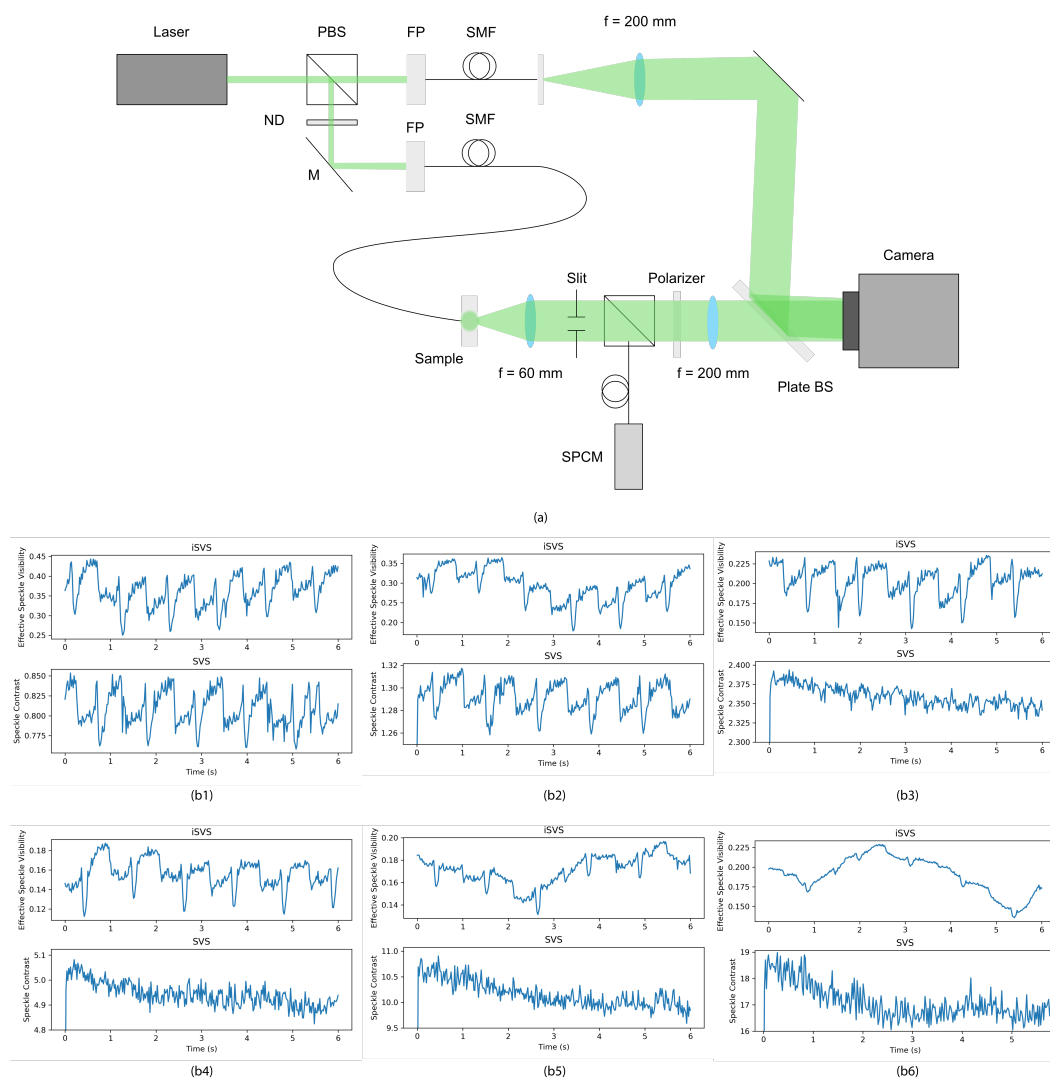


Figure 5.7: **iSVS and SVS results in the dorsal skin flap: transmission.** (a) The experimental setup for the iSVS and SVS measurements in transmission. (b) Experimental results for iSVS and SVS for different sample beam intensities. The laser powers for (b1-b6) were 1, 0.5, 0.26, 0.13, 0.06, and 0.03 mW respectively.

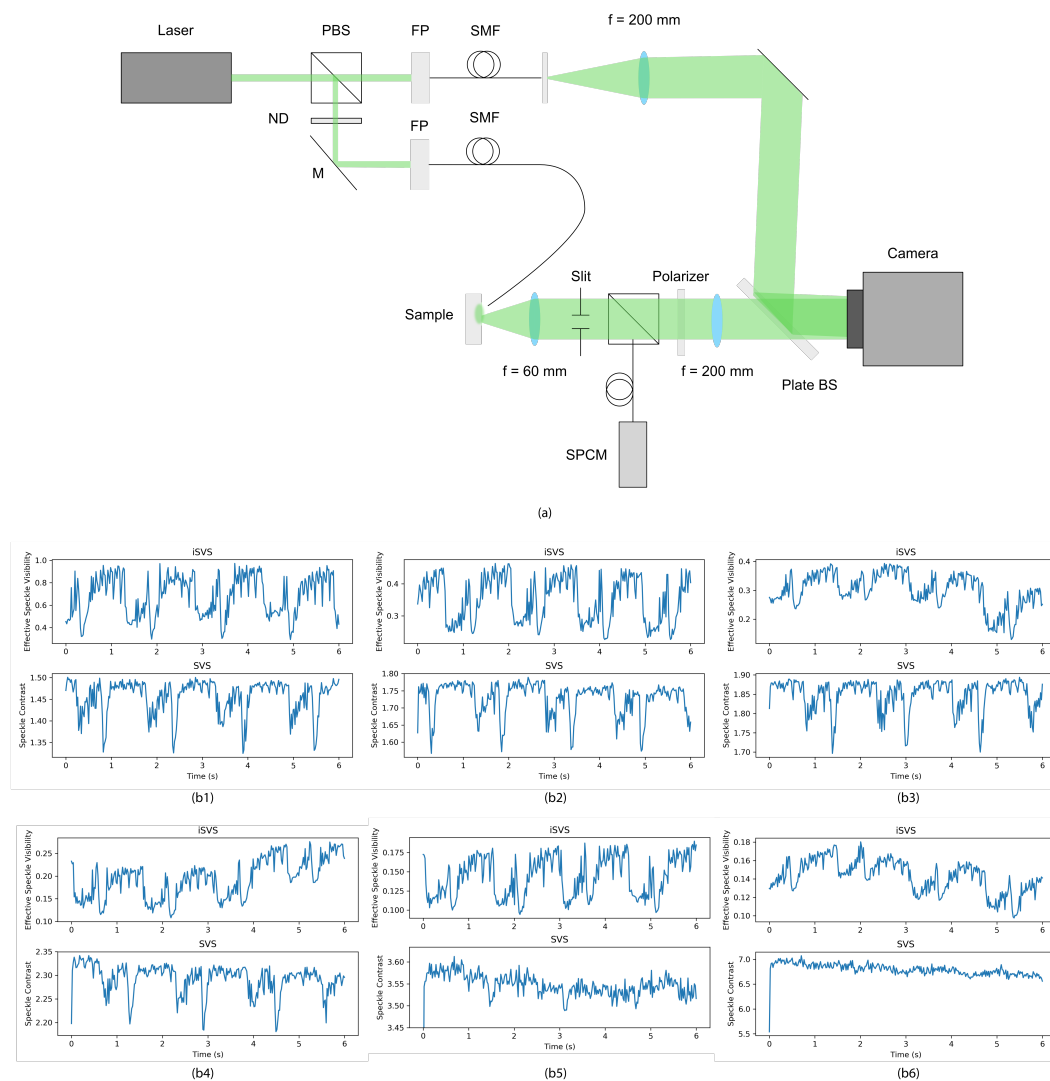


Figure 5.8: iSVS and SVS results in the dorsal skin flap: reflection. (a) The experimental setup for the iSVS and SVS measurements in reflection. (b) Experimental results for iSVS and SVS for different sample beam intensities.

reference beam in the iSVS scheme, iSVS can detect the decorrelation signal due to breathing ($\sim 2/3$ Hz) and even the blood flow from the heart beating (~ 6 Hz) down to a sample beam power of 0.06 mW in 5.7(b5). However, once the sample beam power drops to 0.03 mW in 5.7(b6), even iSVS can only faintly detect the decorrelation from breathing and can no longer resolve any heartbeat events.

For practical applications, it is often not possible to collect light in a transmission geometry. Therefore, we also re-configured the optical setup to illuminate and

collect light from the sample in a reflection geometry. The reflection setup is shown in Figure 5.8(a). Since the system was configured with an optical fiber to deliver the sample beam, this configuration simply required moving the sample beam fiber to illuminate the sample on the same side as the collection optics.

Results from the reflection geometry are shown in Figure 5.8(b1-b6). As in the transmission case, we can see that both iSVS and SVS can resolve decorrelation due to heartbeat, blood flow, and breathing events. In fact, the data collected in reflection highlight signal from the heartbeats, since these are relatively larger compared to the breathing signal as compared to the transmission geometry.

5.6 Discussion and Future Work

While the dynamic nature of biological tissue can be a challenge for wavefront shaping techniques, the decorrelation signal itself can provide valuable information about the sample. Conventional strategies to detect these changes using diffuse correlation spectroscopy (DCS) calculate the decorrelation time from a time-trace, using the assumed ergodicity of the speckle field to equate the temporal and ensemble averages. Speckle visibility based approaches replace this by using the statistics of a single captured speckle frame to calculate the decorrelation, but still require a strong scattered light signal in order to overwhelm detector noise and obtain optimal performance. By adding a reference beam, iSVS overcomes these challenges, beating detector noise to enable shot-noise-limited performance and enabling operation at the optimal exposure time for speckle visibility methods.

iSVS also provides the potential to use additional optical mechanisms to further improve system performance and resolution. For example, using a laser source with a limited coherence length can be used to select certain classes of photons, for example those that preferentially interact with deeper parts of the tissue. This path length gating can help to eliminate signal from superficial layers which may not contain the blood vessels of interest (e.g., signal from blood vessels in the scalp that can mask signal from the photons that have interacted with blood in the brain below). In future work, we plan to apply the iSVS technique to measure blood flow dynamics in the brain that can be used to non-invasively measure neural activity.

References

- [1] D. Pine, D. Weitz, J. Zhu, and E. Herbolzheimer, “Diffusing-wave spectroscopy: Dynamic light scattering in the multiple scattering limit,” *Journal de Physique*, vol. 51, no. 18, pp. 2101–2127, 1990.

- [2] D. A. Boas, L. Campbell, and A. G. Yodh, “Scattering and imaging with diffusing temporal field correlations,” *Physical Review Letters*, vol. 75, no. 9, pp. 1855–1858, 1995.
- [3] R. Bandyopadhyay, A. Gittings, S. Suh, P. Dixon, and D. J. Durian, “Speckle-visibility spectroscopy: A tool to study time-varying dynamics,” *Review of scientific instruments*, vol. 76, no. 9, p. 093 110, 2005.
- [4] D. A. Boas and A. K. Dunn, “Laser speckle contrast imaging in biomedical optics,” *Journal of Biomedical Optics*, vol. 15, no. 1, p. 011 109, 2010.
- [5] J. W. Goodman, “Some fundamental properties of speckle,” *JOSA*, vol. 66, no. 11, pp. 1145–1150, 1976.

*Chapter 6***CONCLUSION**

Scattering has historically been thought to be an insurmountable barrier for optical techniques. The goal of my PhD work and this thesis has been to join the growing community of optical scientists and engineers who are challenging this assumption and to show that there are ways to overcome the scattering nature of tissue and extend the penetration depths available to optical techniques. I hope in my future research to continue working in this field to push the envelope and develop new optical systems to harness scattered light for improved light delivery, imaging, and diagnostics.